January 2019

Optical Nanostructures For Controllable And Tunable Optical Properties

Ashfaqul Anwar Anwar Siraji
Wayne State University

OPTICAL NANOSTRUCTURES FOR CONTROLLABLE AND TUNABLE OPTICAL PROPERTIES

by

ASHFAQUL ANWAR SIRAJI

DISSERTATION

Submitted to the Graduate School

of Wayne State University,

Detroit, Michigan

in partial fulfillment of the requirements

for the degree of

DOCTOR OF PHILOSOPHY

2019

MAJOR: Electrical Engineering

Approved By:

_____

Advisor Date

_____

_____

_____

_____

ACKNOWLEDGEMENTS

I would like to express my profound gratitude to my advisor, Dr. Yang Zhao, for his generous guidance and mentorship during my time at Wayne State University. He always had time for me, offered his counsel on any problem I was facing, and aided me with infinite goodwill.

I am also thankful to Dr. Amar Basu, Dr. Mark Ming-Cheng Cheng, Dr. Pai Yen-Chen, and Dr. Golam Newaz. As members of my dissertation committee, they counseled me at every stage of the research, offered valuable perspectives and given me tips to improve my research. Without them, the dissertation would not be complete.

The ECE department and Graduate School of Wayne State University also deserve special thanks. They have provided me with consistent funding and healthcare during my studies, which allowed me to concentrate on my research without distraction. The ECE department has always been very efficient in handling my paperwork, for which I am especially thankful to Scott Lantz and Dories Ferris. Finally, the staff of the Office of International Students and Scholars has been a constant source of assistance. They have helped me in maintaining proper documentation relevant to my international status.

Finally, I am especially thankful to my family. Their support has been invaluable to me. My wife and daughter have always been my biggest source of motivation and inspiration.

TABLE OF CONTENTS

LIST OF FIGURES

LIST OF TABLES

I. INTRODUCTION

Nanostructures have always been used for their extraordinary optical properties. One of the most prominent examples of optical nanostructure in nature is the beautiful color in the wings of a butterfly. Instead of pigmentation, the color of the butterfly is produced by the nanostructure present in its wings. Another well-known example is the Lycurgus cup, which shows different colors depending on the light incidence angle. The beautiful effect is caused by a small amount of gold and silver nanoparticles mixed in the glass as a colloid.

As these examples demonstrate, the optical properties of nanostructures are as dependent on the structure as much as the constituent material. Optical nanostructures are of special interest because they can manipulate visible light in many useful ways, which cannot be obtained using bulk materials. Furthermore, the interaction between visible light and optical nanostructures can be controlled and tuned to achieve specific results. Our focus is on controllable and tunable optical nanostructures.

Our goal is to determine an efficient design and analysis method for optical nanostructures and use these methods to relate their optical properties with their physical structure. Based on these relations, we will propose and demonstrate controllable and tunable optical nanostructures. We will emphasize the transparency and low optical loss of low refractive index transparent materials and investigate their application in designing optical nanostructures. We will review commonly used methods for the design and analysis of optical nanostructures, including full-wave numerical methods and analytical effective medium approximations. We will derive a general effective medium

approximation for optical nanostructures and verify it experimentally. Finally, using our understanding of the methods of analysis, we will propose and demonstrate an efficient and fast method for designing and analyzing a controllable optical nanostructure.

A. Background

1. Optical Nanostructures

The term optical nanostructure broadly includes all nanostructures that can manipulate visible light. In this work, we define an optical nanostructure as a composite media, consisting of a linear, homogeneous and isotropic matrix material and similar inclusions with size comparable to the operating wavelength. We limit ourselves to dielectric nanostructures where plasmonic effects are absent or negligible. These dielectric optical nanostructures can be periodic photonic crystals, thin-film coatings, aperiodic planar nanostructures, or colloids. Here, a brief background of these optical nanostructures is discussed. Further discussion of different optical nanostructures can be found in the literature [1, 2].

a) Photonic crystals

Photonic crystals are composite media where the inclusions are arranged periodically in a matrix material. The periodicity can be one-dimensional or two-dimensional, with a uniform third dimension, as shown in Figure 1. Periodicity in all three dimensions is possible but rarely used in designing an optical nanostructure. Commonly used photonic crystals are planar with one- or two-dimensional periodicity.

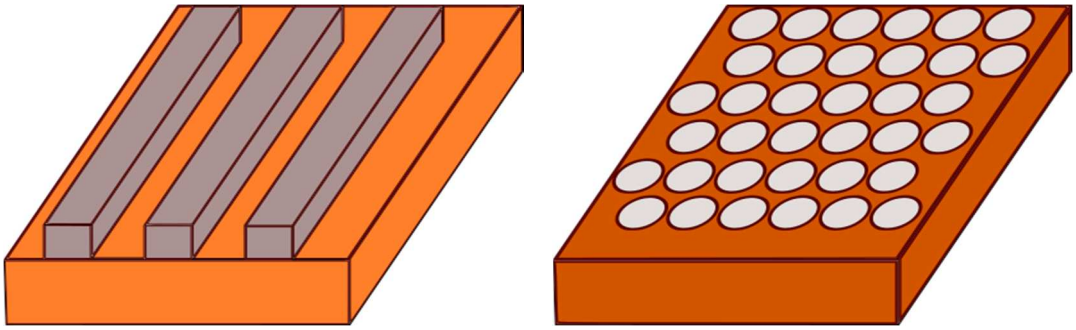

1D 2D

Figure 1 Planar photonic crystals with one-dimensional and two-dimensional periodicity.

The structure of a planar photonic crystal (PPC) can be described by its lattice, periodicity, and the refractive indices of the constituent materials. The lattice denotes the periodic arrangement of the inclusions within the matrix material. Several types of lattice for planar nanostructures have been reported in the literature, including the rectangular lattice [3], the triangular lattice [4], the honeycomb lattice, the kagome lattice [5], and other complex tiling. Triangular and rectangular lattices are utilized for most applications due to their simplicity. Aside from the lattice, the period of the planar nanostructure determines its nature. The frequency dispersion of propagating modes within a photonic crystal is controlled by its period. In such planar nanostructures, the change in group index with respect to frequency can be controlled to engineer modes with a specific frequency and dispersion property.

The most useful property of PPC is the so-called optical bandgap. It is a phenomenon where a set of frequencies is prohibited from propagating within the PPC. In effect, the photonic crystal acts as an optical insulator in the bandgap frequencies. This effect is utilized in many applications and studied in detail here in subsequent chapters. The relation between the periodicity, lattice, material property and bandgap of a PPC is not apparent because there exists no analytical solution of Maxwell's equations for a

general PPC case. Hence, numerical analysis is required to relate the bandgap to the parameters of a PPC. Typically, bandgap analysis is done by calculating the band structure of the PPC.

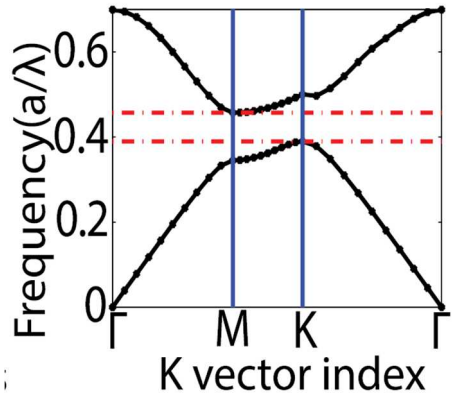

Figure 2 A sample band structure of a PPC.

In Figure 2, a sample band structure is shown. The horizontal axis shows the index of the wave vector. The band structure typically plots the frequency of different allowed modes with respect to the wave-vector of the incident wave. The index of the k vectors is chosen based on the periodicity of the lattice. The frequency is typically displayed after normalizing it by the periodicity of the lattice. In the figure, a bandgap can be found around normalized frequency 0.4. The position and width of the bandgap, as well as the shape of the individual bands, can be controlled by changing the periodicity, nature of the inclusion, or the matrix material properties.

b) Metamaterials

Metamaterials are a class of periodic optical nanostructure that are very different than PPC. Whereas PPC relies on ensemble diffraction to engineer the modes, metamaterials have no diffraction because their inclusions are deeply subwavelength. Rather, metamaterials utilize a different kind of resonant structure in a periodic lattice to

achieve unusual optical properties. In optical metamaterials, the interaction between the nanostructure and light can be codified into effective permeability (μ_{eff}) and effective permittivity (ε_{eff}). These properties are decided by the periodicity, as well as the unit-cell of the structure.

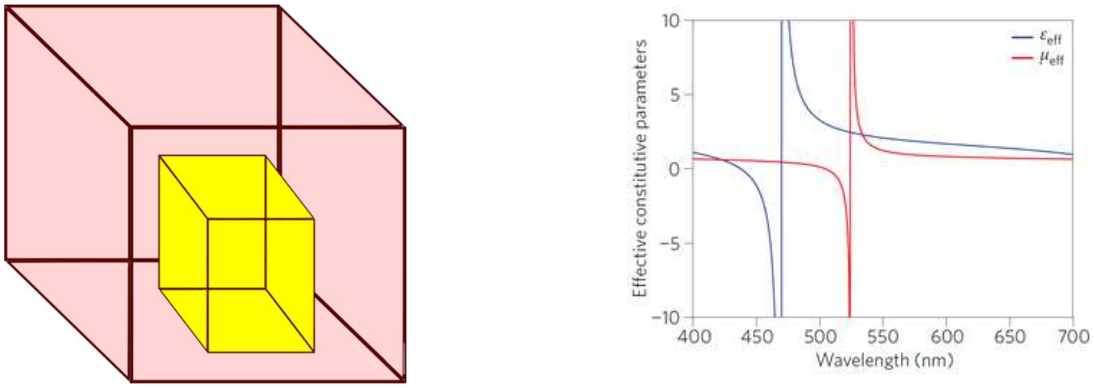

(a) Unit cell (b) Extracted effective properties

Figure 3 (a) The unit cell of a metamaterial consisting of an inclusion in a matrix thin film, (b) the extracted effective permittivity and permeability.

A sample metamaterial unit cell and its extracted parameters are shown in Figure 3. By changing the periodicity, the structure of the unit cell, or the matrix material properties, the optical properties of metamaterials can be controlled. Remarkably, the permittivity and/ or the permittivity of the metamaterial can be made negative or close-to-zero by careful design, which is very useful for many applications.

c) Colloids

Aperiodic optical nanostructure can easily extend beyond a single plane or thin film since there is no periodicity requirement. These nanostructures, where subwavelength inclusions of different size, shape and materials are randomly distributed within a bulk matrix, can be called colloids. The optical properties of these colloids can be controlled by controlling the inclusions.

For example, if the inclusions are stimuli-responsive, then the optical properties of the colloid can be tuned by external stimuli. A colloid containing magnetic spheres may respond to a magnetic field. The transmission, reflection, or color of such a colloid can be magnetically tuned in real-time. Similarly, if the inclusions can sustain Mie resonances of different orders, then the colloid can be designed to have a zero or negative effective refractive index. By choosing the inclusions, one can design tunable and controllable optical nanostructures using colloids.

d) Aperiodic planar nanostructures

While planar photonic crystals have many useful and exotic properties due to their periodicity, aperiodic planar nanostructures can be equally useful, despite having no periodicity. In these nanostructures, inclusion materials of different size and shape are aperiodically distributed within a thin-film matrix. For example, the optical density of a planar aperiodic nanostructure can be designed by controlling the size, shape, material, and volume density of inclusions in the matrix thin film. This effect can be used for designing single layer anti-reflection (SLAR) coating where a single layer of a nanostructure with the appropriate optical density may nullify reflectance. The optical density or effective permittivity of the thin film can be controlled by controlling the volume density of inclusion or porosity of the film. Such controllable porous materials have many uses in optics and nanophotonics.

Recently, aperiodic planar nanostructures with a regular arrangement of inclusions have also been used for designing miniaturized and flat optical components. In these nanostructures, the inclusions are arranged to implement a specific spatial distribution of optical density. This way, the emergent optical wave-front can be

engineered to mimic the output of any desired optical component. Thus, well designed aperiodic nanostructures can replace traditional spherical optical components with flat and planar components, giving rise to new, flat component-based optics. Here, the shape of the components is always flat, unlike traditional optics, where the shape of the lens is determined by its application.

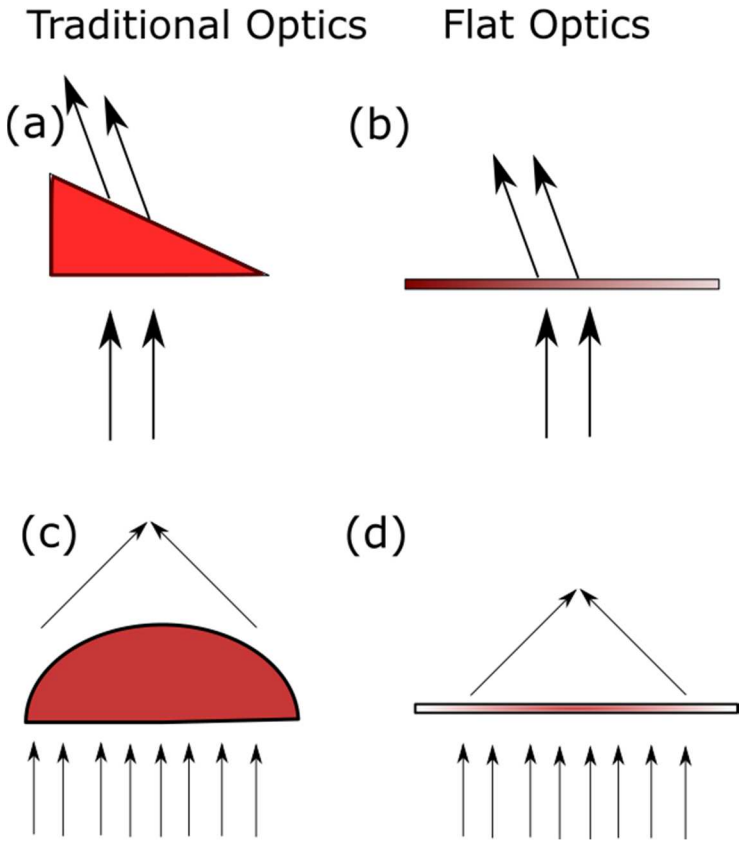

Figure 4 Comparison of regular optics and flat optics

Flat optics and traditional optics are compared in Figure 4. In Figure 4(a), a prism is shown. The degree by which this prism bends the incoming light is decided by its shape, i.e., the acute angle of the prism. In flat optics, light can be bent by a flat film of aperiodic nanostructure with a specific distribution of inclusions, as shown in Figure 4(b). Similarly, Figure 4(c) shows a spherical lens that focuses the incoming light. The focal length of this lens and its efficiency is decided by the shape and material of the spherical lens. On the

other hand, a film of aperiodic nanostructure with controlled distribution of inclusion can achieve the same effect using a flat surface. Flat optics is now a rapidly progressing field. It has generated a lot of interest because planar optical components promise a new integrated optics platform, which can be fabricated with existing technology, and may eliminate long-standing problems of typical optics, such as aberration.

e) Surface nanostructure

Surface nanostructures are surfaces that scatter light due to their optical roughness. It is well known that these rough optical surfaces scatter light in addition to transmitting and reflecting it. By controlling the roughness of the surface, the scattering of light can be controlled and harnessed for many applications. For example, it is well known that rough surfaces reflect less light compared to smooth surfaces. The junctions of solar cells are typically made rough either in a controlled or random manner to enhance photon absorption. Rough surfaces are also better in adsorbing different chemicals such as water. Despite their many applications, surface nanostructures are seldom used in optical applications due to their enhanced ability to scatter light.

f) Materials

While the structure of an optical nanostructure is important, the constituent materials also plays a vital role. The choice of material for an optical nanostructure is limited in practice because of various limitations in the fabrication and production chain. However, it is still important to explore different materials and investigate their usefulness.

The dominant material for designing optical nanostructure is, understandably, silicon. Despite the high loss and opacity of silicon at the visible wavelengths, it is still used due to convenience. Nanostructures designed on silicon can take advantage of the

enormous Si fabrication infrastructure that is already in place. However, the high loss of silicon limits the possible applications of silicon nanostructure in the visible wavelengths. III-IV semiconductors, like InP, GaAs, InGaAs, among others, are possible alternatives to silicon. These materials have a high refractive index and a wide, direct bandgap, making them suitable for opto-electronic application. Significant infrastructure has been built for these kinds of materials, and it is steadily growing. Ultra-high index materials, such as PbTe and Te are also explored for designing optical nanostructures.

However, these materials, despite their advantages, remain highly lossy in the visible wavelengths. Recently, transparent materials, such as SiO_2, TiO_2, and polymers such as Polystyrene, Poly-(9-vinylcarbazole) (PVK), and Poly- (methyl methacrylate) (PMMA) are being explored as candidate materials. In this work, our focus is on low index materials that are highly transparent in the visible wavelengths.

2. ANALYSIS METHODS

Analysis of optical nanostructure means calculating the relevant optical properties of the nanostructure. Typical quantities that are calculated include:

- Reflection, transmission, and absorption
- Scattering, extinction, and absorption efficiencies
- Scattering parameters
- Effective permittivity, effective permeability, and effective refractive indices
- Frequency bandgap, group refractive index, and iso-frequency contours

There are two prominent methods to calculate these quantities: full-wave numerical analysis and analytical analysis. In full-wave numerical analysis, Maxwell's equations are solved numerically, both within and outside the nanostructure, with

appropriate boundary conditions. From the calculated fields, the desired quantities are determined via post-processing. Full-wave numerical methods include the finite difference time domain (FDTD) method, the finite element method (FEM), the finite integral technique (FIT), rigorous coupled wave analysis (RCWA), the transfer matrix method (TMM), and method of moments (MoM). These methods are highly versatile and accurate, but they sometimes fail to provide the desired connection between the optical nanostructure and its optical properties.

These analytical methods, though limited in applicability, may reveal significant insight into an optical nanostructure. These methods use various approximations to derive an analytical relation between the desired quantity and the structural parameters of the nanostructure. Examples of analytical methods include effective medium approximation, Mie theory, scalar wave equation, diffraction theory, etc. In this work, both full-wave numerical and analytical analysis methods are used to design and analyze a controllable and tunable optical nanostructure.

3. IMPORTANCE OF FEATURE SIZE

While numerical and analytical methods can be used to analyze a wide variety of optical nanostructures, these methods are not universally applicable. An important criterion in deciding the analysis method is the feature size of the nanostructure. Numerical methods in general can be very accurate when the features are well-resolved. When feature size is much smaller than the operating wavelength, it is difficult to resolve the features in a numerical analysis. In these situations, numerical methods may require prohibitive memory and time to be accurate. On the other hand, analytical or semi-analytical techniques such as effective medium approximation [6], or scattering

equivalence methods [7] may be sufficiently accurate while requiring much fewer resources.

On the other hand, when the feature sizes are much larger than the optical wavelengths, traditional optical numerical methods such as raytracing can be used. These methods are highly optimized to be memory efficient and accurate. Additionally, analytical approximations may not always be applicable when the feature size is much larger than the operating wavelength.

However, when the feature size is comparable to the wavelength, the advantages and disadvantages of analytical and numerical methods are not very clear. For example, EMA can be very accurate when analyzing nanostructures in this feature range. However, if the nanostructure is periodic or contains resonant features, such as specific shape or arrangement of high index/metallic inclusion, then EMA prediction may be inaccurate. At the same time, numerical analysis of such structures may require significant time and resources, as well as case-by-case modelling of different optical properties. For example, the transmission of such a periodic nanostructure may require one method, while the effective group index may require a completely different one. Furthermore, if such a nanostructure is aperiodic, neither EMA nor numerical analysis may predict it's optical properties accurately, while both could perform predictions that are statistically accurate [8]. Thus, in these cases, careful attention must be paid to the nature of the nanostructure before choosing the analysis method, and experimental verification should be performed if possible. The relation between feature size, wavelength, and analysis method is summarized in Table 1.

Table 1 The relation between feature size (a), wavelength (□) and analysis method

Feature size	Analysis method	Application
$a \ll \lambda$	Full wave Numerical/ Analytical	Anti-reflection coating with controllable refractive index, flat optics
$a \approx \lambda$	Full wave Numerical/ Analytical	Photonic bandgaps, tunable optical windows
$a \gg \lambda$	Geometrical or Physical optics	Traditional optics

B. Literature Review

Optical nanostructures interact with light differently depending on their constituent materials and distribution within the nanostructure. They can have novel properties due to their structure which cannot be obtained using naturally occurring materials. For example, photonic crystals (PC) can have optical bandgaps where certain wavelengths of light cannot penetrate the medium. Specially designed optical nanostructures can have a negative refractive index, bending refracted light away from the normal. Such properties are highly useful in many fields of application and can only be found in optical nanostructures.

The optical properties of nanostructures can be changed by tuning the material properties of their constituent material. For example, by changing the refractive index of the photonic crystal matrix material, its bandgap frequencies can be shifted [3, 9]. Changing the surface charge density of graphene results in change in the permittivity of the material. Controlling the interparticle distance of a magnetic crystal can change its diffractive properties [10]. However, such tunability requires stimuli-responsive materials, which are limited. In general, changing the constituent material to control the optical

properties is limited by the availability of suitable materials. A more versatile method is needed to control the optical properties of a nanostructure. One such method could be changing the spatial configuration of the nanostructure. Even though the choice of suitable materials is limited, by controlling the spatial configuration of the optical nanostructure, many novel properties can be realized. Thus, designing the configuration of materials is crucial when designing an optical nanostructure with the desired optical properties. Control over optical properties such as the refractive index, permeability, permittivity, reflectance, and transmittance of the nanostructure can lead to useful and novel applications.

Efficient design and analysis are crucial for designing a controllable optical nanostructure. The number of design variables in an optical nanostructure is large, and the relation between these variables and the different optical properties of the nanostructure is not readily apparent. Thus, the design and analysis process must iterate until the desired properties are achieved. Unless an efficient design and analysis process is devised, this process may take a long time.

Our goal is to design an optical nanostructure with controllable and tunable optical properties efficiently. However, there are several crucial gaps in the technology that have been prohibitive. Typically used materials to design optical nanostructures are highly lossy in the visible wavelengths. Low loss and transparent materials with low refractive indices are only now garnering significant attention. Also, the analysis of an optical nanostructure is commonly carried out using numerical analysis, while the analytical methods are not fully developed.

In this chapter, we discuss the state of the art of low loss optical nanostructures and analytical methods to analyze them. Different strategies and their shortcomings for solving these problems are reviewed, and finally, the scope of future work is discussed.

1. LOW LOSS OPTICAL NANOSTRUCTURES

In this section, we review the available literature on different nanostructures on low loss material.

a) Photonic Crystals

Photonic crystals can utilize the periodicity of their lattice to manipulate light in many ways. For example, it is possible to create a band of frequency where light cannot propagate, or light interacts anomalously due to resonance. These effects are generally associated with high loss. However, photonic crystals with low loss, which is our focus, have also been reported to produce such effects.

Optical bandgap is one of the most useful of these anomalous effects. Because of multifaceted applications of optical bandgap, the materials that can support this property have found widespread use in all forms of technology. Optical bandgap is typically associated with high refractive index materials, which are relatively lossy at the optical wavelengths. However, low loss materials like glass, polymers, silica, etc. have also been reported to produce optical bandgap.

Interestingly, one of the earliest reports of optical bandgap dates to the 19th century. John William Strutt, commonly known as Lord Rayleigh, published a treaty in 1892 in which he discussed a periodic stack of dielectrics as a perfect mirror [11]. The mathematical framework required to solve Maxwell's equations was not available at the

time. Lord Rayleigh arrived at the correct solution by treating it as a multiple reflection problem. Later, Floquet [12] and Bloch [13] discovered the mathematical framework required to solve the Maxwell equation in a periodic medium. Using this approach, it was discovered that electromagnetic waves cannot propagate in a periodic medium in a specific frequency band [14].Early utilization of this property was limited to a periodic stack of materials. For example, a thin-film laser using the Bragg waveguide was proposed in [15].

A breakthrough in the study of periodic materials came in 1987, when it was theoretically predicted that a three-dimensional periodic medium can inhibit spontaneous emission from a material if the electronic bandgap of the material falls within a certain range of frequency, dubbed the electromagnetic bandgap. The omnidirectional nature of this electromagnetic bandgap was discussed in the literature [16], and it was predicted that such a property could be realized in a three dimensionally periodic medium if the constituent materials had sufficient contrast of the refractive index [16]. This treatise is the genesis of the modern photonic bandgap. Around the same time, it was discovered that even a random medium containing dielectric inclusions can have a forbidden band of frequency [17], further verifying the discovery in [16]. Early attempts to verify this prediction included full vector wave calculation of the photonic band structure of a face centered cubic (FCC) lattice. Early calculations, based on FCC lattice, found no evidence of a bandgap [18]. However, when the diamond lattice was investigated theoretically, the first evidence of a photonic bandgap was found [19]. At that time, it was established that to obtain omnidirectional optical bandgap, a refractive index as high as 3.5 to 3.6 would be necessary, which precludes most low loss materials.

Although the theoretical existence of a photonic bandgap for certain lattices was established beyond any reasonable doubt, the experimental demonstration of a complete photonic bandgap remained a challenge. Early demonstration of complete photonic bandgap included the FCC lattice of non-spherical atoms, which was fabricated by drilling each hole of a mask containing a triangular lattice of holes three times along the directions of FCC lattice axes [20]. In this calculation, it was revealed that a refractive index as low as 2.1 may sustain a complete optical bandgap. This was the first indication that low loss and low index materials may be able to sustain complete or incomplete bandgaps. The image of the structure is reproduced from [20] in Figure 5(a). A simpler structure was proposed using a layer by layer fabrication method, which was able to produce the first micron scale photonic crystal with a complete bandgap [21]. The image of the structure is produced from [21] in Figure 5(b). In this arrangement, the required refractive index for opening bandgap was further reduced to 1.9. The layer by layer structure was successfully scaled down from 12 □m to 1.6 □m in [22], the image of which is reproduced in Figure 5(c). Despite the progress in reducing the loss, most promising structures were still high index self-assembled inverse opals because they could be easily of fabricated, as discussed in [23]. An example is shown in Figure 5(d), which is reproduced from [23].

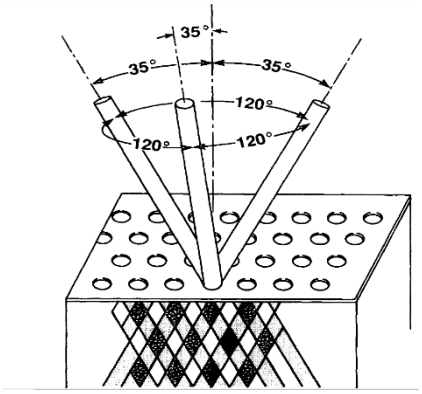

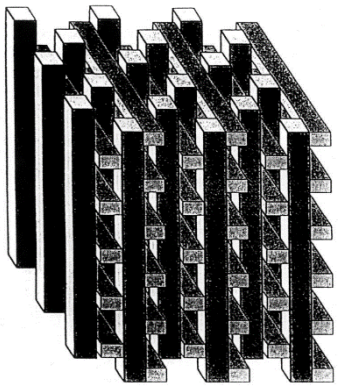

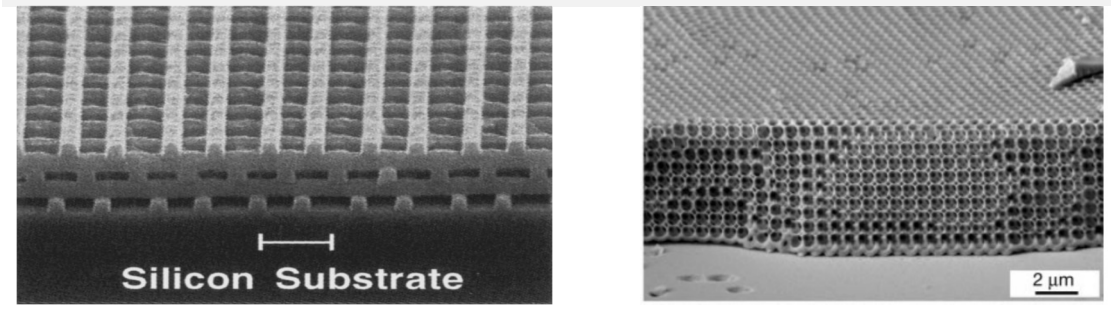

Figure 5 Early experimental realization of photonic crystals with complete bandgap [20-23]

Although a low loss complete bandgap has been experimentally demonstrated in three dimensional photonic crystals, fabricating three dimensional periodic structures remains a challenging task, especially when the visible part of the spectrum is the relevant wavelength. Planar photonic crystals (PPC), where the material is periodic in a two-dimensional plane and uniform in the other, have emerged as a viable alternative because they are easier to fabricate.

Planar photonic crystals have been widely studied, and a variety of applications have been developed, including a high quality-factor cavity for lasing and sensing [24-26], waveguides with sharp bends [27], subwavelength imaging [28], emission control [29] and negative refraction [30, 31]. However, unlike the 3-D photonic crystals, the materials used for fabricating such bandgap structures remain high refractive index materials, as shown in Table 2, which are highly lossy in visible wavelengths. The prevalence for high index material may be caused by the ease of their fabrication. Progress in nanofabrication may render the low index and low loss materials viable candidates for optical bandgap.

Table 2 Application and materials for planar photonic crystal.

Material	Application	Reference
Silicon	Ultra-high Q cavity	[24]
Indium Phosphide	Negative refraction	[30]
Silicon on insulator	Refractive index sensor	[25]
Silicon	Low loss bend waveguide	[27]
High index material (n = 3.1)	Subwavelength imaging	[28]
Gallium Arsenide	Spontaneous Emission control	[29]
Indium Gallium Arsenide Phosphide	Defect based cavity	[26]

Historically, low loss materials like glass and polymers have many uses in optics. For example, a low loss silica waveguide based interferometer has been shown to easily couple with silica fibers [32]. Fiber Bragg grating was demonstrated as an integrated reflector in silica fiber [33]. Low loss couplers based on silica waveguides have also been reported [34]. A high performance laser has been reported on transparent polymers [35]. Fiber optics have been progressing rapidly, and transparent optical devices remain among the most utilized and studied devices.

With the ubiquity of handheld devices covered with transparent screens, the importance of transparent active materials has increased significantly. Effort has been underway to fabricate nanophotonic devices on glass and polymers. For example, a temperature sensor built on Gorilla Glass, which is the glass used on most cell phone screens, has been reported [36]. The sensor was built using a low loss waveguide fabricated on the glass surface. The waveguide, reproduced from [36], is shown in Figure 6.

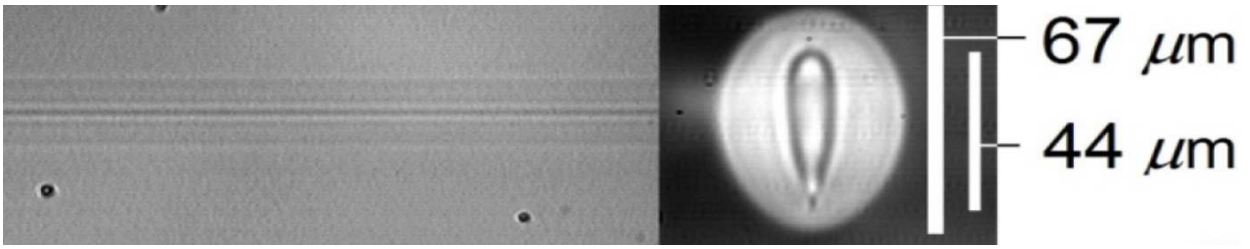

Figure 6 Low loss waveguide on Gorilla Glass. The top view is shown on the left, and the facetted view is on the right [36].

Despite the renewed interest in low index functional material, a photonic crystal device on glass or polymer has not yet been reported. The available literature shows some success in creating photonic crystals with a partial bandgap. For example, a triangular lattice of air cylinders was fabricated on a glass matrix, and a partial photonic bandgap near infrared was demonstrated [37]. Partial bandgap was reported for visible wavelength (514 nm) using a triangular lattice of airholes with 220 nm period in a glass matrix with refractive index 1.46 [38]. Partial bandgaps have also been reported with methyl pentene, which is transparent with a refractive index 1.45 [39]. Thus, there is precedence in the literature where transparent and low index glass and polymers have been used for producing partial bandgap. However, a complete in-plane bandgap using transparent materials has not been reported. Such a device may have many potential applications in communication and sensing.

b) Optical Metamaterials

While optical bandgap emerges from collective diffraction in a periodic lattice, the interaction between the periodic lattice and incident light may produce other anomalous effects when the lattice is deeply subwavelength. These subwavelength periodic nanostructures are called optical metamaterials, which are different than photonic crystals which have periodicity comparable to operating wavelength [40]. These metamaterials

may produce an anomalous refraction, where light is refracted with a near-zero or negative refractive index, which can be harnessed for different applications including imaging, wireless communication, and sensing.

Initial demonstrations of optical metamaterials harnessed the plasmonic resonances in metallic nanoresonators to obtain these exotic effects. However, being metallic, these devices suffered from Ohmic loss [41]. To minimize loss, the Mie resonances in high-dielectric materials have been proposed as an alternative [41]. In such nanostructures, the shape of the resonator plays an important role, because Mie resonance is highly morphological [42, 43]. Different shapes of dielectric resonators are employed in the literature. In these resonators, electric (E) and magnetic (H) type resonances, oriented perpendicular to each-other, interact to produce anomalous reflection and transmission. The typical shapes of the resonators and the two types of resonances possible in them are shown in Figure 7, reproduced from [44].

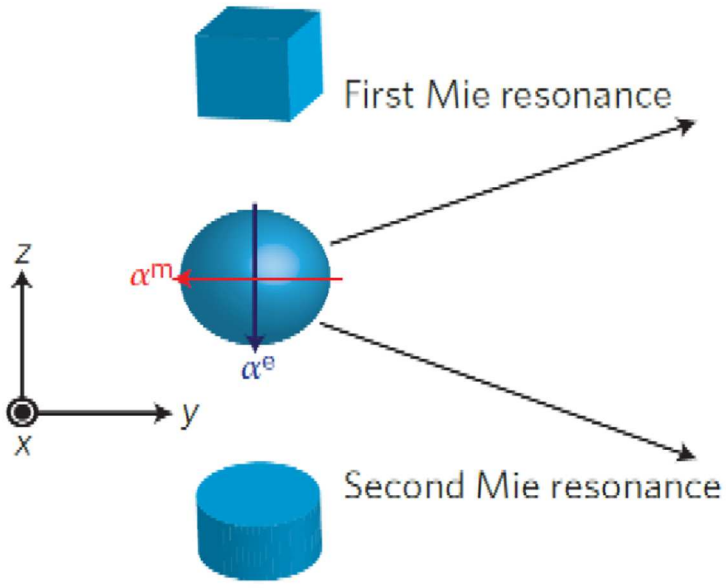

Figure 7 Unit cell of a dielectric resonator [44]

The E type and H type resonances are analogous to the transverse electric and transverse magnetic resonant modes [45]. An E type resonance is associated with anomalous effective permittivity, and an H type resonance is associated with anomalous effective permeability. An array of Mie resonators can sustain anomalous parameters in different frequencies. The effective parameters of an array of silicon spheres with 150 nm radius and volume filling fraction 0.3 are shown in Figure 8.

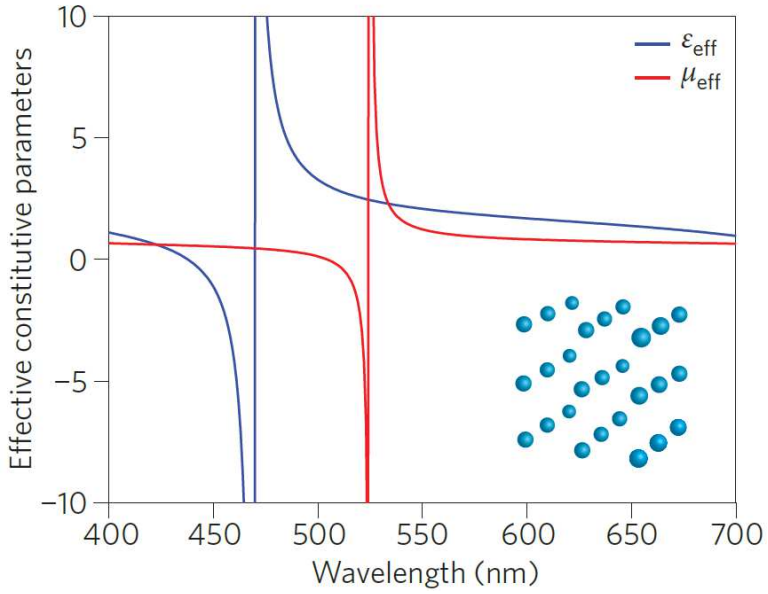

Figure 8 The effective parameters of an array of Si Spheres [44].

Similarly, a 3D array of dielectric resonators has been demonstrated [42]. The array of resonator has anomalous effective permittivity and anomalous effective permeability at the first and second Mie resonance, respectively.

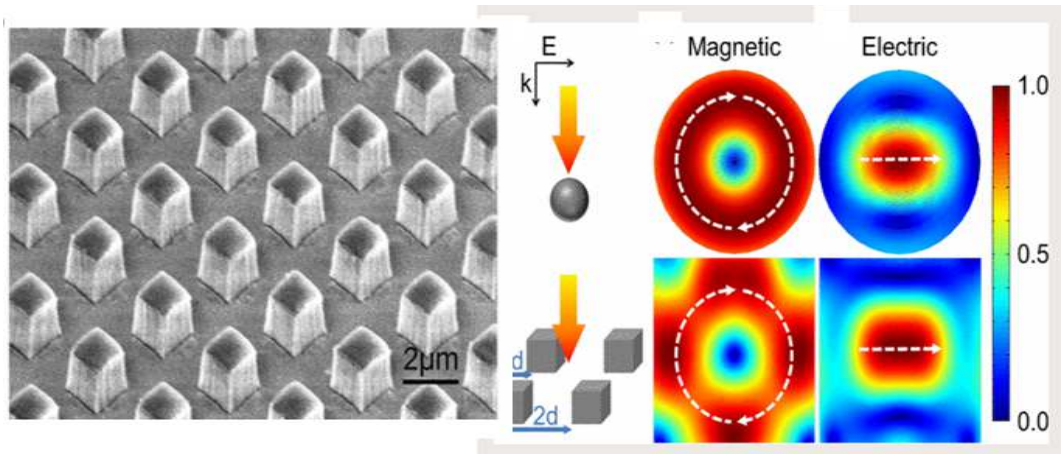

(a)

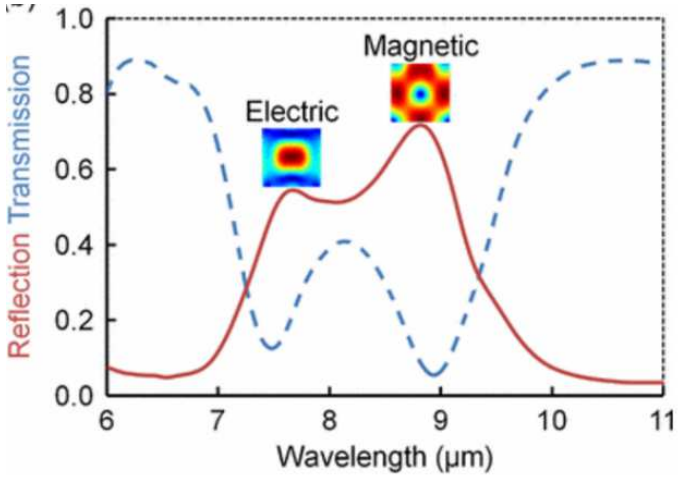

(b)

Figure 9 (a) The first two Mie resonances of an array of Te cubes. (b) Mie resonances of the same structure in a reflection curve[46] .

Electric and magnetic Mie resonances have also used an array of Te cubes, as shown in Figure 9 [46]. It is evident that a simple dielectric resonator can sustain either anomalous permittivity or anomalous permittivity at a given frequency. To obtain anomalous refraction, one must have both at the same frequency. A single resonator simultaneously sustaining anomalous permittivity and anomalous permeability in the visible frequencies has not yet been reported. Recently, it has been shown in a microwave

regime that with very high permittivity (~100), a single resonator can sustain both electric and magnetic resonance simultaneously [47]. The effective parameters of an array of high permittivity cylinders is shown in Figure 10 to have simultaneous anomalous μ and ε. However, a material with such high permittivity in the visible frequencies has not yet been reported. In addition to high index dielectric resonators, coupled resonators have emerged as a new avenue of research that has many promising applications [48, 49].

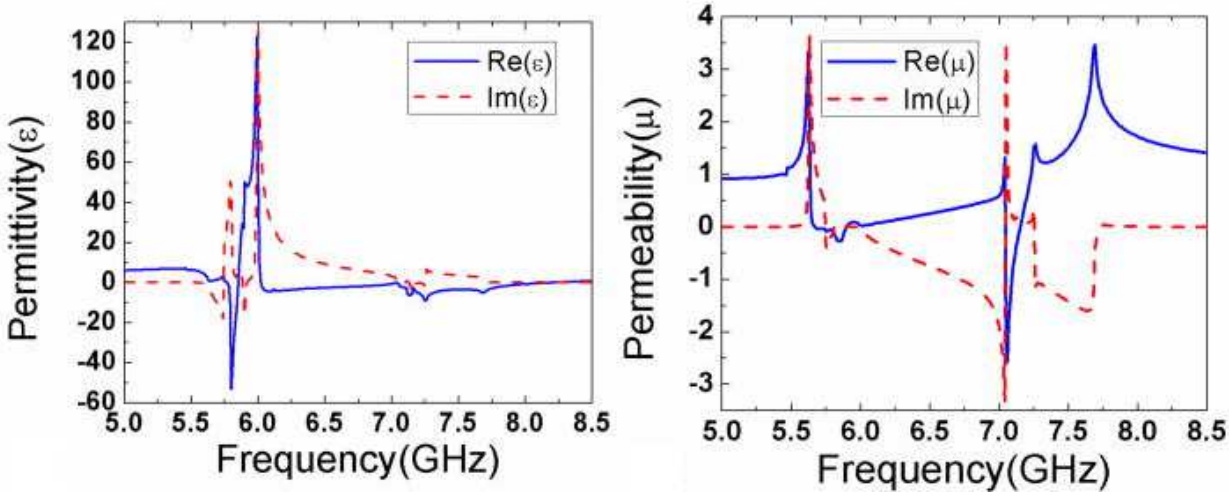

Figure 10. The effective parameters of an array of ceramic cylinders with ε ~100 [47] .

Based on this discussion, anomalous effective parameters may be obtained using high index dielectric materials, as summarized in Table 3. However, a demonstration of these effects in planar periodic optical nanostructure using low loss dielectrics in the optical wavelengths is yet to be reported.

Table 3 Materials for optical Metamaterial

Permittivity	Reference
Si (11.68)	[44]
12	[42]

Te (~24)	[46]
~100	[47]

c) Colloids

While periodic nanostructures show many exotic and useful properties, the requirement of periodicity is difficult to maintain in practice. Colloids, where small islands of inclusion materials are scattered within a matrix material without maintaining lattice periodicity, can be a more practical alternative. For example, when designing periodic nanostructures, the medium must be 3-dimensional in order to be isotropic. Furthermore, the dielectric inclusions must be much smaller than the wavelength of light. Thus, fabricating these kinds of structures is difficult, and fabrication feasibility is often the deciding design parameter. Conversely, a colloid offers an advantage in fabrication because the dielectric inclusion can be randomly distributed in the host. In addition, the inclusions can be separately designed with varying size, shape and distribution. The effective parameters of such random colloids can be extracted using effective medium approximations. In this section the available literature on such colloidal optical nanostructures is discussed.

Frequency bandgaps in photonic crystals are a direct consequence of the lattice periodicity of the nanostructure. In colloids, frequency bands do not form. However, bandgaps can still emerge in such a nanostructure. It has been shown that forbidden frequency bands emerge even when the nanostructure is completely random. In fact, the emergence of permissible frequency bands is the true impact of periodicity since forbidden bands are already present in the random nanostructure [50]. For example, in

Figure 11, the transmission through periodic and aperiodic stacks of dielectric is plotted. Forbidden bandgaps can be achieved using low dielectric materials in a random arrangement.

Unlike frequency bandgap, an anomalous effective parameter can be difficult to obtain in a colloidal nanostructure. A periodic nanostructure harnesses lattice periodicity to obtain modes with a negative or near-zero group index [51]. In fact, it has been argued that the leaky Bloch mode in a periodic lattice plays a central role in the anomalous optical behavior of metamaterials rather than any Mie resonance {Ko, 2018 #690}. In the absence of lattice periodicity and Bloch modes, anomalous effective parameters must be obtained using Mie resonators with E and H type resonances in a matrix medium. It is often difficult to design Mie resonators that can provide resonance of permittivity and permeability in the visible spectrum simultaneously without needing periodicity. The problem is further exacerbated by the fact that the resonances of both permittivity and permeability cause

loss in the resonant wavelength.

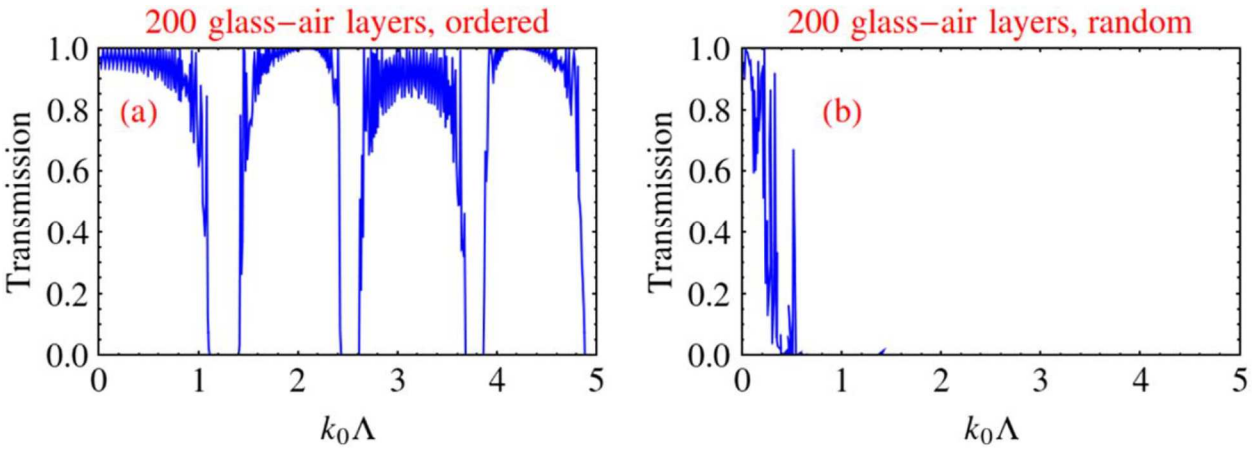

Figure 11 (a) The forbidden and permissible frequency band in a periodic dielectric stack, (b) the forbidden frequency band in an aperiodic dielectric stack.

Many strategies have been employed to solve this problem. One approach is to have one type of inclusion which provides the E type resonance at a frequency range and another which provides the H type resonance in the same range. For example, a colloidal optical nanostructure consisting of $LiTaO_3$ spheres and n-type Ge spheres was proposed [52]. The $LaTiO_3$ spheres supplied the magnetic resonance, and the Ge sphere supplied the electric resonance. The effective refractive index, calculated using long-wavelength effective medium approximation, is reproduced here from [52] in Figure 12. It can be noted that by carefully designing the resonance of the two inclusions, it is possible to obtain a negative refractive index. However, the frequency and bandwidth of the negative refractive index remain limited by the material property. For example, in [52] the negative index was obtained near the optical phonon frequency of the $LaTiO_3$ sphere, ω_T = 26 THz, which is a fundamental property of the material. As such, the negative index obtained by using this combination of material will always be around 26 THz.

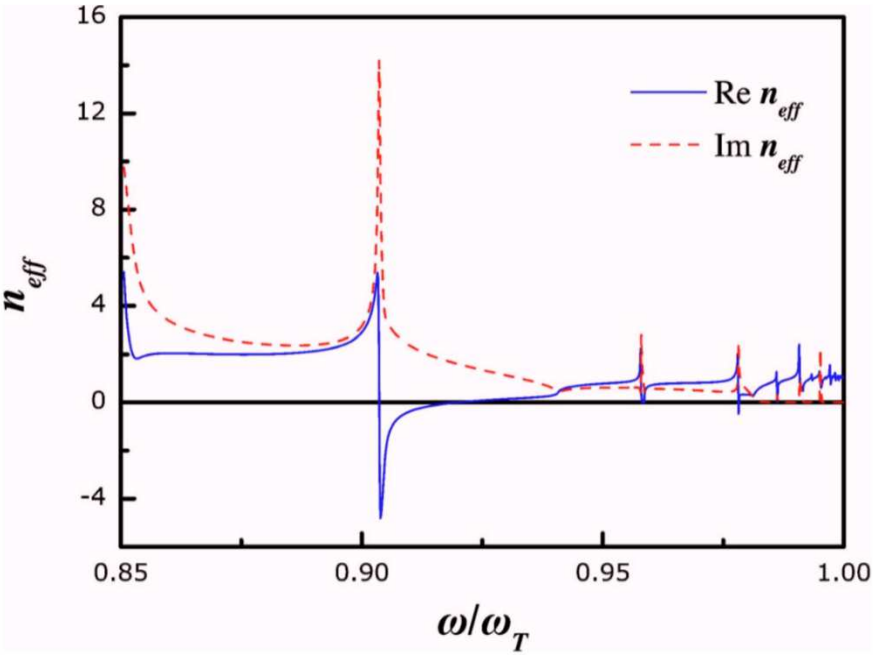

Figure 12. The effective refractive index of the optical nanostructure proposed in [52].

A similar approach is taken in [53], where the two materials supplying electric and magnetic resonance are part of the same sphere in a core shell manner, as shown in Figure 13. The inclusions consist of a core and a shell, each having different material properties. By choosing the configuration of the inclusion, it is possible to obtain negative refraction as shown in Figure 13. However, as discussed before, this approach is limited by the available materials.

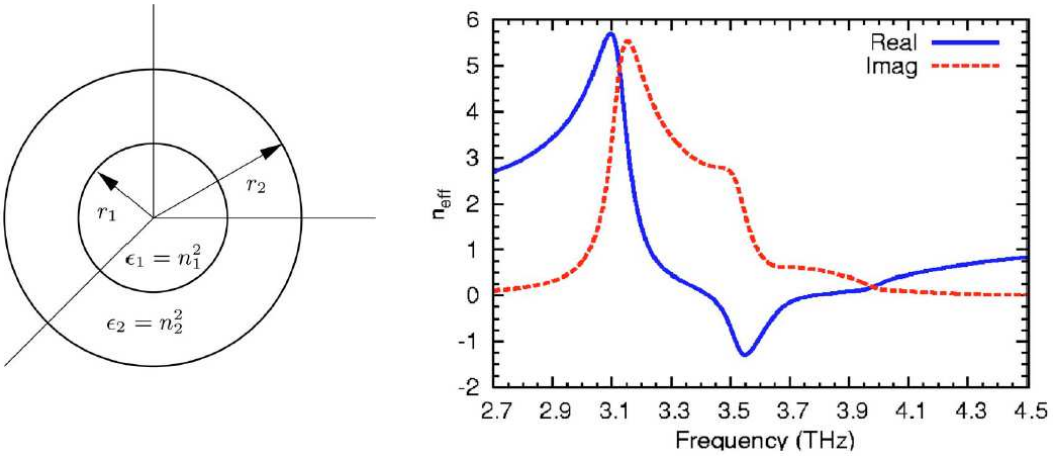

Figure 13. The schematic of core shell type inclusion and the effective refractive index of a medium having such inclusion is shown [53].

Alternatively, instead of completely relying on the Mie resonance, one can have a host material with negative permittivity, such as MgB_2, and an inclusion designed for negative effective permeability [54]. In Figure 14, where a colloid of MgB_2/SiC is shown, both the s and p polarization of light shows a dip in reflectivity. This indicates that both the s and p polarization of light couple with the surface plasmons, indicating that both permittivity and permeability are negative. However, although negative refraction is possible in this structure, sic is lossy at the visible frequency. Thus, the colloid would have a high loss as well.

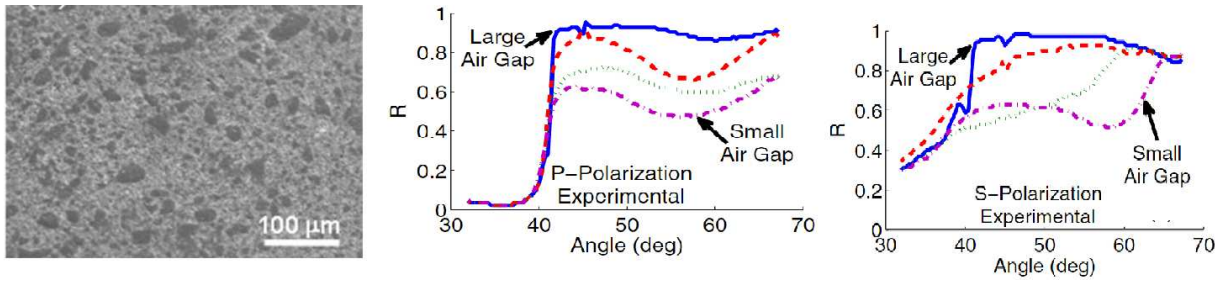

Figure 14 The structure of the MgB_2/SiC composite is shown on the left. The reflection of the material for different angles of incidence with s and p polarization of light is also shown [54].

As an alternative to SiC, other high permittivity materials like Si or Ge can be used to produce effective negative permeability through Mie resonance. Recently, viral capsids have been proposed as a high permittivity material in designing negative index optical nanostructures [55]. Capsids are highly attractive because they can have permittivity ranging from a few decades to thousands depending on the density of their RNA. The effective refractive index of a material containing gold nanoparticle and viral capsids is shown in Figure 15. By changing the permittivity of the capsid, negative refraction can be obtained in different frequency ranges.

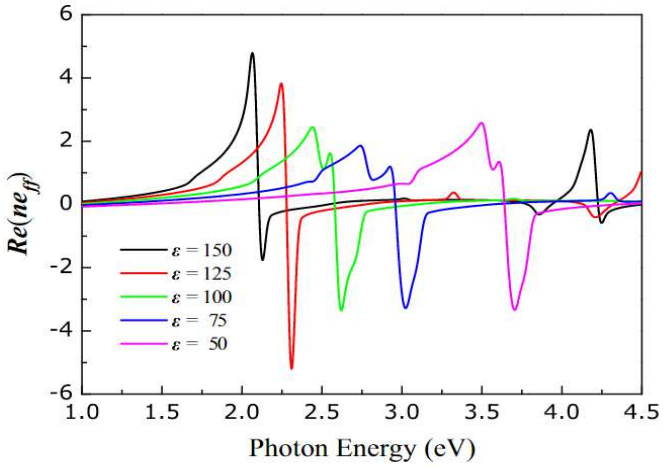

Figure 15 The effective refractive index of the medium containing capsid inclusion and MgB_2 host [55].

While the instances of anomalous refraction discussed above using all-dielectric nanostructure are less lossy than their metallic counterpart, they remain lossy in the visible wavelengths. In fact, since anomalous refraction relies on a strong scattering of light by the medium, it may not be possible to eliminate the loss in such a process. Unlike anomalous refraction, there are many properties of a colloid for which weak scattering is enough. These properties can be utilized for a great many applications. For example, aperiodic nanostructures can have controllable and tunable optical density. This may be harnessed in designing devices such as tunable optical window, anti-reflection coatings and nanostructured flat optical elements.

Optical windows can control and restrict the intensity of the light transmitted through them. These devices are useful in designing smart household windows [56], limiting laser output and filters for optical application [57]. When the transmittance of these windows is externally tunable, they can be called tunable windows. Optical colloidal nanostructures have been used as tunable windows. For example, a tunable window was proposed by fabricating nanopillars on a wrinkled elastomeric polymer film[58]. The transparency of the window can be controlled by mechanical strain. The strain tunable transmission of the window is reproduced from [58] in Figure 16(a).

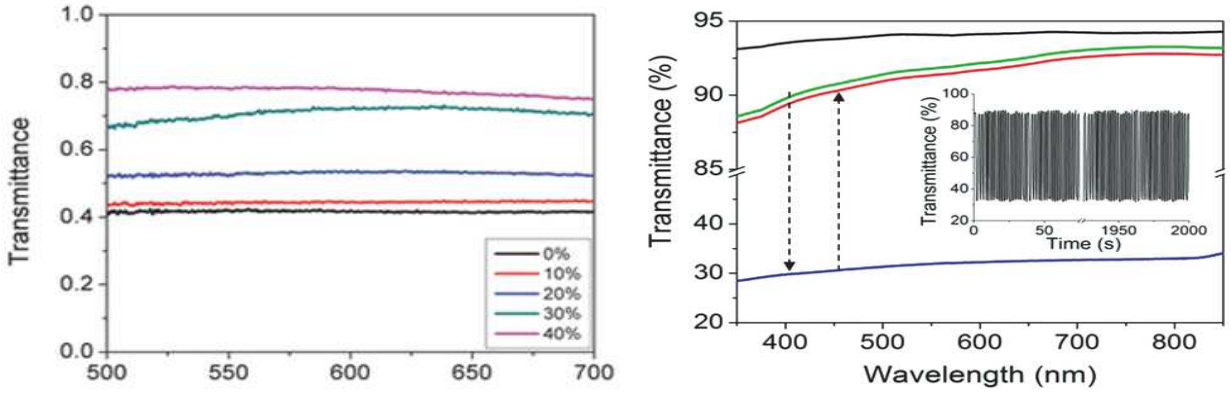

(a) (b)

Figure 16 Transmission of the strain tunable window when different levels of strain are applied.

Silica nanoparticle embedded elastomer film has also been reported as a strain tunable window [59]. The switchable transmission from such a window is reproduced from [59] in Figure 16(b). An electric field tunable window was reported in [60] using a suspension of TiO_2 nanowires in a viscous polymer. The tunable transmission is shown in Figure 17.

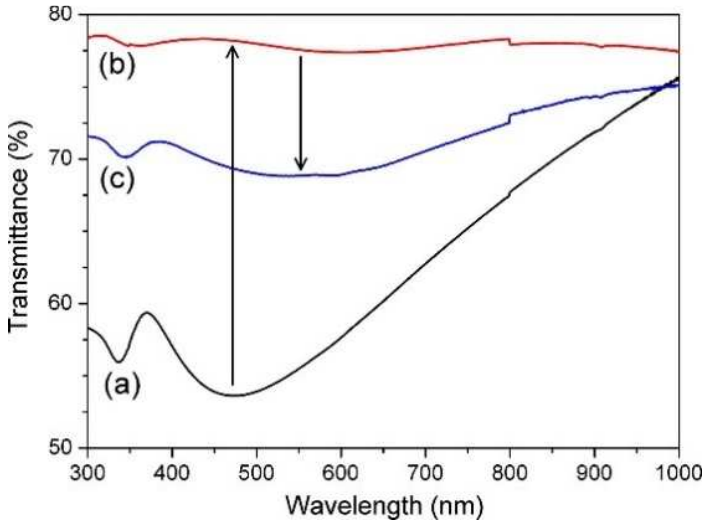

Figure 17 The tunable transmission of the TiO_2 nanowire suspension in polymer under (a) no electric field, (b) perpendicular electric field, and (c) horizontal electric field [60].

The windows demonstrated above do not require any naturally stimuli-responsive material. However, these structures require complicated and expensive fabrication procedures. Their tunability range is also limited. Furthermore, many of the structures are thermally or chemically unstable. Magnetic microsphere colloids (MMC), due to their thermal and chemical stability as well as their quick and inexpensive preparation [61], are a good alternative material for tunable optical windows.

MMC are aperiodic optical nanostructures that can be controlled with an external magnetic field. Generally, the magnetic field controls the structure of the colloid, including its local density and orientation of the magnetic particles. Magnetic field sensitivity of an MMC solution has been utilized for many diverse applications including cancer treatment [62], waste treatment [63], drug delivery [64, 65], petroleum processing [66], and MRI contrast enhancing [67]. Now, optical applications of MMC as a magnetic field tunable optical nanostructure have also garnered attention.

A magnetic crystal was reported, the lattice constant of which can be controlled by an external magnet, resulting in a magnetically tunable optical nanostructure [68]. A colloid consisting of superparamagnetic nanocrystal clusters was reported which diffracted different wavelengths of light depending on the applied magnetic field [10]. A photonic crystal consisting of magnetic colloids in a nonpolar solvent was reported [69], which displayed magnetically tunable reflection and color. An aqueous solution of magnetic nanoparticle was demonstrated which showed magnetically tunable reflection [70]. A magnetic colloidal double heterostructure photonic crystal was reported with magnetically tunable optical properties, which was used as a photonic label [71]. The magnetically tunable reflection and color of magnetic nanoparticle colloid are reproduced from [69] in Figure 18.

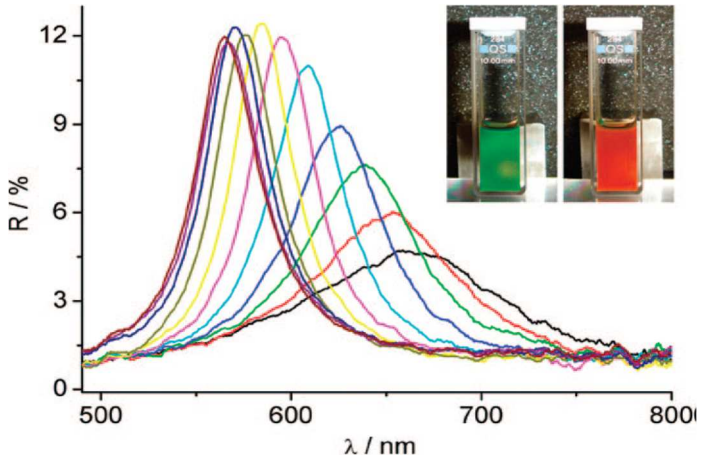

Figure 18 The tunable reflection and color of a magnetic nanoparticle colloid [69].

Although the structures discussed above are highly tunable and easily produced, they are highly sensitive to angle and polarization. As such, they have limited application as optical windows. On the other hand, the transmission of aperiodic magnetic colloids is insensitive to incident angle and polarization [72]. For example, a colloid of Silica wrapped Fe_3O_4 nanoparticles is shown in Figure 19(a). The reflectance and transmittance through this colloid can be controlled simply by applying magnetic field, as sown in Figure 19(b) and (c). Magnetic colloids can also be used to design tunable mirrors by conjugating such colloids with micro-mirrors [73].

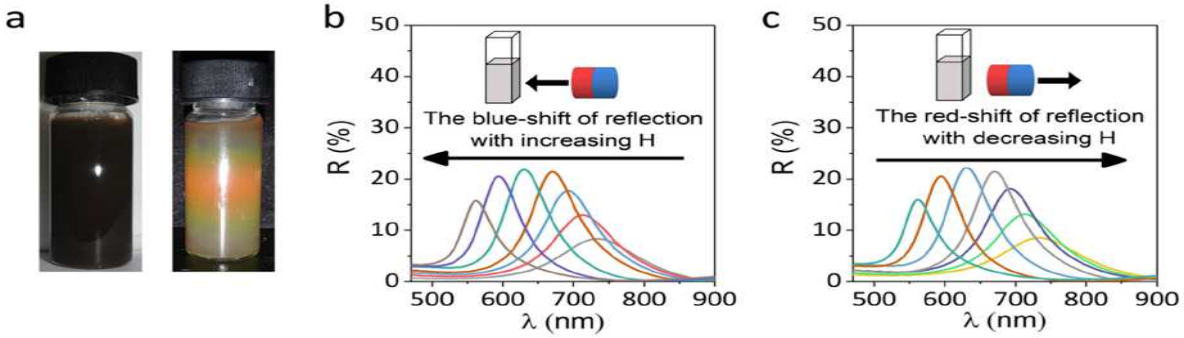

Figure 19 (a) Magnetic colloids of Fe_3O_4 before and after exposure to magnetic field, (b) Change in reflection with increasing magnetic field, (d) change in reflection with decreasing magnetic field [72].

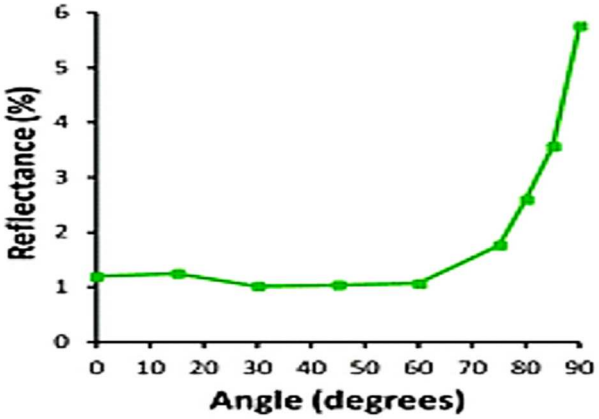

Figure 20 The tunable reflection of an Au micromirror conjugated with magnetic colloids [73].

The functionality of the magnetic colloids derives from the fact that the local density of the colloids can be dynamically controlled by a magnetic field. Tunable magnetic field can be applied on the colloid through magnetic catch-and-release systems. Reported catch-and-release systems include perpendicular current carrying conductors, ring traps [74], differential magnetic field [75],and permanent magnets[76].

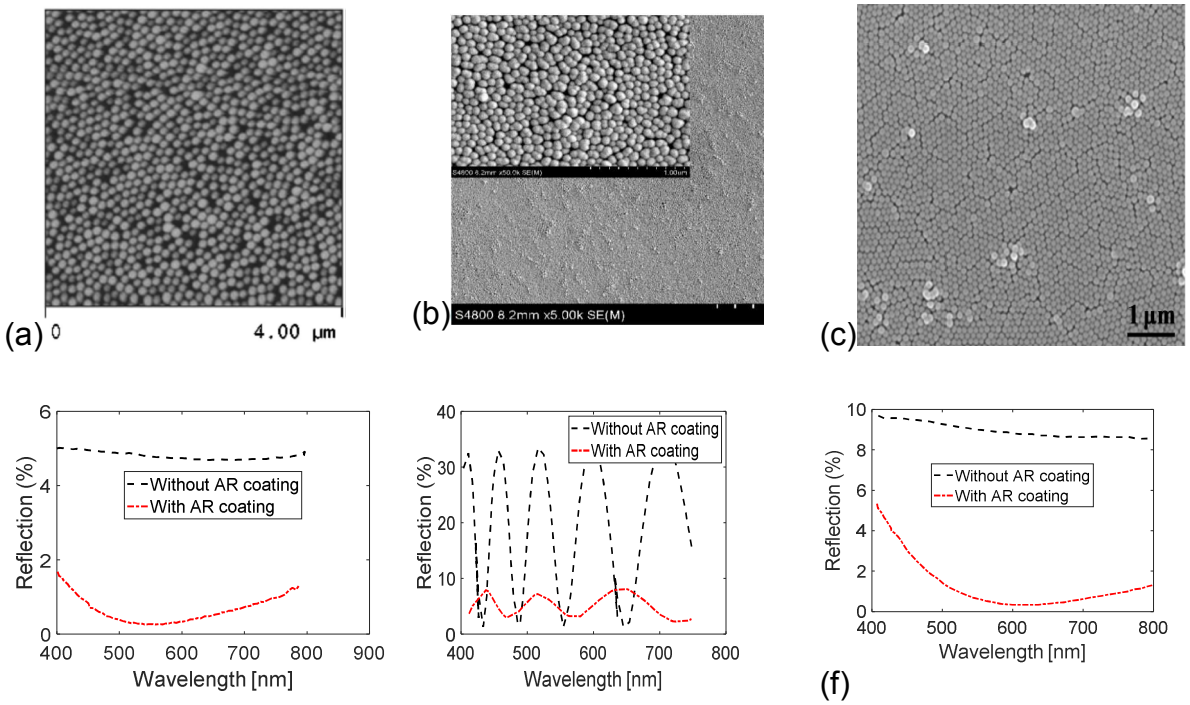

(d) (e)

Figure 21 The aperiodic nanostructure used as AR coating in (a) [77], (b) [78], and (c) [79]. (d-f) shows the respective reduced reflection.

d) Aperiodic planar nanostructure

While dynamic control of local volume density can be harnessed to design tunable optical nanostructures, static control of the same can be used for many applications, including nanostructured optical components, anti-reflection coating, and absorption/adsorption layer. In these optical nanostructures, even though there is no lattice periodicity, the distribution of inclusion is controlled. Since these nanostructures require careful fabrication, these are almost always planar.

Such planar nanostructures span only a single or several layers and are very thin along the propagation direction. However, the planar distribution of inclusion with the nanostructure may modify the intensity, polarization or phase of the transmitted wave [80]. An early example of such a planar nanostructure is the single layer anti-reflection coating [77-79]. Here, the reflection from a substrate is reduced by coating it with a planar nanostructure so that the impedance mismatch at the interface is minimized. The impedance matching is achieved by controlling the effective refractive index of the nanostructure via its local volume density or filling factor. Recent progress in this field has led to wave-front engineering, wherein the wave-front of an incident wave can be manipulated arbitrarily by aperiodic planar nanostructures to achieve the desired effects including focusing, imaging, vortex generation, holography and dispersion control [81-86].

These aperiodic planar nanostructures, with specific arrangement of inclusions, can miniaturize complex optical components into subwavelength optical lenses. They are important because of their thin, often planar geometry and suitability for integrating into optical chips in the visible wavelengths. Furthermore, the aberration of such nanostructure optical components can be controlled because there are many design parameters to optimize including the orientation, physical structure and height of the inclusions within the nanostructure [87-90].

Early demonstration of such subwavelength optical lenses used metals, which were highly lossy in the visible wavelengths [91, 92]. Non-metallic optical lenses using high index materials like silicon [90], lead telluride (PbTe) [93], graphene [94], van der Waals materials like molybdenum disulfide (MoS_2), and hexagonal boron nitride (hBN) [95] have been demonstrated for THz, infrared, and visible wavelength ranges. These materials are limited by loss at the visible wavelengths. Materials that are highly transparent are much desired candidates for subwavelength optical lenses in the visible wavelengths although their low refractive index can present challenges for implementation. Recently, moderately low refractive index subwavelength optical lenses have been demonstrated using Si_3N_4 [84], TiO_2 [88, 89] and photoresist [96].

Like periodic optical nanostructures, aperiodic nanostructures may also be highly useful if they can be implemented in low index materials like glass and transparent polymers. Diffractive optical lenses [97, 98] have been demonstrated using such materials. However, planar aperiodic nanostructures using glass and polymers are rarely analyzed in detail. In subsequent chapters, we will address aperiodic optical nanostructures in detail.

2. ANALYTICAL ANALYSIS METHOD

Optical nanostructures require careful and accurate analysis before as well as after performing experiments. This is because there is no straight-forward relation between the properties of a nanostructure and its morphology and structure. Additionally, there can be numerous parameters when designing an optical nanostructure, and the interplay between them may not be obvious. Hence, numerous methods have been developed to analyze optical nanostructures. They can be divided into two types: full-wave numerical and analytical. Full-wave numerical analysis methods rely on using different numerical techniques to calculate the electric and magnetic field within and outside the nanostructures. There are several mature, stable, and versatile numerical techniques available that can analyze optical nanostructures, such as finite difference time domain method, plane wave expansion method, transfer matrix method, rigorous coupled wave analysis method, among others. A detailed discussion of these computational methods and their implementation is out of the scope of this work. Implementation and discussion of these methods can be found in [99].

The drawback of these numerical methods is twofold. First, these methods, while being extremely accurate, do not reveal the interplay between the physical structure and optical properties of a nanostructure. Second, these methods may require a prohibitive amount of time and computational resources to produce sufficiently accurate results. Analytical methods, on the other hand, do not have these drawbacks. In analytical methods, the optical nanostructures are simplified by reasonable assumptions, and the relation between their optical properties and physical structure is derived analytically. These methods provide valuable insights into the interplay of the design parameters while

also being very fast. They also do not require many resources to implement. However, the speed and ease of development come at the cost of accuracy.

One type of analytical method is effective medium approximation (EMA) where the optical nanostructure is approximated by an optically equivalent effective medium. Accurate effective medium approximation of an optical nanostructure remains an open problem. Currently, effective medium approximations require the assumption that the nanostructure is greatly dispersed, and the feature size is very small compared to the wavelength. Even with these limitations, EMA has been successfully employed to study optical nanostructures for different applications, including anti-reflection coating [77], thermo-photovoltaics [100] and all-dielectric metamaterial [101]. EMAs treat optical nanostructures as a homogeneous medium with effective optical properties, which are functions of the constituent materials and their distribution. The available literature on commonly used effective medium approximation of heterogeneous materials and their applicability are discussed below.

One of the first EMAs was proposed by Maxwell-Garnett in 1904 [102] while discussing optical properties of glass containing small metallic inclusion. In [102], it was assumed that the metal inclusions were very small and spherical in size. They were approximated as point dipoles, which are much smaller than the wavelength. The static polarizability of the point dipole was calculated, and then the polarizability of the medium was estimated as an average of the polarizabilities of individual inclusions. From the effective polarizability, the effective permittivity of the optical nanostructure was explicitly calculated. Let us consider an optical nanostructure where the matrix material has a

relative permittivity of $m_{at,}$ and the spherical nanoparticle inclusions have a relative permittivity of z_{inc}. The dipole polarizability of the nanoparticles can be deduced as

$$\alpha = 4\pi R^3 \frac{\epsilon_{inc} - \epsilon_{mat}}{\epsilon_{inc} + 2\epsilon_{mat}}$$

where α is the dipole polarizability of each nanoparticle and R is the radius of the nanoparticles. The effective relative permittivity (ε_{eff}) of the ensemble can be evaluated from the Claussius-Mossotti (CM) equation:

$$\epsilon_{eff} = \epsilon_{mat} \times \left(1 + \frac{n\alpha}{1 - \frac{n\alpha}{3}}\right).$$

Here, n is the volume density of the inclusion nanoparticle. Although the Maxwell-Garnett formula (MG) was very convenient, its applicability was limited [6]. For example, the inclusions must be much smaller than the wavelength of light, the fill factor must be below the so-called percolation threshold (above the percolation threshold, the distinction between inclusion and matrix material becomes meaningless), and the inclusions must be non-interacting. Furthermore, the inclusion material and matrix material must be clearly defined. The MG formula is not symmetric to a reversal of the matrix and inclusion material.

Several attempts have been made to design an effective medium approximation without such limitations. To solve the symmetry problem, a new formula was proposed by Bruggeman which treats all components of an optical nanostructure as inclusions in the effective medium [103]. In the Bruggeman formula (BG), the inclusions were still treated as spherical point dipoles. It was assumed that the medium did not produce any electric field of its own, and the total contribution of the inclusions to the incident electric field must be zero. For example, let us consider the optical nanostructure defined above. In the case

of the BG formula, the inclusion material and the matrix material would both be treated as inclusions. Their dipole polarizabilities can be calculated as:

$$\alpha_{inc} = 4\pi R^3 \frac{\epsilon_{inc} - \epsilon_{eff}}{\epsilon_{inc} + 2\epsilon_{eff}} \; ; \; \alpha_{\mathrm{mat}} = \; 4\pi R^3 \frac{\epsilon_{mat} - \epsilon_{eff}}{\epsilon_{mat} + 2\epsilon_{eff}};$$

where α_{inc} is the effective polarizability of the inclusion and α_{mat} is the effective polarizability of the matrix. Then, the effective permittivity can be calculated form the implicit formula:

$$f\left(\frac{\epsilon_{inc} - \epsilon_{eff}}{\epsilon_{inc} + 2\epsilon_{eff}}\right) + (1-f)\left(\frac{\epsilon_{mat} - \epsilon_{eff}}{\epsilon_{mat} + 2\epsilon_{eff}}\right) = 0$$

Where f is the inclusion fill factor. Although this approximation is symmetric, it still cannot account for finite sized interacting inclusions. Furthermore, the approximation requires solving the above equation iteratively to calculate the effective permittivity.

Volume averaging theory(VAT), applied to Maxwell's equations, was also used to define the effective medium approximation [77]. However, volume averaging also cannot account for the size and shape of the inclusions. Explicit linear effective medium approximations like series and parallel approximations were also proposed [104], which predicted effective optical parameters as series and parallel combinations of the constituent materials. Below, the linear EMA formulas are listed for reference:

Series model:

$$n_{eff} = (1-f)n_{mat} + f n_{inc}$$

Parallel model:

$$\frac{1}{n_{eff}} = \frac{1-f}{n_{mat}} + \frac{f}{n_{inc}}$$

Volume Avg.:

$$n_{eff} = [n_{mat}^2(1-f) + n_{inc}^2 f]^{\frac{1}{2}}$$

Although the formulas above are widely used in the literature, their applicability remains limited. In order to account for the size, shape and interaction of the inclusions, it is vital to extend the existing effective medium theory. Due to its explicit nature, the MG theory is the best candidate for such an extension.

To account for the finite size of the inclusions in a heterogeneous material within the framework of the MG formula, the polarizability of the inclusions must be calculated in a way that accounts for the size of the inclusion. It has been proposed that instead of static polarizability, dynamic polarizability must be used [105]. When the inclusions are spherical, the polarizabilities can be easily calculated using the Mie solutions [106]. In this case, the polarizability can be given as:

$$\alpha = \mathrm{i}\frac{\mathrm{R}^3}{\mathrm{x}^3} a_1 ,$$

where R is the inclusion radius, x is the relative refractive index of the inclusion and a_1 is the Mie coefficient of the first order. Then the effective permittivity can be derived as:

$$\epsilon_{eff} = \frac{x^3 + 3if a_1}{x^3 - \frac{3}{2} if a_1}.$$

The formula above takes the size of the inclusion into account but assumes the size is small enough that it can be represented by a dynamic dipole. However, at a larger size, higher order poles are needed to accurately describe the electrodynamic behavior of the inclusions. Recently, an EMA was proposed which accounted for the third and fifth order dipoles [107]. The number of poles required to mode the inclusions is decided arbitrarily,

which limits the application of Mie extended MG formulas. Also, these formulas cannot account for the interaction between the inclusions. As a result, the formulae derived this way are not accurate enough to justify their extra complexity in use. Thus, there remains a need to design a more general, explicit and accurate EMA.

a) Applicability of EMA

Effective medium approximations are limited in their validity. The Maxwell-Garnett formula is rigorous only when the size of the inclusions is vanishingly small. However, the exact size for which the MG and associated EMA are valid has not been rigorously determined. Some studies have reported that EMAs are accurate when the operating wavelength is more than 6 times larger than the inclusions [108]. However, it is generally accepted that EMAs can become increasingly inaccurate when feature size approaches the wavelength [6].

Another important parameter is the volume density of the medium. This parameter can be represented by the “filling factor”, which is the ratio of the volume of the inclusions to the volume of the substrate. Although a limit on the filling factor is not introduced in the derivation of the EMAs discussed above, it has been found that the filling factor must remain below the percolation threshold of the medium [109]. Above the percolation threshold, the role of inclusion and substrate is switched, and the nanostructure behavior changes in ways that can’t be predicted by the EMA discussed above. Thus, the percolation threshold is an upper limit of the filling factor. In addition, it has been found that EMAs are valid only when the mean separation between the inclusion is at or below the effective wavenumber [108]. This puts a lower limit on the filling factor. That is, if the

nanostructure is too dispersed, it may not be possible to describe the medium with an EMA.

EMAs simplify an optical nanostructure for analytical calculations of their properties. Thus, there is some loss of information. For example, the spatial variation of the nanostructure is lost when it is approximated by an effective medium. In practice, the properties of an optical nanostructure, even a perfectly periodic one, may be locally inhomogeneous and dependent on the incident angle. However, EMAs cannot calculate these variations. As such, EMAs may not be applicable in all calculations. In simple transmission and reflection calculation, Prediction using EMA is considered accurate enough [8]. On the other hand, calculating absorption or heat transfer using EMAs is inaccurate[6, 110]. Furthermore, EMAs generally lose information on size, shape and local variation of the inclusions. In applications where these are relevant, EMAs cannot be applied[110]. Similarly, when there are periodic effects like diffraction and Bloch resonances, EMAs are insufficient to describe the propagation of light [111].

Based on the discussion above, the criteria for applying EMA can be summarized as follows:

- The inclusions need to be small
- The filling factor must be below the percolation threshold
- The filling factor cannot be vanishingly small
- There cannot be any diffraction or Bloch resonances
- The shape and spatial distribution of inclusion cannot be relevant.

C. Problem Statement

In the literature review, we discussed the state-of-the-art research on optical nanostructures and analytical methods to analyze them. Based on the discussion, some over-arching gaps appear in the current technology.

First, optical nanostructures based on low refractive index material, e.g., glass or polymers, have not been explored in detail. Although optical nanostructures using high index materials have been studied in detail, it is not established that high refractive index is a design requirement in optical nanostructures. In fact, the overall role of the refractive index in designing optical nanostructures is unclear. One of the roadblocks in nanophotonics is the lossy and non-transparent nature of typically used materials. On the other hand, low index materials are naturally transparent and loss-less at visible wavelengths. Thus, it is important to consider whether low index materials can be used in designing optical nanostructures.

Second, the available analytical effective medium approximations are very limited. While some of the limitations are unavoidable, it is important to consider whether EMA can be extended to be more general. There is also some ambiguity on the applicability of EMA. For example, while it is known that inclusions need to be small, a rigorous treatment of the size dependence of EMA is needed. The role of shape and morphology of the inclusions should also be included in the EMA. Most importantly, it is important to consider the usefulness of these limitations from a practical perspective. That is, it should be investigated whether violating any of these limitations results in false predictions compared to experimental or numerical results.

A combination of the above issues is seen in the analysis of flat optical components based on optical nanostructures. Even though optical applications demand high transparency and low loss, available instances of these nanostructured flat optical components utilize highly lossy metals and high-index dielectrics. Further, the design of these components relies on full-wave numerical analysis. Since optical applications require quite large-area components as well as far-field calculations, numerical analyses can be time consuming and inefficient in analyzing these nanostructures. An analytical method that combines an analytical wave propagation solution, such as the scalar diffraction theory, with an analytical modelling method, such as effective medium approximation, may be a fast and accurate alternative. An investigation of such an analytical method, including comparison to numerical and experimental results, needs to be executed.

D. Major Contribution

In this work, the identified gaps will be addressed in detail. First, we will investigate low index materials and their applications. We consider both periodic and aperiodic optical nanostructures, consisting of glass and polymers, with a refractive index of $n < 2.0$.

We will address the possibility of creating a complete optical bandgap in planar photonic crystals using low index materials. Specifically, the Schott glass ($n = 1.9$) and the polymers PVK ($n = 1.6$) and PMMA ($n = 1.5$) are considered. The band structures of different lattices of planar photonic crystals will be studied, and the optimal structure for obtaining the bandgap with low index materials will be identified. As an application of the bandgap, the planar photonic crystal cavity will be discussed. The resonant properties of

the cavity will be calculated using full vector wave simulations. Finally, the suitability of the designed cavity as a sensor will be discussed.

We also address the narrow applicability of EMA and derive a generalized EMA by extending the MG formula using the Mie theory. The ambiguity in modelling inclusions of different sizes will be addressed. Furthermore, effective polarizability will be modified to account for the interaction between the nearby inclusions. We will derive a framework where the size and shape of the inclusion can be considered. We will also simplify a derived formula for the Rayleigh regime. We will test out the framework by comparing it with experimental results. We will apply the framework to model both periodic and aperiodic optical nanostructure. Specifically, we will demonstrate modelling an anti-reflection coating and a tunable magnetic colloid and show that the derived framework is more accurate.

Finally, we will address the efficient design and analysis of flat optical elements consisting of aperiodic optical nanostructure on low index material. We will utilize the derived EMA framework along with the scalar diffraction theory as an analytical method, along with the full wave three-dimensional finite difference time domain method (3D-FDTD). First, we will investigate whether the EMA can be used, and then we will test the limit of applicability of the EMA in this context. The designed analytical method will be compared to 3D-FDTD and experimental results. Then, using the designed analytical method, a large-area optical element will be designed and analyzed.

All the results presented in this work are original work. For comparison and demonstration, results from the literature are displayed where necessary and they are

cited appropriately. Based on the work in this research, several original articles have been written. E.g.:

1. Siraji, Ashfaqul Anwar, and Yang Zhao. "High-sensitivity and high-Q-factor glass photonic crystal cavity and its applications as sensors." *Optics letters* 40.7 (2015): 1508-1511.
2. Siraji, Ashfaqul Anwar, and Yang Zhao. "Simple effective medium approximation with Rayleigh scattering." *Optics Letters* 42.9 (2017): 1860-1863.
3. Siraji, Ashfaqul Anwar, and Yang Zhao. “Tunable optical transmission of magnetic microsphere colloids”, Applied Optics 57.36 (2018), 10412-10417.
4. Siraji, Ashfaqul Anwar, and Yang Zhao. “Design and analysis of thin optical lens composed of low index subwavelength structures”, Applied Optics 58.17 (2019), 4654-4664.

E. Organization

The dissertation is organized as follows. In chapter 2, two of the most accurate and commonly used numerical methods for analyzing optical nanostructure are discussed. Their strengths and shortcomings are pointed out, and finally, they are used for analyzing low index planar photonic crystals. The condition for bandgaps in low index materials is discussed. As an application, a planar photonic crystal cavity is designed and analyzed using numerical methods, and its application as a sensor is discussed.

In chapter 3, a more generalized and accurate EMA is derived. It is tested for both periodic and aperiodic optical nanostructures, and the accuracy and limitation of the EMA is discussed. Using this EMA framework, an aperiodic optical nanostructure is designed to work as an optical element in chapter 4. The analytical method is compared to the

numerical method, and its efficiency is tested. Finally, in chapter 5, the findings of the work are summarized.

II. FULL-WAVE NUMERICAL ANALYSIS OF LOW-INDEX OPTICAL NANOSTRUCTURES

The objective of this work is to design controllable and tunable optical nanostructures with low loss in the visible frequencies. Designing optical nanostructures requires careful analysis and processing to establish relationships between their physical parameters and optical properties. Optical nanostructures involve a very wide range of material properties, a wide dynamic range of feature size, as well as many different physical and structural parameters. It is impractical to rely on experimental trial and error to design an optical nanostructure with a specific property. Numerical analysis has emerged as a quick and reliable tool to analyze optical nanostructures and optimize design with a specific goal[112].

Typically, optical nanostructures are a medium where subwavelength physical, chemical, or structural variation control the interaction with an electromagnetic wave. In this work, it is assumed that optical nanostructures interact with visible wavelengths, ranging from 400-800 nm, and have a feature size that is smaller than this range. Although typically such nanostructures are made using dielectrics of varying strength, metallic structures are also frequently used. The goal of the numerical analysis of optical nanostructures is to calculate a specific performance metric from the physical, chemical and structural description of the device. Generally, this goal is achieved in two steps. First, Maxwell's equations are solved for the relevant volume or area of the nanostructure. Then, once the electromagnetic fields are known, the performance metrics are calculated using various post-processing steps[113].

A wide variety of techniques are available to solve Maxwell's equations numerically. The finite difference time domain (FDTD) method and plane wave expansion (PWE) method are two of the most versatile and mature methods. In this chapter, these two methods are briefly discussed. Then their application in numerical analysis of optical nanostructures is demonstrated. Specifically, the relationships between the structural parameter of optical nanostructures and their optical properties are established.

A. Finite Different Time Domain Method

FDTD is a versatile method for analyzing optical nanostructures and has been used to simulate a variety of optical nanostructures [4, 114, 115]. In this method, Maxwell's equations are solved by replacing the differential equations with a center difference equation. Maxwell's equations can be given as:

$$\nabla \times \vec{E}(t) = -\frac{\partial \vec{B}(t)}{\partial t}$$

$$\nabla \times \vec{H}(t) = \vec{J} + \frac{\partial \vec{D}(t)}{\partial t} \tag{2.1}$$

$$\nabla \cdot \vec{B} = 0$$

$$\nabla \cdot \vec{D} = \rho_v$$

Where E is the electric field, D is the displacement, H is the magnetic field, B is the magnetic induction, and ρ_v is the volume charge density. Here, the fields are vectors with x, y, and z components. The curl equations each represent three coupled differential equations. In order to solve all these equations, simply replacing the differential equations with difference equations is not enough. In the FDTD method, an algorithm for calculating the fields is developed from Maxwell's equations.

1. FORMULATION

Although Maxwell's equations all describe the same moment in time, it is helpful to look at the field propagation through Maxwell's equations as a multistep process, as shown in Figure 22. One can calculate the E field from the H field and vice versa. As a first step to solving Maxwell's equations numerically, the time differentials can be replaced by central differences.

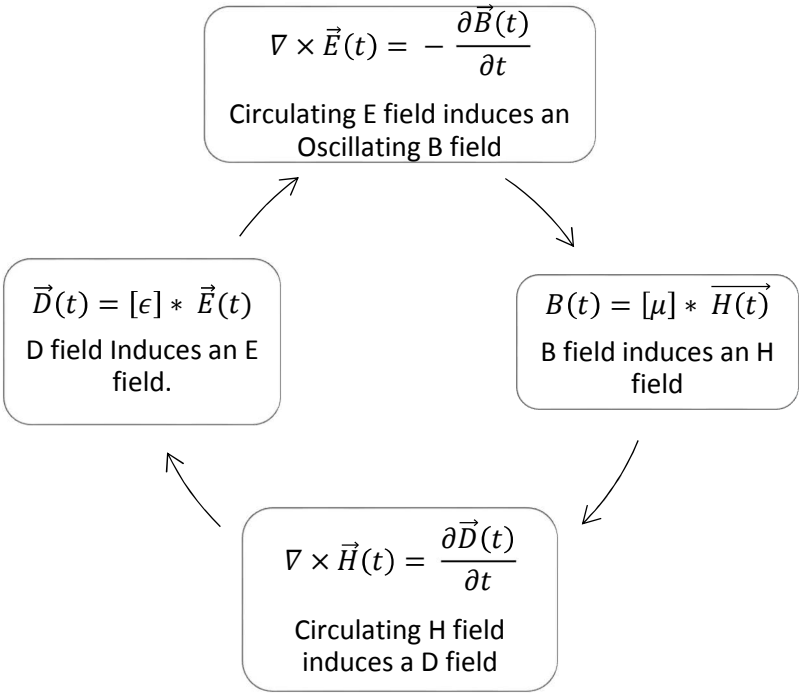

Figure 22 The multistep process of field propagation in FDTD.

For an isotropic, linear and non-dispersive medium, the curl equations can be approximated as:

$$\nabla \times \vec{E}(t) = -\mu \frac{\partial \vec{H}(t)}{\partial t} \implies \nabla \times \vec{E}(t) = -\mu \frac{\vec{H}(t)_{t+\frac{\Delta t}{2}} - \vec{H}(t)_{t-\frac{\Delta t}{2}}}{\Delta t} \tag{2.2}$$

$$\nabla \times \vec{H}(t) = \epsilon \frac{\partial \vec{E}(t)}{\partial t} \implies \nabla \times \vec{H}(t) = \epsilon \frac{\vec{E}(t)_{t+\Delta t} - \vec{E}(t)_t}{\Delta t}$$

These equations can be rewritten as:

$$\vec{H}(t)_{t+\frac{\Delta t}{2}} = \vec{H}(t)_{t-\frac{\Delta t}{2}} - \frac{\Delta t}{\mu}\left(\nabla \times \vec{E}(t)\right) \tag{2.3}$$

$$\vec{E}(t)_{t+\Delta t} = \vec{E}(t)_t + \frac{\Delta t}{\epsilon}(\nabla \times \vec{H}(t))$$

From these equations, any of the fields at an instance *t* can be calculated if one field is known at a previous time and the other field is known at an intermediate time. Thus, the evolution of the electromagnetic fields has been discretized in the time domain, with a time step Δt. The E fields are known at instances $n\Delta t$, and the H fields are known at instances $(2n+1)\Delta t/2$, as shown in Figure 23.

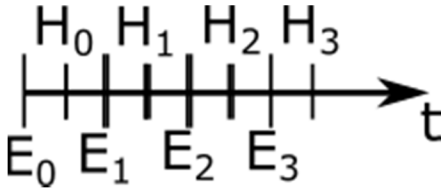

Figure 23 The relative positions of successive calculated E and H entities in the time axis

Thus, by discretizing the time axis and then placing the calculated instances of E and H entities in a staggered position, the time differential equations can be replaced by difference equations.

However, the cross equations remain, which are partial differential equations themselves. These equations can also be replaced by difference equations if the space axes $(\hat{x}, \hat{y}, \hat{z})$ are discretized as well. The discretized and staggered grid scheme for the time and space axes was suggested in [116] and has subsequently been widely used. The staggered grid scheme is shown in Figure 24. Using this discretizing scheme, the cross equations can now be replaced by difference equations. Generally, the electric field E is many times stronger than the magnetic field. This may cause numerical instability in the difference equation. To avoid this, the magnetic field is normalized by the impedance of the medium:

$$\tilde{\vec{H}} = \sqrt{\frac{\mu}{\epsilon}}\vec{H}.$$

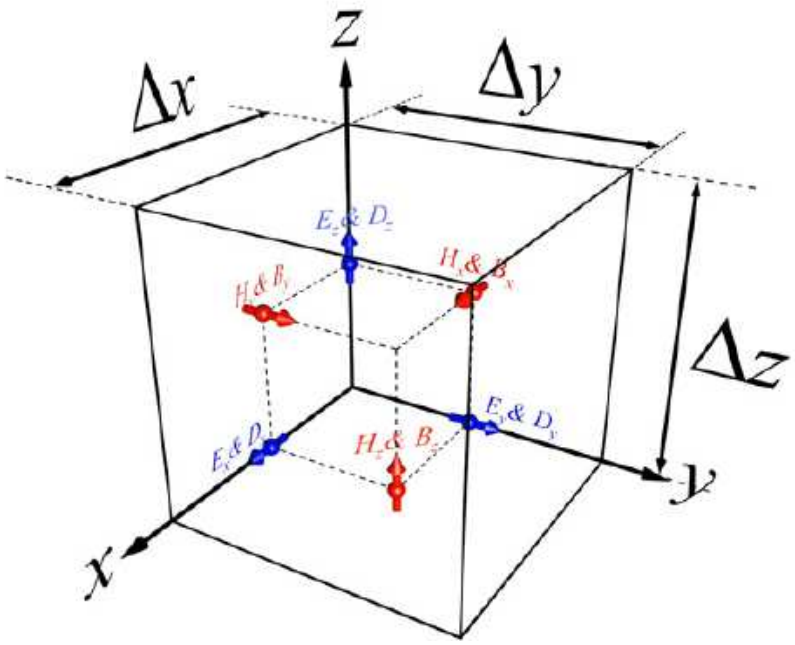

Figure 24 The staggered position of the fields in a discretized spatial grid.

After normalization, the curl equations can be expanded and discretized, as shown in Table 4.

Table 4: The discretized Maxwell's equations

$\nabla \times \vec{E}(t) = -\mu \frac{\partial \vec{H}(t)}{\partial t}$	
$\frac{\partial E_Z}{\partial y} - \frac{\partial E_y}{\partial z} = -\frac{\mu_{xx}}{c_0}\frac{\partial \tilde{H}_x}{\partial t}$	$\frac{E_z^{i,j+1,k}\|_t - E_z^{i,j,k}\|_t}{\Delta y} - \frac{E_y^{i,j,k+1}\|_t - E_y^{i,j,k}\|_t}{\Delta z} = -\frac{\mu_{xx}^{i,j,k}}{c_0}\frac{\tilde{H}_x^{i,j,k}\|_{t+\Delta t/2} - \tilde{H}_x^{i,j,k}\|_{t-\Delta t/2}}{\Delta t}$
$\frac{\partial E_x}{\partial z} - \frac{\partial E_z}{\partial x} = -\frac{\mu_{yy}}{c_0}\frac{\partial \tilde{H}_y}{\partial t}$	$\frac{E_x^{i,j,k+1}\|_t - E_x^{i,j,k}\|_t}{\Delta z} - \frac{E_z^{i+1,j,k}\|_t - E_z^{i,j,k}\|_t}{\Delta x} = -\frac{\mu_{yy}^{i,j,k}}{c_0}\frac{\tilde{H}_y^{i,j,k}\|_{t+\Delta t/2} - \tilde{H}_y^{i,j,k}\|_{t-\Delta t/2}}{\Delta t}$

$\frac{\partial E_y}{\partial x} - \frac{\partial E_x}{\partial y} = -\frac{\mu_{zz}}{c_0}\frac{\partial \widetilde{H}_z}{\partial t}$	$\frac{E_y^{i+1,j,k}\|_t - E_y^{i,j,k}\|_t}{\Delta x} - \frac{E_x^{i,j+1,k}\|_t - E_x^{i,j,k}\|_t}{\Delta y} = -\frac{\mu_{zz}^{i,j,k}}{c_0}\frac{\widetilde{H}_z^{i,j,k}\|_{t+\Delta t/2} - \widetilde{H}_z^{i,j,k}\|_{t-\Delta t/2}}{\Delta t}$
$\nabla \times \vec{H}(t) = \epsilon \frac{\partial \vec{E}(t)}{\partial t}$	
$\frac{\partial \widetilde{H}_z}{\partial y} - \frac{\partial \widetilde{H}_y}{\partial z} = \frac{\epsilon_{xx}}{c_0}\frac{\partial E_x}{\partial t}$	$\frac{\widetilde{H}_z^{i,j+1,k}\|_{t+\Delta t/2} - \widetilde{H}_z^{i,j,k}\|_{t+\Delta t/2}}{\Delta y} - \frac{\widetilde{H}_y^{i,j,k+1}\|_{t+\Delta t/2} - \widetilde{H}_y^{i,j,k}\|_{t+\Delta t/2}}{\Delta z} = \frac{\epsilon_{xx}^{i,j,k}}{c_0}\frac{E_x^{i,j,k}\|_{t+\Delta t} - E_x^{i,j,k}\|_t}{\Delta t}$
$\frac{\partial \widetilde{H}_x}{\partial z} - \frac{\partial \widetilde{H}_z}{\partial x} = \frac{\epsilon_{yy}}{c_0}\frac{\partial E_y}{\partial t}$	$\frac{\widetilde{H}_x^{i,j,k+1}\|_{t+\Delta t/2} - \widetilde{H}_x^{i,j,k}\|_{t+\Delta t/2}}{\Delta z} - \frac{\widetilde{H}_z^{i+1,j,k}\|_{t+\Delta t/2} - \widetilde{H}_z^{i,j,k}\|_{t+\Delta t/2}}{\Delta x} = \frac{\epsilon_{yy}^{i,j,k}}{c_0}\frac{E_y^{i,j,k}\|_{t+\Delta t} - E_y^{i,j,k}\|_t}{\Delta t}$
$\frac{\partial \widetilde{H}_y}{\partial x} - \frac{\partial \widetilde{H}_x}{\partial y} = \frac{\epsilon_{zz}}{c_0}\frac{\partial E_z}{\partial t}$	$\frac{\widetilde{H}_y^{i+1,j,k}\|_{t+\Delta t/2} - \widetilde{H}_y^{i,j,k}\|_{t+\Delta t/2}}{\Delta x} - \frac{\widetilde{H}_x^{i,j+1,k}\|_{t+\Delta t/2} - \widetilde{H}_x^{i,j,k}\|_{t+\Delta t/2}}{\Delta y} = \frac{\epsilon_{zz}^{i,j,k}}{c_0}\frac{E_z^{i,j,k}\|_{t+\Delta t} - E_z^{i,j,k}\|_t}{\Delta t}$

From the linear difference equation, an updated equation for each field component can be derived, using staggered time and space coefficients. Thus, the fundamental formalism of the FDTD method can be summarized as in Figure 25.

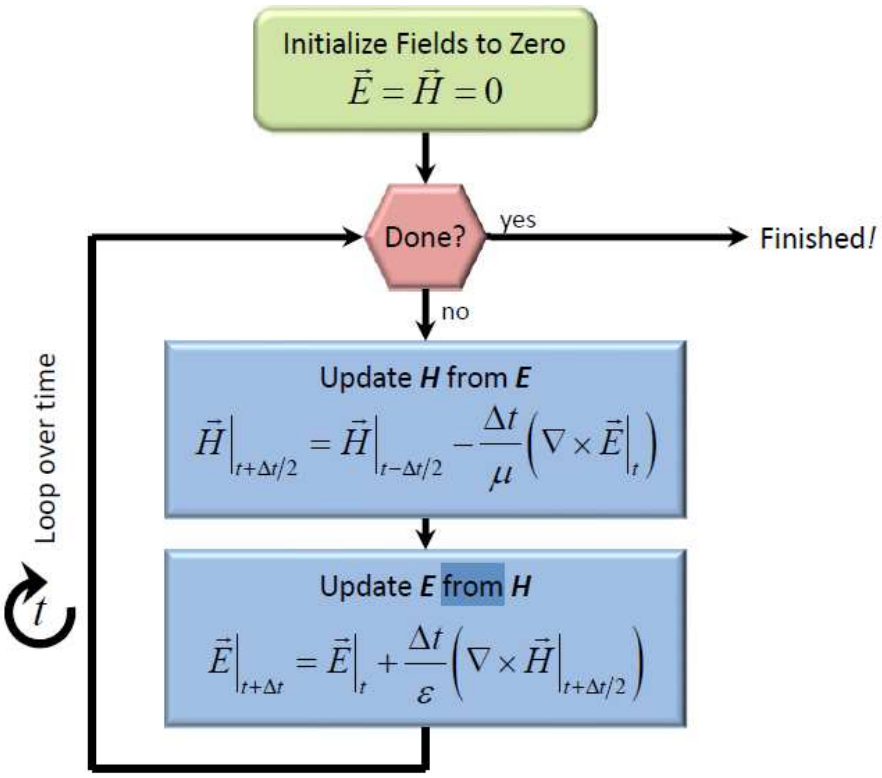

Figure 25 Fundamental Formalism of FDTD.

Using this step by step method, one can simulate the propagation of an electromagnetic field through any medium. However, unless there is a way to add sources, then all the results would be meaningless. To understand how sources are added to an FDTD calculation, let us consider a planar device, represented by the xy plane in Figure 26. The fields in the plane are evaluated at each time step. To add a source, first a time dependent source signal needs to be built. Once the source signal is calculated, it can be added to the field at each time step in the following way:

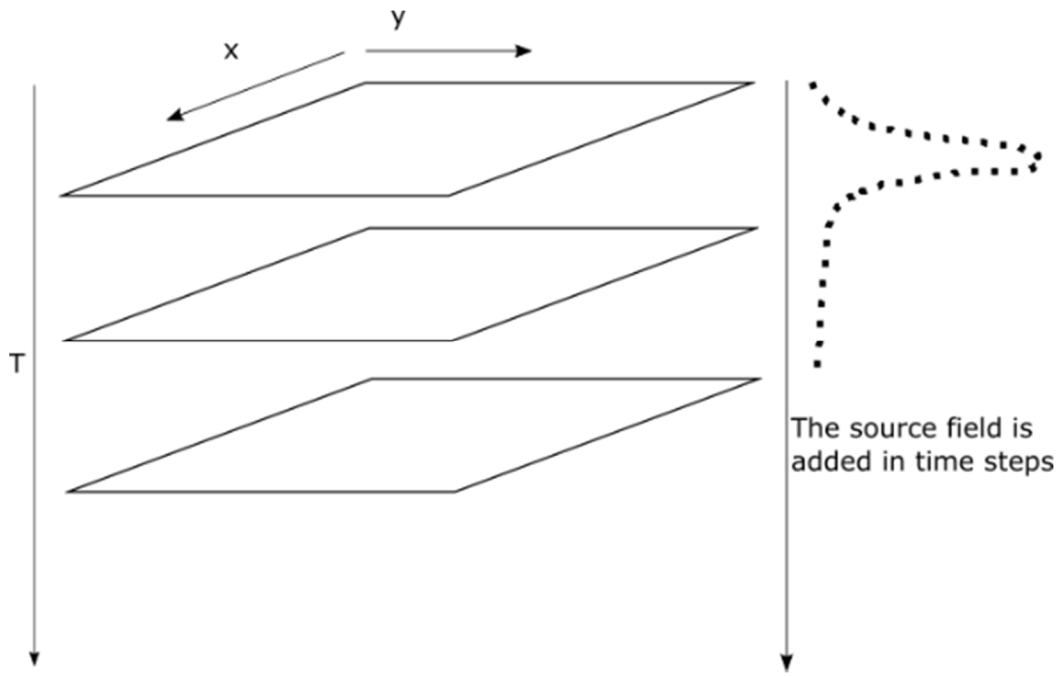

Figure 26 Adding source in to the FDTD algorithm

$$E(r,t) = E(r,t-\Delta t) + S(r,t) \tag{2.4}$$

where E is the field entity and S is the source signal. The source can be an impulse function, a Gaussian function, or a plane-wave, depending on the problem.

Another important consideration is the boundary condition of the problem. From Table 4, to calculate the future value of any entity, only the past values of related field entities are required. However, in a space domain, to calculate the value of any field entity at a grid-point, the vales of related entities at the preceding and succeeding grid-points must also be known. A problem arises at the boundaries, where either the preceding or the succeeding grid-point does not exist, i.e., these values are outside of the grid. There are several approaches to address this issue. For example:

- The Dirichlet boundary condition: In this condition, the unknown entities outside the grids are assumed to be 0.

- The periodic boundary condition: This boundary condition only applies when it is known that the fields are periodic. In this case, the fields are wrapped around with appropriate phase change, as shown in Figure 27.

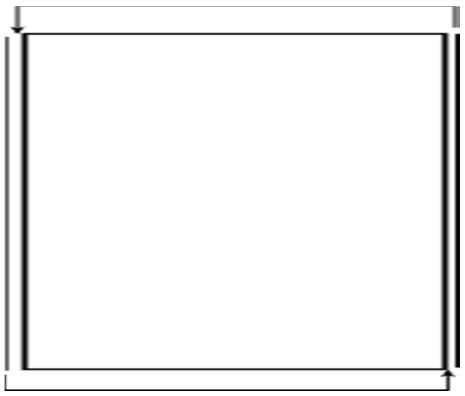

Figure 27 The Periodic boundary condition.

Another vital consideration is the grid resolution. There are several requirements that must be satisfied by the grid resolution.

- The minimum grid resolution (Δ) must be small enough to resolve the minimum wavelength ($10\,\Delta \approx \frac{\lambda_{min}}{n_{max}}$).
- Δ must small be enough to resolve the minimum feature size (d_{min}): $4\Delta \approx d_{min}$.

It is a good idea to start the calculation with the coarsest possible grid and then increase the resolution in steps to see when the result converges.

Like space resolution, time resolution must also be carefully chosen. Very fine time steps may result in calculations that are too long. The upper limit on time resolution (Δt) is given as:

$$\Delta t = \frac{1}{c_0\sqrt{\frac{1}{(\Delta x)^2}+\frac{1}{(\Delta y)^2}+\frac{1}{(\Delta z)^2}}}$$

This limit is known as the Courant stability limit. Steps larger than this result in instability.

2. PERFECTLY MATCHED LAYER

While the discussed methodology is stable and accurate, a common problem with simulating any real device is reflection at the simulation boundary. For example, in the real world, any device can scatter the incident fields into the free space, and the scattered fields may radiate into the infinite free space. However, when performing FDTD calculations, we cannot simulate the infinite space and the simulation grid must have edges. Scattered fields can be reflected at these edges, as shown in Figure 28(a). This is clearly a non-physical representation.

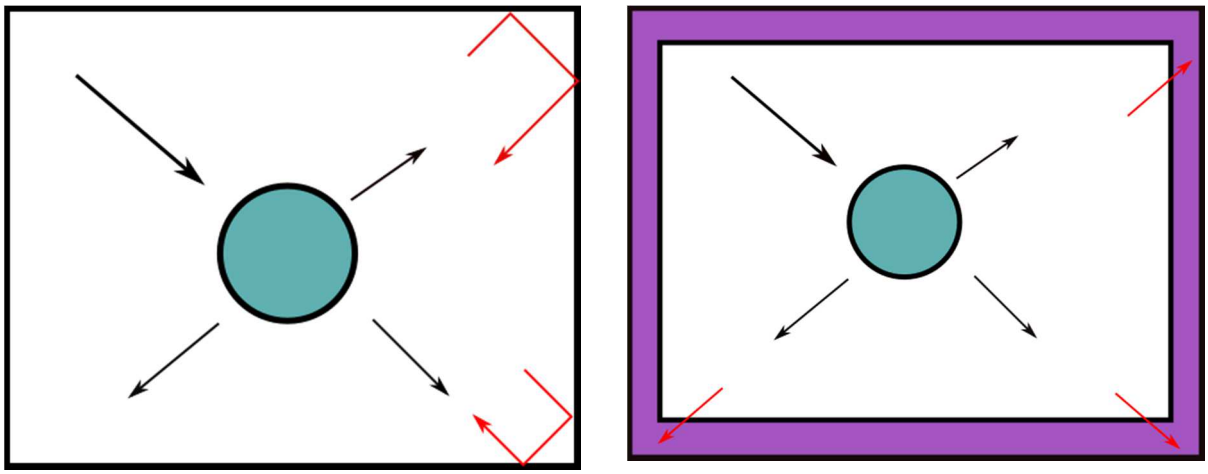

(a) (b)

Figure 28 (a) Reflection at the boundary without PML, (b) Fields at the boundary with PML.

A way around this spurious reflection is to wrap the boundary with a material that absorbs the incoming wave with no reflection, i.e., the impedance at the interface is perfectly matched for all wavelengths, angles, and polarizations. Since this extra layer is non-physical, we can design its parameters to perfectly absorb the incoming waves of all frequencies, angles and polarizations. Such a reflection-less layer, shown in Figure 28(b),

is called a perfectly matched layer (PML). It is now common practice to surround the simulation problem with PML to avoid non-physical reflection at the boundary.

B. Plane Wave Expansion Method

The plane wave expansion method is a relatively quick method of solving Maxwell's equations. This is a specialized method because it applies only to cases where the device and fields are spatially periodic. The spatial periodicity allows them to be resolved into harmonics and reduce Maxwell's equations into an eigen-value problem.

1. FORMULATION

Like the FDTD method, the plane wave expansion method (PWE) also starts with Maxwell's equations. However, the PWE is a Fourier space method. In this method, the real space Maxwell's equations are first converted into the Fourier space Maxwell's equations. For example, the ***x*** component of the magnetic curl equation can be written as:

$$\frac{\partial \widetilde{H}_Z}{\partial y} - \frac{\partial \widetilde{H}_y}{\partial z} = k_0 \epsilon_r E_x \tag{2.5}$$

Assuming the fields and the device are spatially periodic infinitely in all directions, they can be resolved into harmonics. For example, the permittivity function can be expanded into a Fourier Series as:

$$\epsilon_r = \sum_{p=-\infty}^{\infty} \sum_{q=-\infty}^{\infty} \sum_{r=-\infty}^{\infty} a(p,q,r) \mathrm{e}^{j\left(p\vec{T}_1 + q\vec{T}_2 + r\vec{T}_3\right)\cdot\vec{r}} \tag{2.6}$$

where $\vec{T}_1 = \frac{2\pi}{\Lambda_x}\hat{x}, \vec{T}_2 = \frac{2\pi}{\Lambda_y}\hat{y}, \vec{T}_3 = \frac{2\pi}{\Lambda_z}\hat{z}$ are the reciprocal lattice vectors, $\Lambda_x, \Lambda_y, \Lambda_z$ are the period along x, y, and z axis, and p,q,r ae the indices of the harmonics in the reciprocal lattice. The fields can also be expanded as:

$$\vec{E}(r) = e^{-j\vec{\beta}\cdot\vec{r}} \sum_{p=-\infty}^{\infty}\sum_{q=-\infty}^{\infty}\sum_{r=-\infty}^{\infty} \vec{S}(p,q,r)e^{j\left(p\vec{T}_1+q\vec{T}_2+r\vec{T}_3\right)\cdot\vec{r}}$$

$$= \sum_{p=-\infty}^{\infty}\sum_{q=-\infty}^{\infty}\sum_{r=-\infty}^{\infty} \vec{S}(p,q,r)e^{-j\left(k_x x+k_y y+k_z z\right)} \tag{2.7}$$

Where

$$\begin{aligned} k_x &= \beta_x - pT_{1,x} - qT_{2,x} - rT_{3,x} \\ k_y &= \beta_y - pT_{1,y} - qT_{2,y} - rT_{3,y} \\ k_z &= \beta_z - pT_{1,z} - qT_{2,z} - rT_{3,z} \end{aligned} \tag{2.8}$$

Similarly, the magnetic fields can be expanded as:

$$\vec{H}(r) = \sum_{p=-\infty}^{\infty}\sum_{q=-\infty}^{\infty}\sum_{r=-\infty}^{\infty} \vec{U}(p,q,r)e^{-j\left(k_x x+k_y y+k_z z\right)} \tag{2.9}$$

Then, Maxwell's equations can be transformed into linear equations in the Fourier space:

Table 5 Maxwell's equations in the Fourier Space

Real Space	Fourier Space
$\frac{\partial \widetilde{H}_z}{\partial y} - \frac{\partial \widetilde{H}_y}{\partial z} = k_0\epsilon_r E_x$	$k_y(q)U_z(p,q,r) - k_z(r)U_y(p,q,r) = jk_0 a(p,q,r) \star S_x(p,q,r)$
$\frac{\partial \widetilde{H}_x}{\partial z} - \frac{\partial \widetilde{H}_z}{\partial x} = k_0\epsilon_r E_y$	$k_z(r)U_x(p,q,r) - k_x(p)U_z(p,q,r) = jk_0 a(p,q,r) \star S_y(p,q,r)$
$\frac{\partial \widetilde{H}_y}{\partial x} - \frac{\partial \widetilde{H}_x}{\partial y} = k_0\epsilon_r E_y$	$k_x(q)U_y(p,q,r) - k_y(r)U_x(p,q,r) = jk_0 a(p,q,r) \star S_z(p,q,r)$
$\frac{\partial E_z}{\partial y} - \frac{\partial E_y}{\partial z} = k_0\mu_r \widetilde{H}_x$	$k_y(q)S_z(p,q,r) - k_z(r)S_y(p,q,r) = jk_0 b(p,q,r) \star U_x(p,q,r)$
$\frac{\partial E_x}{\partial z} - \frac{\partial E_z}{\partial x} = k_0\mu_r \widetilde{H}_y$	$k_z(r)S_x(p,q,r) - k_x(p)S_y(p,q,r) = jk_0 b(p,q,r) \star U_y(p,q,r)$
$\frac{\partial E_y}{\partial x} - \frac{\partial E_x}{\partial y} = k_0\mu_r \widetilde{H}_z$	$k_x(p)S_y(p,q,r) - k_y(q)S_x(p,q,r) = jk_0 b(p,q,r) \star U_z(p,q,r)$

The Fourier Space equation can be written in a matrix form as:

$$\mathbf{K}_\mathrm{y}\mathbf{u}_\mathrm{z} - \mathbf{K}_\mathrm{z}\mathbf{u}_\mathrm{y} = jk_0[\![\epsilon_r]\!]\mathbf{s}_\mathrm{x}$$

$$\begin{aligned}
\mathbf{K}_z\mathbf{u}_x - \ \mathbf{K}_x\mathbf{u}_z &= jk_0[\![\epsilon_r]\!]\mathbf{s}_y \\
\mathbf{K}_x\mathbf{u}_y - \ \mathbf{K}_y\mathbf{u}_x &= jk_0[\![\epsilon_r]\!]\mathbf{s}_z \\
\mathbf{K}_y\mathbf{s}_z - \ \mathbf{K}_z\mathbf{s}_y &= jk_0[\![\mu_r]\!]\mathbf{u}_x \\
\mathbf{K}_z\mathbf{s}_x - \ \mathbf{K}_x\mathbf{s}_z &= jk_0[\![\mu_r]\!]\mathbf{u}_y \\
\mathbf{K}_x\mathbf{s}_y - \ \mathbf{K}_y\mathbf{s}_x &= jk_0[\![\mu_r]\!]\mathbf{u}_z
\end{aligned} \tag{2.10}$$

These equations can be summarized in a block matrix form:

$$\begin{bmatrix} \mathbf{0} & -\mathbf{K_z} & \mathbf{K_y} \\ \mathbf{K_z} & \mathbf{0} & -\mathbf{K_x} \\ -\mathbf{K_y} & \mathbf{K_x} & \mathbf{0} \end{bmatrix} \begin{bmatrix} \mathbf{u_x} \\ \mathbf{u_y} \\ \mathbf{u_z} \end{bmatrix} = jk_0 \begin{bmatrix} [\![\epsilon_r]\!] & 0 & 0 \\ 0 & [\![\epsilon_r]\!] & 0 \\ 0 & 0 & [\![\epsilon_r]\!] \end{bmatrix} \begin{bmatrix} \mathbf{s_x} \\ \mathbf{s_y} \\ \mathbf{s_z} \end{bmatrix} \Longrightarrow \left[\vec{\mathbf{K}} \times\right]\vec{\mathbf{u}} = jk_0[[\![\epsilon_r]\!]]\vec{\mathbf{s}} \tag{2.11}$$

$$\begin{bmatrix} \mathbf{0} & -\mathbf{K_z} & \mathbf{K_y} \\ \mathbf{K_z} & \mathbf{0} & -\mathbf{K_x} \\ -\mathbf{K_y} & \mathbf{K_x} & \mathbf{0} \end{bmatrix} \begin{bmatrix} \mathbf{s_x} \\ \mathbf{s_y} \\ \mathbf{s_z} \end{bmatrix} = jk_0 \begin{bmatrix} [\![\mu_r]\!] & 0 & 0 \\ 0 & [\![\mu_r]\!] & 0 \\ 0 & 0 & [\![\mu_r]\!] \end{bmatrix} \begin{bmatrix} \mathbf{u_x} \\ \mathbf{u_y} \\ \mathbf{u_z} \end{bmatrix} \Longrightarrow \left[\vec{\boldsymbol{K}} \times\right]\vec{\mathbf{s}} = \boldsymbol{jk_0}[[\![\mu_r]\!]]\vec{\mathbf{u}} \tag{2.12}$$

From these equations, either the magnetic field or the electric field can be eliminated to form a single double-cross equation. In terms of the electric field, the equation becomes

$$\left[\vec{\mathbf{K}} \times\right][[\![\mu_r]\!]]^{-1}\left[\vec{\mathbf{K}} \times\right]\vec{\mathbf{s}} = -k_0^2\,[[\![\epsilon_r]\!]]\vec{\mathbf{s}} \tag{2.13}$$

And in terms of the magnetic field:

$$\left[\vec{\mathbf{K}} \times\right][[\![\epsilon_r]\!]]^{-1}\left[\vec{\mathbf{K}} \times\right]\vec{\mathbf{u}} = -k_0^2\,[[\![\mu_r]\!]]\vec{\mathbf{u}} \tag{2.14}$$

These equations are general eigen value equations, where k_0 is the eigen value. It is the frequency of light scaled by its speed. Thus, by solving the above eigenvalue equation, it is possible to ascertain which frequencies can be permissible in each problem and obtain the electric and magnetic fields associated with those frequencies.

It is illuminating to note that the frequency and fields of a mode are the output of the above equation. The input in this formalism is β, called the Bloch wave vector, which indicates the direction of the wave. Thus, by using the above formalism, it is possible to

determine the permissible frequencies and associated fields of modes after exciting the problem domain with a specific Bloch wave vector. Generally, the possible values of β are infinite. However, due to the assumed spatial periodicity of the problem domain, spanning the wavevectors in the irreducible brillouin zone (IBZ) is sufficient[117]. Thus, a plot of ω versus β over the IBZ completely characterizes the problem volume. This plot is generally called the frequency band versus wave vector diagram, or simply the band diagram. The primary output of PWE based routines is typically this band diagram over an appropriate IBZ.

It must also be noted that in theory, an infinite number of harmonics (p, q, r) is needed to completely synthesize the electric and magnetic fields. However, in practice, the number of harmonics is finite and decided by a convergence study.

C. Application

In the subsequent sections, we apply the FDTD and PWE methods to simulate several photonic devices. We first address the scattering of electromagnetic fields by a single spherical scatterer. An analytical solution for this problem is found, and numerical analysis by FDTD is compared with analytical results. Then, a purely periodic structure is characterized by calculating its band diagram. After that, the modes of non-periodic structure are studied. For these calculations, various commonly available FDTD and PWE tools are used, along-side developed packages. For example, Lumerical FDTD, Rsoft fullwave and bandsolve, as well as CST Microwave studio is used for the simulations, while MATLAB is used extensively both for development and post-processing.

1. SINGLE SCATTERER

In this section, the directional scattering of a single spherical scatterer is calculated. That is, the ratio of the forward scattering and backward scattering of the spherical scatterer is calculated. Our goal is to compare the FDTD results with the analytical results calculated from the Mie theory. Using simulation, we show that hollow particles can be tuned to have enhanced directional scattering.

We consider a hollow particle composed of a low-index dielectric ceramic, e.g., SiCN or low index polymers. In subsequent calculations, the radius of the particle is set at 31.8 □m, while the thickness of the particle shell is set at 50 nm. Similar structures have been reported in the literature [118, 119]. A schematic diagram of the shell and the FDTD study is shown in Figure 29.

To calculate the F/B ratio analytically, the forward and backward scattering efficiencies of the hollow particle have been calculated using the Mie theory. The formula for forward scattering and backward scattering can be given as [120]:

$$FS = \frac{1}{x^2}\sum_{n}\frac{1}{2n+1}|a_n + b_n|^2 \tag{2.15}$$

$$BS = \frac{1}{x^2}\sum_{n}\frac{1}{2n+1}|a_n - b_n|^2 \tag{2.16}$$

where FS denotes the forward scattering efficiency, BS denotes the backward scattering efficiency, x (= 2πR/λ) is the size parameter, R is the radius of the particle, n is the order, a_n is the coefficient for scattered electric field and b_n is the coefficient for the scattered magnetic field. The coefficients a_n and b_n can be analytically calculated for a hollow spherical shell [121].

The forward and backward scattering efficiency has also been calculated using the 3-dimensional finite difference time domain (FDTD) method, in which a total-field/scattered field (TFSF) source has been used to excite the hollow particle. By monitoring the normalized power of the scattered field in front of the shell, the forward scattering efficiency can be calculated. Backward scattering efficiency can be calculated by monitoring the normalized power at the back of the particle.

The directivity of the particle is defined as:

$$D = \frac{4\pi}{P_{rad}} Max[p(\theta, \phi)] \tag{2.17}$$

where D is the directivity, P_{rad} is the total radiated power, and $p(\theta, \phi)$ is the power at a direction. The directivity has been calculated by calculating the far-field from the near-field.

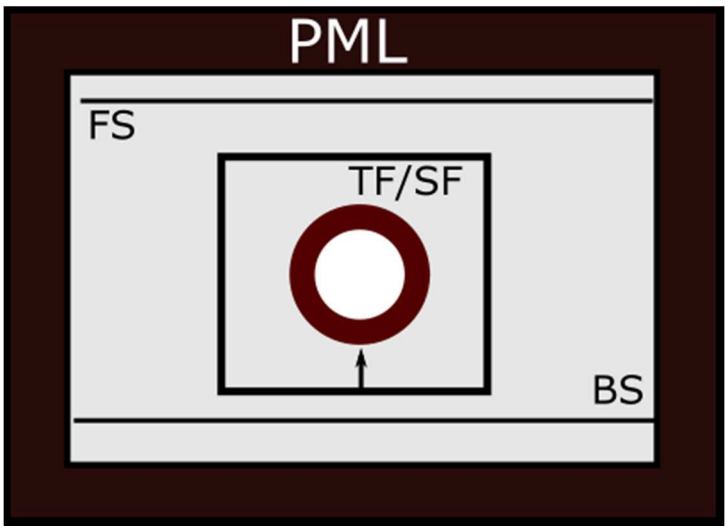

Figure 29 The schematic of the FDTD study, showing PML boundary, TFSF source, and the two field monitors to calculate the forward scattering (FS) and backward scattering (BS).

The F/B ratio has been calculated for the hollow particle as well as a solid particle which is composed of the same material as the shell and has the same radius. A summary of the Mie calculation and FDTD calculations is shown in Figure 30.

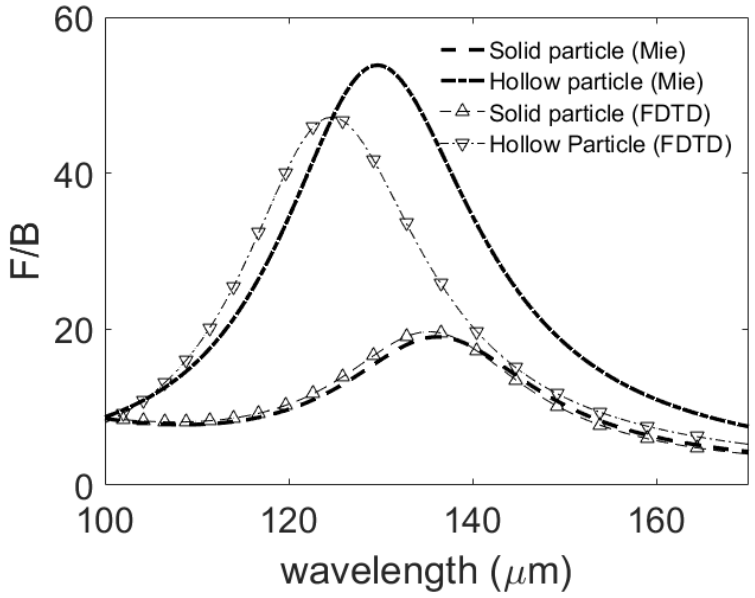

Figure 30 The F/B ratio of a solid particle and hollow shell

Clearly, the analytical results obtained using the Mie theory agree reasonably well with the FDTD results. The hollow particle has a significantly higher F/B ratio. The enhanced directionality of the scattering can be attributed to the Kerker condition. Unlike the solid particle, the electric and magnetic modes of the hollow particle nearly cancel each other out in the backward direction, resulting in the enhanced F/B ratio.

The reflectivity of the particle is shown in Figure 31. Around 120~130 □m, the reflectivity nearly falls to zero, implying that at these wavelengths, the incident waves are almost completely transmitted. This observation agrees with the F/B ratio seen in Figure 30. At 120~130 □m wavelengths, the forward scattering efficiency is many times that of the backward efficiency, implying reduced reflection.

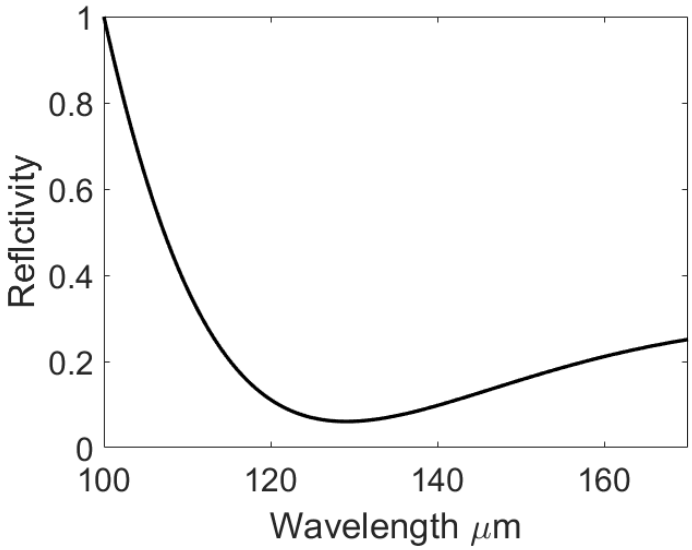

Figure 31 The reflectivity of the particle.

The directivity measures how much of the radiated power is directed at a certain direction. The calculated directivity of the hollow particle is shown in Figure 32. Near 120~130 □m, the directivity is quite high at 15 dBi. At higher wavelengths, the directivity slowly falls to 12 dBi.

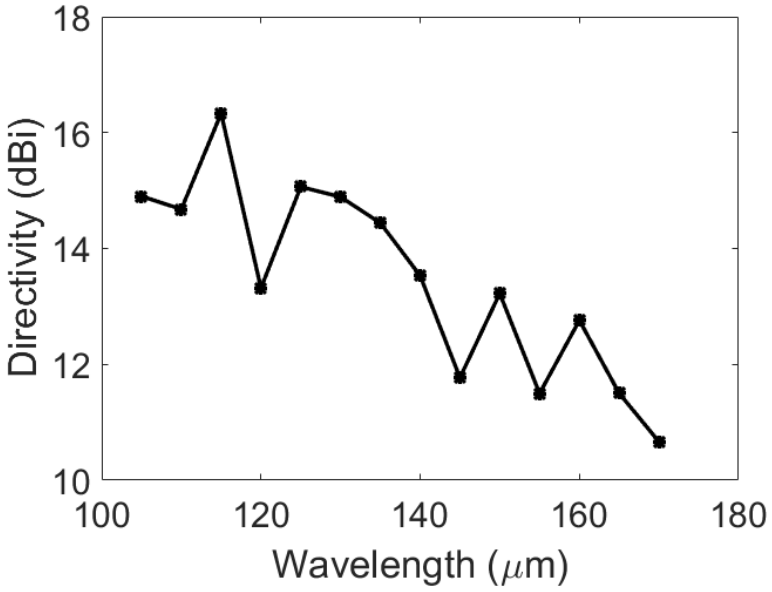

Figure 32The directivity of the hollow particle.

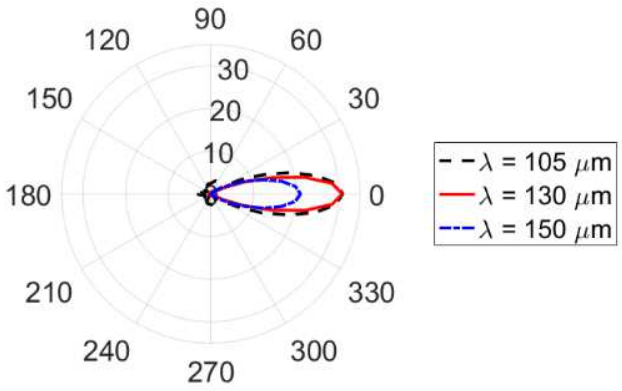

Figure 33 The radiation pattern of the hollow particle (linear scale).

As shown in Figure 33, at a higher wavelength, the radiation pattern shows side lobes which reduce the power available at the main lobe, leading to smaller directivity.

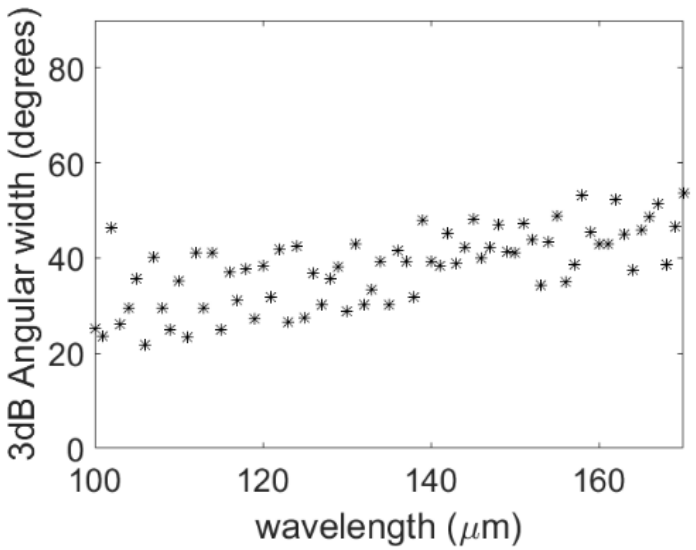

Figure 34 The half power beam width of the hollow particle

The half power beam width of the hollow particle is shown in Figure 34. Although the F/B ratio has a peak at 130 □m, the directivity falls at a higher wavelength, which results in a

larger beam width. The beam width increases slowly from 20^0 to 50^0 at longer wavelengths.

In Table 6 and Table 7 , the F/B ratio and the directivity of the hollow particle are compared with similar work in the literature. The hollow particle compares favorably to existing results.

Table 6 Comparison of F/B ratio with literature.

F/B	Ref
10	[122]
10	[123]
12	[124]
50	This work

Table 7 Comparison of directivity with literature.

Directivity	Ref
6.17	[125]
2	[126]
6.3	[127]
10	[128]
25	[129]
30	This work

The relevant quantities here are directivity and F/B ratio, which were calculated using FDTD method. Each simulation took 5 minutes on average, requiring <1GB of memory.

2. PERIODIC STRUCTURES

Periodic structures, such as photonic crystals and metamaterials, are vitally important for many nanophotonic applications. It is possible to calculate the permissible modes in a periodic structure. The frequencies and spatial profile of the modes can be calculated using PWE. In Figure 35 (a), the unit cell of a periodic photonic crystal, consisting of air holes of radius (*R*) in a lattice of period (*a*) on a dielectric substrate, is shown.

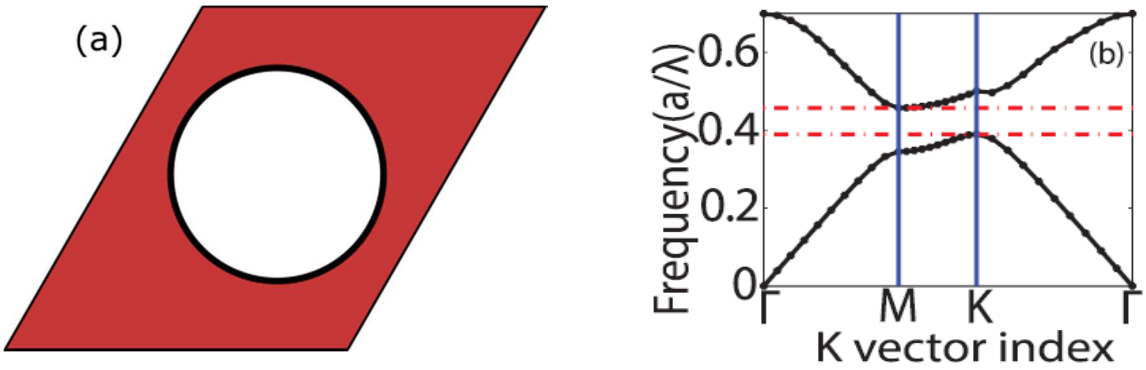

Figure 35 (a) the unit cell of a purely periodic medium consisting of airholes in a dielectric substrate and(b) the calculated band structure of the periodic medium.

To implement nanophotonic devices, the presence of an optical bandgap is often desirable. An optical bandgap refers to a band of frequencies where no permissible mode exists, and such a forbidden frequency band can be harnessed for many useful applications. A sample band diagram, calculated by setting *R* = *0.4a*, is shown in Figure 35(b). When the refractive index of the core material is around the airholes (n_{core}) = 1.9, a bandgap exists between $\frac{a}{\lambda} = 0.39 \sim 0.45$. The position and width of the bandgap are dependent on the lattice structure of the periodicity, as well as the index contrast between the dielectric core and the circular scatterers.

In Figure 36(a), the position of the bandgap is shown between the air-band edge and the dielectric-band edge. For a higher refractive index, the bandgap occurs at lower frequencies and the bandgap width increases. In Figure 36(b), the bandgap width is plotted against n_{core}. We observe that there is a minimum refractive index below which the bandgap doesn't exist. On the other hand, above this threshold, the bandgap width increases linearly. The linear increase can be modeled by

$$BW = 0.12\, n_{core} - 0.155 \tag{2.18}$$

Where BW is the bandgap width. Based on this bandgap study, it can be concluded that planar photonic crystal cavities can be designed on a low index material if n_{core} >1.5.

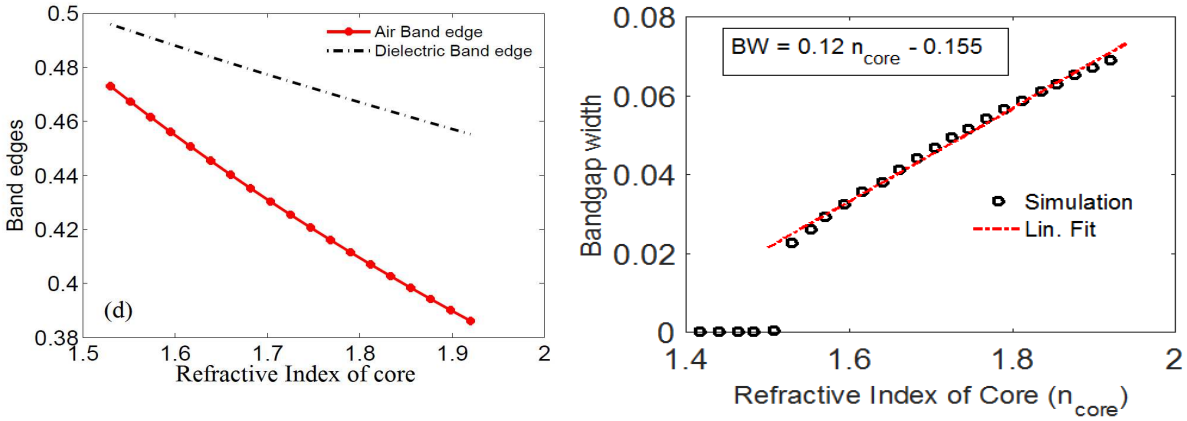

(a) (b)

Figure 36(a)The position of the bandgap for different refractive index of the core. (b) The bandgap width plotted against increasing n_{core}.

Here, each bandgap was determined by calculating the band diagram of the relevant periodic media. Each diagram required around 2 minutes to calculate, requiring >10MB of memory.

3. PERTURBED PERIODIC STRUCTURE

In the previous section, the band structure calculations are described, characterizing the behavior of all the modes in a photonic crystal. However, the behavior of the resonant mode of the cavity, which is typically formed by a perturbation in the photonic crystal lattice, cannot easily calculated using the above-mentioned procedure. The primary reason behind this is the fact that when there is a cavity in a photonic crystal, the periodicity of the structure is perturbed. As such, neither the Bloch theorem nor the periodic boundary condition apply. As such, the Maxwell equation must be solved directly using FDTD to predict the resonant behavior of a photonic crystal cavity.

To solve Maxwell's equations, the simulation domain was covered with a rectangular mesh with 5nm step size in all three directions. Perfectly matched layers (PML) were used as a boundary, with the appropriate number of layers and reflectivity so that the electromagnetic waves do not backscatter into the simulation domain from the boundary. The minimum time step was chosen to be 0.009 fs. The simulation was run for 1000 fs, approximately 1.1×10^5 time steps. A Gaussian impulse source was added into the cavity at the beginning of the simulation, and the fields could evolve according to the Maxwell equation. At the end of the run, the time dependent field data was collected from several points within the cavity, and their average was taken to eliminate any numerical noise. The time signal was then converted to frequency response using the Fourier transform. From the calculated frequency data, Q factor is calculated from the formula:

$$Q = \frac{\pi f_r}{m} \tag{2.19}$$

where f_r is the resonant frequency, and m is the slope of the decaying time envelope at the resonant frequency. To calculate the Q factor, the envelope of the time data

associated with the resonant peak was separated using a Gaussian Filter, and the slope of the envelope was calculated using linear approximation. From the slope the Q factor can be calculated using (5).

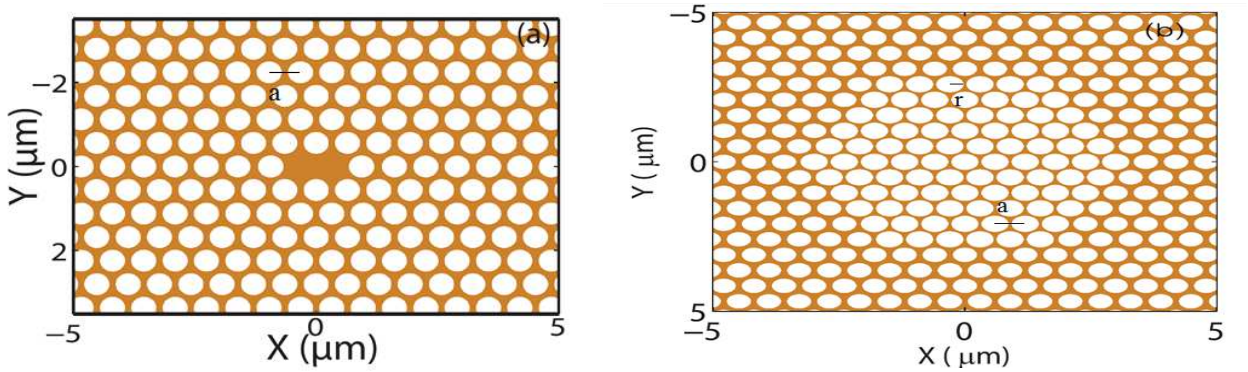

Figure 37 We have designed two PPCC devices with proper periodicity (a) and airhole radius (r). (a) A twofold defect cavity where the defect in the lattice act as the cavity. (b) A band-edge cavity where the low group velocity mode in the center is confined by bandgap mirror around it.

We propose several resonator-based devices to take advantage of the optical bandgap. They are shown in Figure 37. The top view of the designed devices can be shown in Figure 37(a) and (b). A two-fold defect, which can be created by removing two airholes from the hexagonal lattice, is shown in Figure 37(a). The lattice defect hosts mode(s) that cannot exist in the photonic crystal lattice surrounding the defect. Thus, the mode(s) should remain confined within the defect site. This results in a high quality-factor optical resonator. In Figure 37(b) a defect less resonator is shown. Here, a photonic crystal with large airholes (the core) is surrounded by another one with a smaller airholes but the same periodicity (the mirror). The dispersion property of the core PhC and mirror PhC is shown in Figure 38(a). We see that the slowest modes in the core PhC fall within the bandgap of the mirror. This is possible because the bandgap position is highly

dependent on the ratio of the radius and the period (r/a), as shown in Figure 38(b). By using Figure 38(b), it is possible to choose the radius of the core and mirror PhC so that the slowest mode of the core PhC falls within the bandgap of the mirror PhC.

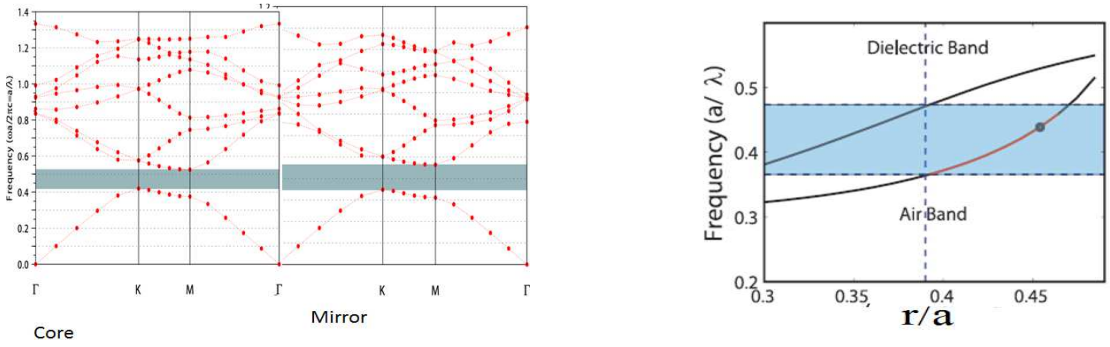

Figure 38 (a) The mode dispersion of the core and Mirror PhC. (b) The guideline for choosing appropriate r/a for desired bandgap frequency.

The 3D structure of the perturbed photonic crystal is shown in Figure 39. The planar photonic crystal cavity is designed on a glass substrate with a glass background, making it a transparent resonator. Our goal is to demonstrate the usefulness of FDTD, as well as determine the suitability of glass for nanophotonic applications. We determine the frequency response of the PPCC structures and calculate their quality factors. The dependence of the quality factor on the design parameters, such as core thickness, core refractive index and airgap width, are studied. We also investigate several applications of the PPCC, viz., refractive index sensing, temperature sensing, etc.

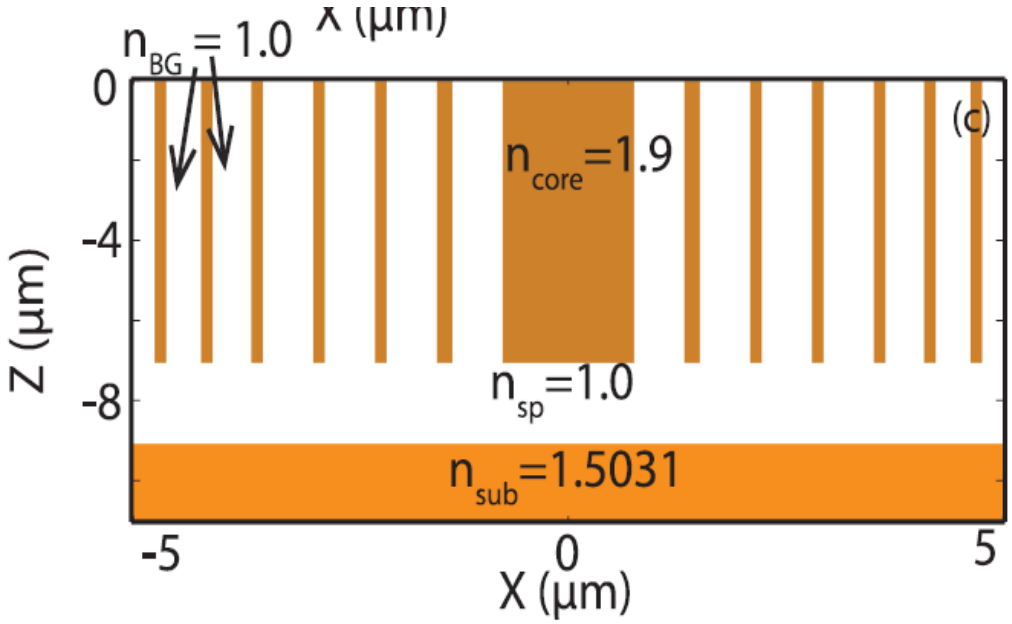

Figure 39 The 3D structure of the planar photonic crystal cavity.

The normalized spectrum of the absolute field is given in Figure 40(a), where it is evident that the structure has a resonance at $\lambda_r = 1.55\ \mu m$ which can be shifted to $\lambda_r = 0.855\ \mu m$ simply by setting *a* = 364*nm*. The resonant wavelength (λ_r) can be changed by controlling the radius (*r*) of the airholes as well as the period of the lattice (*a*). To provide a guideline for choosing the appropriate *r* and *a* for a specific λ_r, the normalized radius of the airholes ($\frac{r}{a}$) and the quality factor (Q) are plotted against the normalized resonant wavelength ($\frac{a}{\lambda_r}$) in Figure 40(b). The Q serves as the figure of merit in choosing the appropriate period *a*. Then, the airhole radius can be determined from the curve. The quality factor has been optimized by moving and changing the radius of the adjacent airholes and by setting the index of the spacer material, n_{sp} = 1.0. With optimized airhole placement and sizing, the maximum Q of the cavity can be as high as 4459 with an air spacer. It should be noted that, as shown in Figure 40(c), the Q factor is also affected by the refractive index of the spacer material, n_{sp}. Thus, Figure 40 can serve as a guideline

in designing a photonic crystal cavity with the desired resonant frequency and quality factor.

There are two relevant quantities here, the resonant wavelength and the Q-factor. To resolve the resonant wavelength, the simulation must run for close to an hour, and to calculate the decaying field with enough accuracy, the required memory is >3GB.

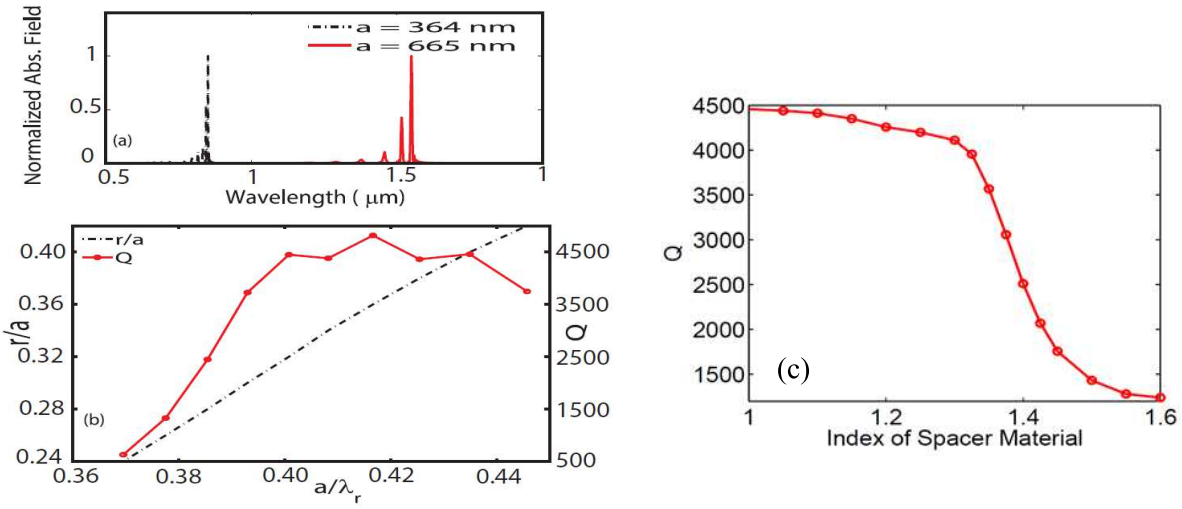

Figure 40 (a) The spectrum of the cavity. The resonance is at $\lambda_r = 1.55\ \mu m$ when a = 665nm and it is shifted to $\lambda_r = 0.855 \mu m$ when a = 364nm. (b) r/a and Q are plotted against the normalized resonant wavelength. (c) The dependence of the Q factor on nsp. Here a = 0.66 μm, r =0.264 μm and the resonant wavelength is 1.55 μm.

To determine the sensitivity of the cavity to the background material, the spectrum of the cavity has been calculated with two different background indices. It can be seen in Figure 41 that when the refractive index of the background environment (n_{BG}) is changed from n_{BG} = 1.0 to n_{BG} = 1.01, the resonant wavelength of the frequency changes from 1.528 μm to 1.532 μm, resulting in a sensitivity of 400nm/RIU. We have investigated the dependence of the sensitivity on the core thickness and the spacer thickness, and the results are summarized in Table 4. The quality factor and sensitivity increase with

increasing core thickness since the increased core thickness increases the interaction between the environment and the cavity.

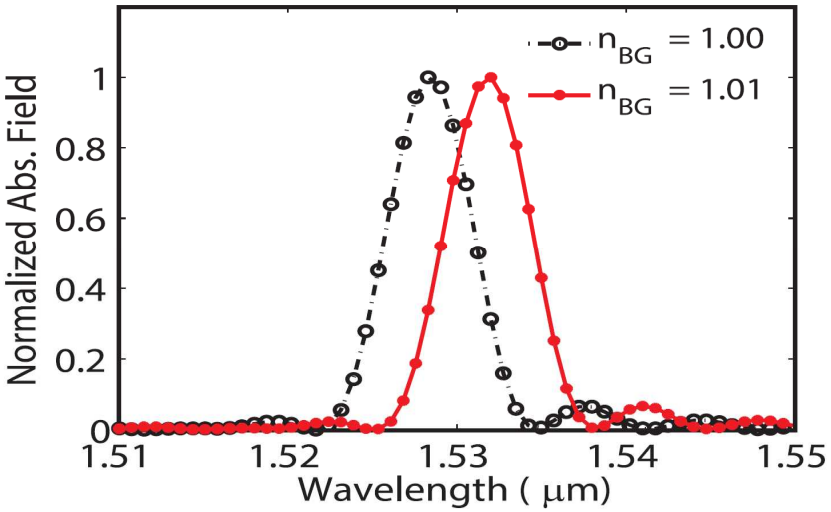

Figure 41 The spectrum of the cavity with two different refractive indices of the background environment (n_{BG}.)

Table 8 Impact of core thickness (T_{core}) and spacer layer thickness (T_{sp}) on Q factor (Q) and sensitivity (S).

T_{sp} (μm)	T_{core} (μm)	Q	S (nm/RIU)
2	3	324	100
2	5	1759	300
2	6	4459	400
2.5	6	4482	415
3.5	6	4459	415

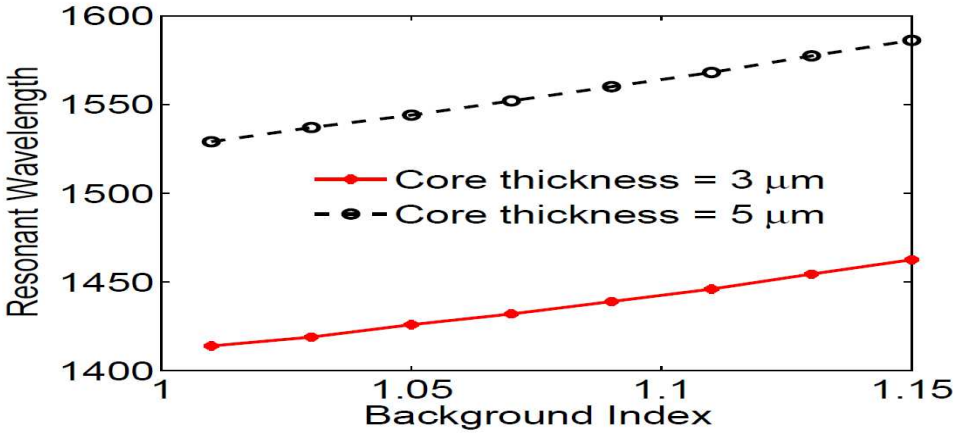

Figure 42 The resonant wavelength for the core thickness of 3 μm and 5 μm are plotted against the background index.

Figure 42 shows that the resonant wavelength increases linearly with the background refractive index. The relation between the resonant wavelength and the background index can be given as:

$$\lambda_{res} = S \times n_{BG} + C \tag{2.20}$$

where λ_{res} is the resonant wavelength, *S* is the slope, n_{BG} is the background refractive index, and *C* is a constant. Here, the slope *S* can be thought of as average sensitivity over the entire range of analyte refractive index. From Figure 42, it can be found that *S* = 322*nm/RIU* and *C* = 1087*nm* for 3 *μ*m thick core and *S* = 388*nm/RIU* and *C* = 1136*nm* for 5*μ*m thick cores. In Table 5, the Q and sensitivity of this work is compared with similar studies found in the literature. It can be observed that the refractive index sensitivity found in this work is much higher than that reported in [130, 131] .

Table 9 Comparison between the refractive index sensitivity found in this work and that in similar works in literature

Material	**S (nm/RIU)**	**Q**	**Ref.**
GaAs	-	360	[132]
Air-bridged Si	320	~10^2	[130]
Si	190	~10^6	[131]
SOI	585	~10^4	[133]
Si	-	~10^7	[134]
Airbridges Glass	388	~10^3	This work

The designed cavity is also sensitive to temperature. The refractive index of the LASF35 glass used as the core changes with temperature according to [135]:

$$n(T) = n_0 + (2.7 \times 10^{-6})\Delta T \tag{2.21}$$

where n_0 = 1.9 is the refractive index at room temperature, and $\Delta T = T - T0$ is the change in temperature. Furthermore, the glass expands with temperature. Assuming a uniform

thermal distribution and uniform linear thermal expansion, the parameters of the photonic crystal on glass are affected by the temperature according to [135] :

$$L(T) = L_0(1 + 8.5 \times 10^{-6}\Delta T) \quad (2.22)$$

where *L*0 is any length parameter of the photonic crystal cavity (e.g., period, radius) at room temperature, and *L*(*T*) is the changed parameter after thermal expansion. The total impact of the temperature on the resonance of the designed cavity is shown in Figure 43, where the spectra of the cavity at room temperature and at temperature 10◦C as well as 20◦C higher than room temperature are shown together.

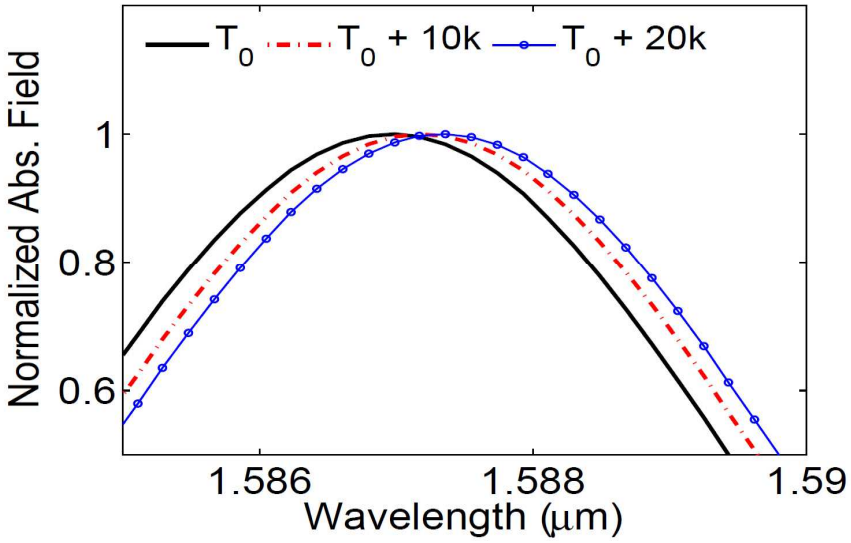

Figure 43 The spectrum of the cavity at three different temperatures T0 C, T0+10 C and T0+20 C. With rising temperature, the peak of the spectrum red shifts.

Table 10 Comparison of the temperature sensitivity calculated in this work with reported values.

Material	**Structure**	**Temp. Sensitivity**	**Ref**
Gorilla Glass	MZI	1.14	[36]
Si	PhC	6.6	[135]
Schott Glass	PhC	18.5	This work

From Figure 43, the resonance suffers a red-shift from 1589.99 nm at room temperature to 1587.17 nm at 10◦C higher temperature. When temperature is increased again by 10◦C, the resonance shifts to 1587.36 nm. From the shift in the resonant peak, the sensitivity is measured to be 18.5 pm/◦C. In Table 6, the temperature sensitivity of this work is compared with similar work in the literature. It is evident that the results in this work are significantly superior to prior reported results. Also, it can be seen that the cavity structure used in this work provides better sensitivity than the Mach-Zehnder Interferometer scheme used in [36].

In addition to glass, other low index transparent materials can be equally suitable for designing PPCC. For example, PMMA can be a suitable low refractive index material because it is cheap and easy to handle, and it has low loss. We investigated the in-plane Q-factor of PMMA PPCC for different resonant wavelengths. The dispersion and absorption effects of PMMA were taken into account [136]. As shown before, the resonant wavelength can be tuned by scaling the cavity. We adjusted the devices to have resonant wavelengths between 700 nm to 1100 nm. The different periodicity of the PhC required for the resonant wavelength in the desired range is plotted against the resonant wavelength in Figure 44(a) for the two cavities. The linear scaling is upheld.

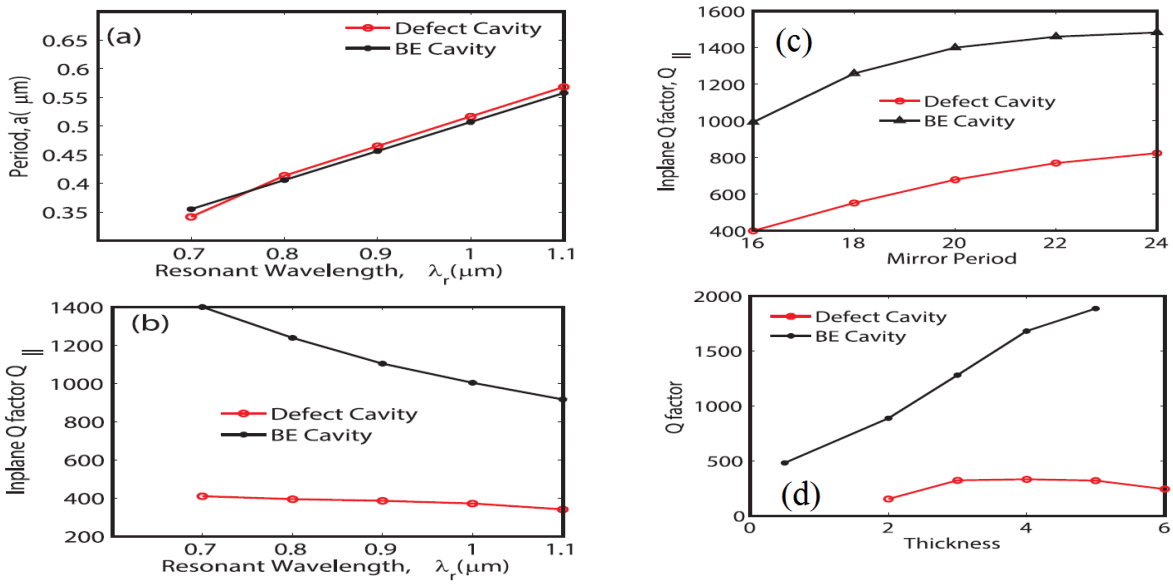

Figure 44 (a) The in-plane Q factor and (b) corresponding periods for the defect cavity and Band-edge cavity at different resonant wavelengths. (c) The in-plane Q factor of the cavities for increasing mirror depths. (d) The total Q factor of the devices for increasing thickness.

The in-plane Q-factor is plotted against the resonant wavelength in Figure 44(b). The in-plane Q-factor of the defect cavity remains around 400 while that of the band-edge cavity is around 1400. The in-plane Q is also dependent on the mirror depth, i.e., the number of periods around the cavity that act as a bandgap mirror, as shown in Figure 44(c). The in-plane Q factor can be as high as 824 in the case of a defect cavity and 1483 in the case of a band-edge cavity. The resonant wavelengths converge to the designed value when the mirror thickness is increased. The in-plane Q factor presented here compares favorably with those in [137]. The overall quality factor is dependent on the thickness of the cavity. As can be seen in Figure 44(d), the total Q factor of both cavities increases up-to a certain thickness, after which the higher absorption in the thicker layers becomes dominant and the Q factor saturates and eventually falls. With optimal thickness

and mirror depth, the defect cavity can reach Q = 737. From the above discussion, it is evident that a high Q factor nanocavity can be implemented on a low refractive index PMMA polymer.

D. Summary

Table 11 Summary of the time and memory required to calculate different quantities

Quantity	Time	Memory
F/B	5 mins	1 GB
Band Diagram	2 mins	10 MB
λ_{res}, Q-factor	1 hour	3 GB

In this chapter, we have discussed different simulation methods relevant to nanophotonics. In these methods, Maxwell's equations are solved numerically by using various approximations and simplifying assumptions. By replacing the differentials in Maxwell's equations with the central difference, numerical solutions can be derived in the FDTD method. Being a first principle method, FDTD applies to a vast array of problems, and it can produce a stable solution for most cases with the appropriate boundary conditions. The accuracy of FDTD calculations depends on the density of the spatial and temporal grid. Thus, while FDTD is very versatile, it may require sizable computational resources to be reasonably accurate. The plane wave expansion method is much faster, requiring much fewer resources, but it only applies to a periodic medium. A summary of the calculation times and memory requirements is given in Table 7.

We have demonstrated the use of both methods to characterize a single spherical scatterer, a periodic photonic crystal and a planar photonic crystal cavity. The results demonstrate the efficacy of these methods in solving a variety of problems. We have also addressed the possibility of nanophotonic devices on low index materials. We have

established that an optical bandgap may be opened for refractive indices as low as 1.5. We have also shown that transparent optical sensors can be designed on low index materials like glass or polymers by using planar photonic crystal cavities as refractive index sensors.

Based on the calculations performed in this section, it can be concluded that simulations can be useful for designing nanophotonic devices when time and resources are not limited. It is also demonstrated that low index transparent materials can be useful as nanophotonic materials.

III. EFFECTIVE MEDIUM APPROXIMATION OF OPTICAL NANOSTRUCTURE

In the previous chapter, it was discussed that numerical analysis methods are versatile but require significant time and resources to execute. Analytical effective medium approximation can be an effective tool for analyzing the properties of optical nanostructures quickly and at a low computation cost. Classically, sparse heterogeneous media containing infinitesimally small inclusions in a matrix material have been described accurately using effective medium theory. However, optical nanostructures often do not satisfy these requirements. For optical nanostructures, the inclusions are often closely packed and comparable to operating wavelength in size. Accurate effective medium approximation of such optical nanostructures remains an unsolved problem. Furthermore, numerical analyses often require assumptions of symmetry or periodicity to simplify the calculation. However, optical nanostructures are often aperiodic, with no underlying symmetry. A schematic representation of such a nanostructure is shown in Figure 45. Thus, an accurate effective medium approximation can be very useful in the design and analysis of optical nanostructures.

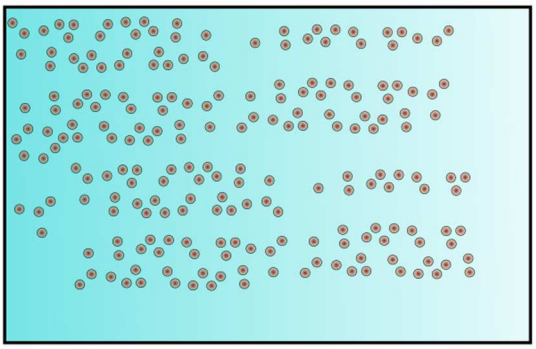

Figure 45. Schematic representation of an optical nanostructure consisting of small and dispersed inclusion in a matrix material.

Optical nanostructures containing random or regular inclusions (e.g. nanoparticles) as constituents have found applications in diverse fields such as anti-reflection coating [77], thermos-photovoltaics [100], ultra-thin optical elements [84, 96] and all-dielectric metamaterial [101]. The optical properties of such media can be controlled by changing the size, shape and optical parameters of the constituent inclusions [101]. Effective medium approximation (EMA), in addition to being fast and cheap, may also produce greater physical insight into the interplay of the physical and optical properties of the nanostructure. Numerical analyses may be more accurate, but they may fail to produce the explicit inter-relation between the configuration of the medium and its optical properties.

EMAs treat the optical nanostructure as a homogeneous medium with effective optical properties which are often explicitly related to the configuration of the optical nanostructure. In this section, the available literature on effective medium approximation of optical nanostructure is discussed. Commonly used EMAs are reviewed, and their applicability is highlighted. Finally, a generalized EMA with very wide applicability is proposed.

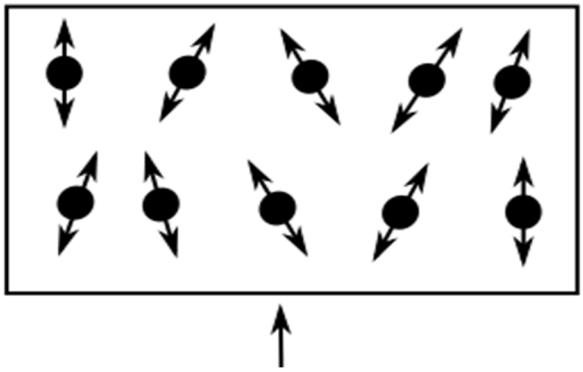

Figure 46 Medium containing nanoparticles. Each nanoparticle can be considered a dipole, which responds to the incident field

One of the first EMAs was proposed by Maxwell-Garnett in 1904 [102] while discussing optical properties of glass containing small metallic inclusions as shown in Figure 46. It was assumed that the metal inclusions were very small and spherical in size. They were approximated as point dipoles, which are much smaller than the wavelength. The dipoles responded to an incident wave by aligning themselves to the field. How well they polarized themselves was calculated using the static polarizability of the point dipole, and then the polarizability of the medium was estimated as an ensemble average of the polarizabilities of the individual inclusions. This simple approximation was justified by assuming that the inclusions are infinitesimally small and much smaller than the wavelength. From the effective polarizability, the effective permittivity of the optical nanostructure was explicitly calculated. Let us consider a linear optical nanostructure where the matrix material has a relative permittivity of ε_{mat}, and the inclusions have a relative permittivity of ε_{inc}. The dipole polarizability of the infinitesimally small inclusions can be deduced as [138]:

$$\alpha = 4\pi R^3 \frac{\epsilon_{inc} - \epsilon_{mat}}{\epsilon_{inc} + 2\epsilon_{mat}} \tag{3.1}$$

where α is the dipole polarizability of each nanoparticle and R is the radius of the nanoparticles. The effective relative permittivity (ε_{eff}) of the ensemble can be evaluated from the Claussius-Mossotti (CM) equation:

$$\epsilon_{eff} = \epsilon_{mat} \times \left(1 + \frac{n\alpha}{1 - \frac{n\alpha}{3}} \right). \tag{3.2}$$

Here, n is the volume density of the inclusion nanoparticle. Although the Maxwell-Garnett formula (MG) was very convenient, its applicability was limited [6]. For example, the inclusions must be much smaller than the wavelength of light; the fill factor must be below

the so-called percolation threshold (above the percolation threshold, there may be at least one infinitely connected component, which leads to inaccuracies between prediction and experimental value); and the inclusions must be non-interacting. Furthermore, the inclusion material and matrix material must be clearly defined. The MG formula is not symmetric to a reversal of the matrix and inclusion material.

Several attempts have been made to design an effective medium approximation without such limitations. To solve the symmetry problem, a new formula was proposed by Bruggeman which treats all components of an optical nanostructure as inclusions in the effective medium [103]. In the Bruggeman formula (BG), the inclusions are still treated as spherical point dipoles. It is assumed that the medium did not produce any electric field of its own, and the total contribution of the inclusions to the incident electric field must be zero. For example, let us consider the optical nanostructure defined above. In the case of the BG formula, the inclusion material and the matrix material are both be treated as inclusions. Their dipole polarizabilities can be calculated as:

$$\alpha_{inc} = 4\pi R^3 \frac{\epsilon_{inc} - \epsilon_{eff}}{\epsilon_{inc} + 2\epsilon_{eff}} \; ; \; \alpha_{\mathrm{mat}} = \; 4\pi R^3 \frac{\epsilon_{mat} - \epsilon_{eff}}{\epsilon_{mat} + 2\epsilon_{eff}}; \tag{3.3}$$

where α_{inc} is the effective polarizability of the inclusion and α_{mat} is the effective polarizability of the matrix. Then, the effective permittivity can be calculated form the implicit formula:

$$f\left(\frac{\epsilon_{inc} - \epsilon_{eff}}{\epsilon_{inc} + 2\epsilon_{eff}}\right) + (1-f)\left(\frac{\epsilon_{mat} - \epsilon_{eff}}{\epsilon_{mat} + 2\epsilon_{eff}}\right) = 0 \tag{3.4}$$

Where f is the inclusion fill factor. Although this approximation is symmetric, it still cannot account for finite sized interacting inclusions. Furthermore, the approximation requires solving the above equation iteratively to calculate the effective permittivity.

Volume averaging theory(VAT), applied to Maxwell's equations, was also used to define the effective medium approximation [77]. However, volume averaging also cannot account for the size and shape of the inclusions. Explicit linear effective medium approximations like series and parallel approximations were also proposed [104], which predicted effective optical parameters as series and parallel combinations of the constituent materials. Here, these explicit EMA formulas are listed for reference:

Series model:

$$n_{eff} = (1 - f)n_{mat} + f n_{inc} \tag{3.5}$$

Parallel model:

$$\frac{1}{n_{eff}} = \frac{1 - f}{n_{mat}} + \frac{f}{n_{inc}} \tag{3.6}$$

Volume Average theory:

$$n_{eff} = [n_{mat}^2(1 - f) + n_{inc}^2 f]^{\frac{1}{2}} \tag{3.7}$$

Although the above formulas are widely used in the literature, their applicability remains limited. In order to account for the size, shape, and interaction of the inclusions, it is vital to extend the existing effective medium theory. Due to its explicit nature, the MG theory is the best candidate for such an extension.

Let us consider EMA when the inclusion size is not infinitely small, as shown in Figure 47. Like that shown in Figure 46, the inclusions in this medium also polarize themselves when a field is incident on it. However, unlike the previous medium, the inclusions cannot be modeled as dipoles. To account for the finite size of the inclusions in a heterogeneous material, the polarizability of the inclusions must be calculated in a way that accounts for the size of the inclusion.

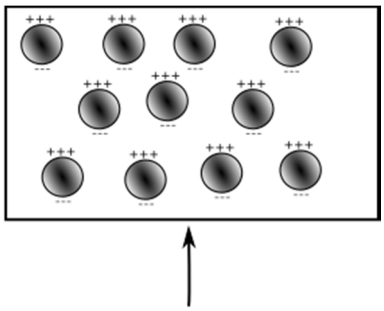

Figure 47 Medium consisting of large spherical inclusion. Each inclusion can be considered a multipole.

For finite sized particles, it has been shown that the static polarizability is not enough because the particle is subject to dynamic fields. Thus, a dynamic description of the polarizability is required [105]. In [105], Doyle et al. discussed that the electrodynamic response of a finite spherical inclusion can be expressed as a sum of ideal point multipoles, each with an appropriate multipole polarizability. These polarizabilities can be calculated from the Mie solutions [106] of the scattered field. They calculated, for example, the dipole polarizability as:

$$\alpha = i\frac{3R^3}{2x^3}a_1 \tag{3.8}$$

Where R is the radius of the sphere, x is the size parameter ($\mathrm{x} = \frac{2\pi \mathrm{R}}{\lambda}$), λ is the wavelength, and a_1 is the first Mie coefficient of the scattered field. The polarizability calculated here is different from the one used in MG equations because the internal field considered here are not static, rather the actual dynamically scattered fields are considered. By making this drastic modification, the MG formula is extended to accommodate finite sized particles. Adoption of the MG formula with different kinds of polarizability has been demonstrated in the literature, each of which approximates the internal field in the medium

differently [139-141]. These extended formulae also show much better performance in predicting experimental results.

Using the modified dynamic polarizability, the effective permittivity can be derived as:

$$\epsilon_{eff} = \frac{x^3 + 3if a_1}{x^3 - \frac{3}{2} if a_1}. \tag{3.9}$$

The above formula takes the size of the inclusion into account but assumes the size is small enough that it can be represented by a dynamic dipole. However, at a larger size, higher order poles are needed to accurately describe the electrodynamic behavior of the inclusions. Recently, an EMA was proposed which accounted for the third and fifth order dipoles [107]. The number of poles required to mode the inclusions is decided arbitrarily, which limits the application of Mie extended MG formulas. Also, these formulas cannot account for the interaction between the inclusions. As a result, the formulae derived this way are not accurate enough to justify their extra complexity in use. Thus, there remains a need to design a more general, explicit, and accurate EMA.

In this chapter, a new simplified EMA based on the Mie extension of the MG theory is proposed. The ambiguity in deciding the number of poles required to model the inclusions is addressed. Furthermore, the effective polarizability is modified to account for the interaction between the nearby inclusions. The Mie based formula requires evaluating the Bessel functions of various orders, which is computationally extensive. For the specific case when the size of the inclusion is of the order of λ/10, i.e., the Rayleigh scattering regime, the Mie formula is simplified to an explicit polynomial equation. The applicability of the MG formula, the simplified Rayleigh formula and the MG formula for different sizes and refractive indices of the inclusion material are discussed. Finally, the

derived EMA is extended to account for the layered inclusion materials. The popularity of the MG formula, despite its shortcomings, points out a need for a simple and accurate formula that can simplify the modelling of heterogeneous materials and predict the effective medium properties of artificial material with greater accuracy.

A. Derivation

In this section, a simpler and more accurate effective medium approximation will be derived by calculating the polarizability of the inclusion accurately and then relating the polarizability of the inclusions to the effective optical properties of the random optical nanostructure.

In order to derive a more accurate EMA, it is worthwhile to start by deriving the MG formula. The MG formula assumes that the inclusions are infinitesimally small. As such they can be approximated by electric dipoles. Let us consider such a sphere with radius a with dielectric permittivity ε in a constant external field $\mathbf{E}_{ext}$. The dipole moment of the sphere can be given as $\mathbf{d} = \alpha\mathbf{E}_{ext}$, where α is the static polarizability. By solving the Laplace equation, the polarizability can be obtained as:

$$\alpha = a^3 \frac{\epsilon - 1}{\epsilon + 2} \tag{3.10}$$

Then, the electric field outside the sphere can be written as:

$$E_d(\boldsymbol{r}) = \frac{3\hat{\boldsymbol{r}}(\hat{\boldsymbol{r}}.\boldsymbol{d}) - \boldsymbol{d}}{r^3} + \boldsymbol{E_{ext}} \tag{3.11}$$

While the internal field can be written as:

$$E_{int} = \frac{3}{\epsilon + 2} E_{ext} \tag{3.12}$$

where **r** is the vector along the radius of the sphere. The depolarization field (E_{dep}), which is induced by the charges on the surface of the sphere, can be written as:

$$\boldsymbol{E}_{dep} = \boldsymbol{E}_{int} - \boldsymbol{E}_{ext} = -\frac{\epsilon - 1}{\epsilon + 2}\boldsymbol{E}_{ext} = -\frac{1}{a^3}\boldsymbol{d}. \tag{3.13}$$

Integrating the depolarization field over the volume, we obtain:

$$\int_{r<a} E_{dep}\, dV = -\frac{4\pi}{3}\boldsymbol{d} \tag{3.14}$$

Thus, the total field induced by the dipole can be written as:

$$E_d(\boldsymbol{r}) = \frac{3\hat{\boldsymbol{r}}(\hat{\boldsymbol{r}}.\boldsymbol{d}) - \boldsymbol{d}}{r^3} - \frac{4\pi}{3}\delta(\boldsymbol{r}). \tag{3.15}$$

Where $\delta(\boldsymbol{r})$ is a dirac-delta function. The first part of the above equation is the field created by the dipole around the sphere, and the second part is the field created within the dipole. It is important to note that when the induced electric field is integrated over the sphere, the first term in the above equation reduces to zero, but the second term remains.

Now, let us consider a random optical nanostructure with volume V which contains N such spheres with radius a. Each sphere can be considered an inclusion with linear polarizability α. Since, in a macroscopic sense, only the depolarizing field remains in the expression for the dipole electric field, we can neglect the interaction between the spheres and assume each spherical inclusion experiences the same field E_{ext}. Thus, the total dipole moment of the medium can be written as:

$$\boldsymbol{d_{tot}} = N\alpha\boldsymbol{E}_{ext} \tag{3.16}$$

where d_{tot} is the total dipole and N is the number of inclusions. On the other hand, if the medium is assigned a, with effective permittivity ϵ_{eff}, then the total dipole moment can be written as:

$$d_{tot} = V\boldsymbol{P} = V\frac{\epsilon_{eff} - 1}{4\pi}\, E. \tag{3.17}$$

Where E is the total field inside the random medium. The total field can be related to the external applied field as:

$$E = E_{ext} + \overline{E_n(r)} \tag{3.18}$$

Where $\overline{E_n(r)}$ is the ensemble average of the fields induced by each dipole. It can be given as:

$$\overline{E_n(r)} = \frac{1}{V}\int_V E_d(r - r_n)\, d^3r = -\frac{4\pi}{3}\frac{\boldsymbol{d}}{V} \tag{3.19}$$

Then, the field inside the medium can be given as:

$$E = E_{ext} + \overline{E_n(r)} = \left(1 - \frac{\frac{4\pi}{3}\alpha}{\nu}\right)E_{ext}. \tag{3.20}$$

Here, we have used d = αE_{ext} and ν = N/V. Now, equating the two expresions for total dipole d_{tot}, we obtain,

$$N\alpha = \frac{nf\left(\epsilon_{eff} - 1\right)}{4\pi}\left(1 - \frac{\frac{4\pi}{3}\alpha}{\nu}\right), \tag{3.21}$$

Which can be simplified to

$$\epsilon_{eff} = 1 + \frac{\frac{4\pi\alpha}{\nu}}{1 - \frac{4\pi\alpha}{3\nu}} \tag{3.22}$$

By substituting $f = \frac{4\pi}{3}\frac{a^3}{\nu}$ and $\alpha = a^3\frac{(\epsilon-1)}{\epsilon+2}$, we obtain:

$$\epsilon_{eff} = \frac{1 + 2f\frac{(\epsilon - 1)}{\epsilon + 2}}{1 - f\frac{(\epsilon - 1)}{\epsilon + 2}}, \tag{3.23}$$

Which is the MG EMA equation. During the derivation of (3.23), several assumptions were made. For example:

It was assumed that the spherical inclusions were infinitesimally small. Thus, treating the interaction between the external field and the inclusions as an electrostatic problem was justified. The spheres were treated as static electric dipoles, and the magnetic interactions were ignored. Thus, the definition of effective polarizability was given as $\alpha = \frac{\epsilon-1}{\epsilon+2}$. It was assumed that all the inclusions experience the same external electric fields. Thus, the inter-inclusion interactions were ignored.

The first step towards deriving a more accurate EMA formula is to formulate the effective polarizability that accounts for all the interactions between the external field and the scattered field of the spherical inclusions. While the electrodynamic response of the optical nanostructure is a many body problem, we can envision the medium as a black box where the scattering and absorption of external fields by the spherical inclusions take place. In the output from this black box, it would not be possible to distinguish between the scattering and absorption. Then, the effective polarizability of an individual inclusion can be calculated from its extinction, which considers both scattering and absorption as a form of loss.

In this approach, a medium containing spherical inclusions of arbitrary size is assumed to be a black box, onto which light is incident. Due to scattering and absorption, the incident light suffers attenuation. For a causal, isotropic, and passive system, this attenuation can be described by the Beer-lambert Law:

$$\mathrm{I} = \mathrm{I}_0 e^{-\phi d} \tag{3.24}$$

Where I_0 is the input light intensity, *I* is the output light intensity, d is the medium thickness and ϕ is the absorption coefficient. It is possible to assign a dielectric constant to the medium from this information. Assuming the system is causal, the imaginary part of the

effective dielectric constant is related to the absorption coefficient and the real part can be calculated using Kramer-Kronig relationship. Thus, it may possible to assign an EMA to a medium containing arbitrarily large particles if they are used to calculate transmission and reflection.

In order to calculate the dielectric constant described above, the similarity of extinction coefficient and effective permittivity when calculating optical density can be harnessed [107]:

$$\log\left[\left(1-R_{eff}\right)^2 e^{\sigma_{ext}\rho d}\right] = \log\left[\left(1-R_{eff}\right)^2 e^{\frac{2\pi Im\left(\epsilon_{eff}\right)}{\lambda Re\left(\sqrt{\epsilon}_{eff}\right)}d}\right] \tag{3.25}$$

Thus, the above-mentioned black box can be described by a dielectric constant by accounting for the extinction of each spherical inclusion. Since the spherical inclusions are finite in size, their extinction can be calculated by approximating the local field around each inclusion by the scattered field from a weighted sum of an ensemble of multipoles. The weight of each multipole is essentially the corresponding coefficient in the Mie expansion of the scattered field from a sphere. Thus, the modified multipole polarizability can be deducing as:

$$\alpha_{\text{eff}} = \frac{2\pi R^3 \epsilon_0}{x^3}\left[\sum_{n=1}^{\infty} i(2n+1)(a_n + b_n)\right], \tag{3.26}$$

by using the relationship between extinction coefficient and polarizability [142]. Here, a_n and b_n represent the Mie scattering coefficients of the E-type and H-type modes of increasing order, respectively. They can be calculated as:

$$a_n = \frac{m\psi_n(mx)\psi_n'(x) - \psi_n(x)\psi_n{}'(mx)}{m\psi_n(mx)\xi_n'(x) - \xi_n(x)\psi_n'(mx)}, \tag{3.27}$$

and

$$b_n = \frac{\psi_n(mx)\psi_n'(x) - m\psi_n(x)\psi_n'(mx)}{\psi_n(mx)\xi_n'(x) - m\xi_n(x)\psi_n'(mx)}, \tag{3.28}$$

where ψ_n and $\xi_n$are the Ricatti-Bessel functions, and $m = \frac{n_{inc}}{n_{mat}}$ is the ratio of the complex refractive index of the inclusion (n_{inc}) and matrix (n_{mat}) material. A comparison between eq. (3.26) and eq. (3.10) indicates that the polarizability described by eq. (3.26) contains higher order multipoles, i.e., it accounts for the complicated scattered field around a particle of arbitrary size. Here, by assuming the particles are non-interacting, far away from each other, and identical, the effective dielectric constant from the multipole polarizability can be derived using CM equations [107, 143]. By using the multipole polarizability with the CM equation, the detailed scattered fields within the optical nanostructure considered in (6) are averaged out when calculating the effective dielectric constant. This effective dielectric constant cannot be arbitrarily applied in all calculations. However, based on the assumptions, the dielectric constant derived using this formalism is accurate when calculating the transmission.

The number of terms in eq. (3.26) required for accurate EMA prediction is not immediately clear. In the literature, an arbitrary number of terms has been used [107, 143]. A more rigorous approach would be to include terms enough to achieve convergence. The number of terms required for the convergence of the Mie series when 1<x<200 and precision up to 10 decimal place is given as [144]:

$$N = x + 3.52761\, x^{\frac{1}{3}} - 4.1. \tag{3.29}$$

Where x is the size parameter. In Figure 48, the extinction cross section of a sphere, which is predicted by the Mie formula curtailed at N, is compared to the extinction cross

section calculated directly by the FDTD method. Curtailing the Mie series at N produces sufficiently accurate results. To test the accuracy of this curtailing, let us consider the scattering cross section (SCS) and extinction cross section (ECS) of a sphere. From the Mie theory, the SCS can be given as:

$$SCS = \frac{2}{x^2}\sum_{n=1}^{\infty}(2n+1)(|a_n|^2 + |b_n|^2). \tag{3.30}$$

$$ECS = \frac{2}{x^2}\sum_{n=1}^{\infty}(2n+1)Re(a_n + b_n).$$

In Figure 48, it is shown that curtailing the Mie series at N terms produces a sufficiently accurate prediction of extinction.

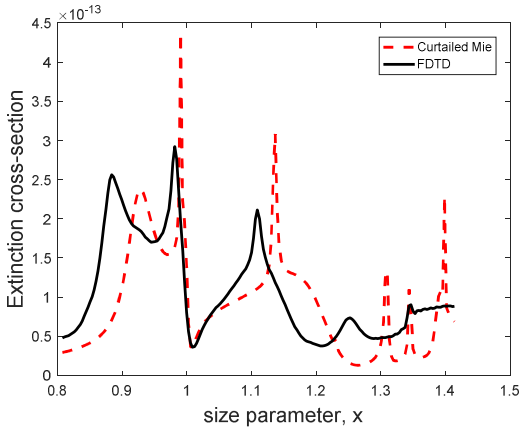

Figure 48. Comparison of the extinction cross section calculated using FDTD method and the curtailed Mie formula.

In Figure 49, the scattering cross section of a sphere is plotted against the size parameter for different relative refractive indices (m). The scattering cross section is calculated by considering one (first order approximation), two (second order approximation) and all N (total) terms. Although the first or second order approximation produces accurate results when x and m are small, the higher order terms are necessary

when x and m are larger. Thus, in this work, all N terms are considered when calculating the effective polarizability.

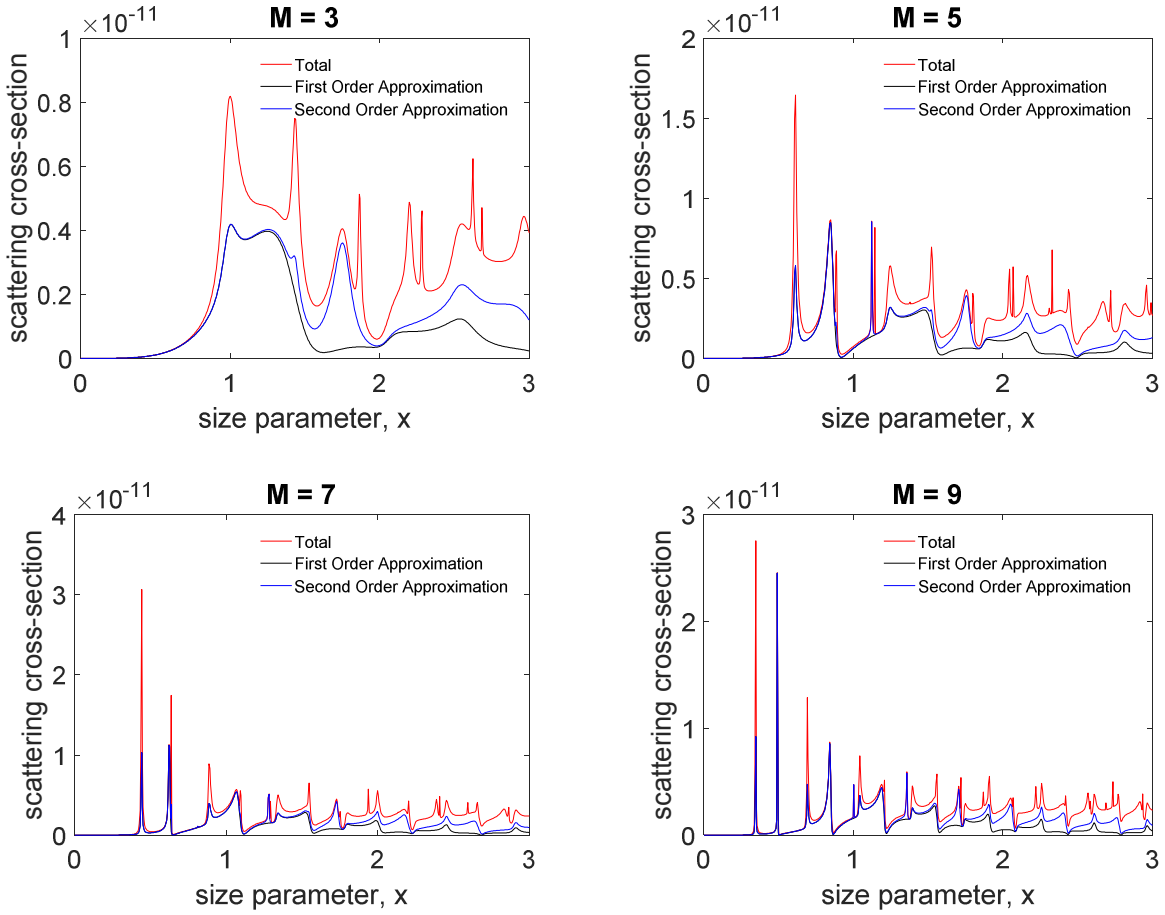

Figure 49. The scattering cross-section of a sphere for m= 3, m = 5, m = 9. m = 7 (clockwise).

Thus, combining eq. (3.26) and eq. (3.29), we obtain:

$$\alpha_{\text{eff}} = \frac{2\pi R^3 \epsilon_0}{x^3}\left[\sum_{n=1}^{N} i(2n+1)(a_n + b_n)\right], \tag{3.31}$$

The effective polarizability defined in (3.31) can account for the scattering and absorption from spherical inclusions of finite size. In order to account for the interaction between the particles, a net polarizability can be formed [145]:

$$\alpha_{\perp} = \frac{2\alpha^2 - \frac{\alpha^2}{2\pi l^3}}{1 - \frac{\alpha^2}{(4\pi\, l^3)^2}} \tag{3.32a}$$

$$\alpha_{\parallel} = \frac{2\alpha + \frac{\alpha^2}{2\pi l^3}}{1 - \frac{2\alpha^2}{(2\pi l^3)^2}} \tag{3.32b}$$

$$\alpha_{net} = \frac{1}{2}(\alpha_{\perp} + \alpha_{\parallel}) \tag{3.32c}$$

Here, $\alpha_{\perp}$ is the perpendicular component of the polarizability, $\alpha_{\parallel}$is theparallel component, α_{net} is the net polarizability, l is the average distance between the inclusions, and α is the polarizability described in (3.31).

To separate the contribution of E-type and H-type modes, the polarizability can be separated into magnetic and electric components as [12,13]:

$$\alpha_{\text{net}} = \alpha_{(e)} + \alpha_{(m)}. \tag{3.33}$$

Here, $\alpha_{(e)}$is the effective electric polarizability containing all the $a_n$term, and $\alpha_{(m)}$is the effective magnetic polarizability containing all the $b_n$terms in (1). From these effective polarizabilities, the effective permeability (μ_{eff}) and effective permittivity (ϵ_{eff}) can be calculated as [9-11,14]:

$$\epsilon_{eff} = \epsilon_{mat} \times \left[1 + \frac{F\alpha_{(e)}}{v - 0.33F\alpha_{(e)}}\right], \tag{3.34a}$$

$$\mu_{eff} = \mu_{mat} \times \left[1 + \frac{F\alpha_{(m)}}{v - 0.33F\alpha_{(m)}}\right] \tag{3.34b}$$

where $\epsilon_{eff}$is the effective permittivity of the medium, ϵ_{mat} is the permittivity of the matrix material, μ_{eff} is the effective permeability of the medium, $\mu_{mat}$is the permeability of the matrix material, *F* is the filling factor, and *v* is the volume of an individual particle. To

calculate the effective refractive index, we used the well-known formula $n_{eff} = \sqrt{\epsilon_{eff}\mu_{eff}}$.

In eq (3.35), the polarizability accounts for all the losses from absorption and scattering. Thus, it can be used for calculating the reflection and transmission of optical nanostructures. This formula can be easily extended to the cases of layered inclusions. The Mie coefficients for a layered sphere with two layers can be given as:

$$a_n = \frac{\psi_n(y)[\psi_n'(m_2y) - A_n\chi_n'(m_2y)] - m_2\psi_n'(y)\left[\psi_n(y)\left[\psi_n\,(m_2y) - A_n\chi_n\,(m_2y)\right]\right]}{\xi_n(y)[\psi_n'(m_2y) - A_n\chi_n'(m_2y)] - m_2\xi_n'(y)\left[\psi_n(y)[\psi_n\,(m_2y) - A_n\chi_n\,(m_2y)]\right]} \quad (3.35a)$$

$$b_n = \frac{m_2\psi_n(y)[\psi_n'(m_2y) - B_n\chi_n'(m_2y)] - \psi_n'(y)\left[\psi_n(y)\left[\psi_n\,(m_2y) - B_n\chi_n\,(m_2y)\right]\right]}{m_2\xi_n(y)[\psi_n'(m_2y) - B_n\chi_n'(m_2y)] - \xi_n'(y)\left[\psi_n(y)[\psi_n\,(m_2y) - B_n\chi_n\,(m_2y)]\right]} \quad (3.35b)$$

Where A_n and B_n are defined as:

$$A_n = \frac{m_2\psi_n(m_2x)\psi_n'(m_1x) - m_1\psi_n'(m_2x)\psi_n(m_1x)}{m_2\chi_n(m_2x)\psi_n'(m_1x) - m_1\chi_n'(m_2x)\psi_n(m_1x)} \quad (3.35c)$$

$$B_n = \frac{m_2\psi_n(m_1x)\psi_n'(m_2x) - m_1\psi_n\,(m_2x)\psi_n(m_1x)}{m_2\chi'_n(m_2x)\psi_n\,(m_1x) - m_1\psi_n'(m_1x)\chi_n(m_1x)} \quad (3.35d)$$

Here m_1 and m_2 are the relative refractive index of the first and second layer, x is the size parameter in the first layer, y is the size parameter in the second layer. By replacing the Mie coefficients in (3.36) into (3.31), the effective refractive index of an optical nanostructure containing layered inclusions can be calculated.

Although the EMA discussed above can account for arbitrary sized inclusions, its expression is not straight forward and the relations between the variables are not

apparent. To simplify the expression, we consider the case of uniform inclusions when R <λ/10. The Mie coefficients can be expressed in polynomial form after expanding the Ricatti-Bessel functions in power series. We get:

$$a_1 = -\frac{ix^3}{3}\frac{m^2-1}{m^2+2} - \frac{i2x^5}{5}\frac{(m^2-2)(m^2-1)}{(m^2+2)^2} + \frac{4x^6}{9}\left(\frac{m^2-1}{m^2+2}\right)^2 + O(x^7) \quad (3.36a)$$

$$a_2 = -\frac{ix^5}{15}\frac{m^2-1}{2m^2+3} + O(x^7) \quad (3.36b)$$

$$b_1 = -\frac{ix^5}{45}(m^2-1) + O(x^7) \quad (3.36c)$$

$$b_2 = O(x^7) \quad (3.36d)$$

Thus, for cases that adhere to the Rayleigh scattering condition, we obtain,

$$\alpha = 4\pi R^3 U\left[1 + \frac{x^2}{15}UV + \frac{i2x^3}{3}U\right] \quad (3.37)$$

Where

$$U = \frac{m^2-1}{m^2+2}; V = \frac{m^4+27m^2+38}{2m^2+3}.$$

Substituting the polarizability calculated in (3.38) into the MG equation we obtain

$$n_{eff}^2 = \epsilon_{mat}\left(\frac{1+2fU\left[1+\frac{x^2}{15}UV+\frac{i2x^3}{3}U\right]}{1-fU\left[1+\frac{x^2}{15}UV+\frac{i2x^3}{3}U\right]}\right) \quad (3.38)$$

Thus, a simple effective medium approximation can be derived from the Mie solution.

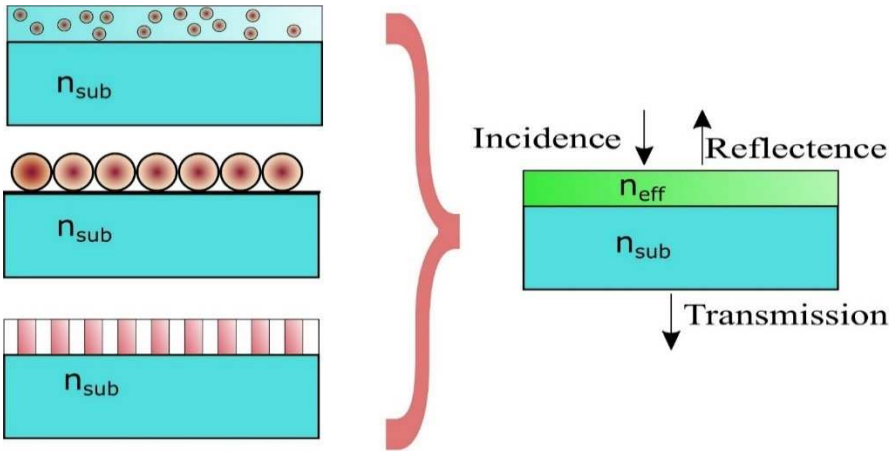

Figure 50 Random heterogeneous nanostructure is characterized with effective medium. Nanostructure with spherical and cylindrical inclusions are studied.

B. Method

In order to experimentally verify the EMA formulas derived in (3.34) and (3.38), the transmission and reflection of the optical nanostructures calculated using the EMA are compared to the experimental data found in the literature as well as those obtained in-house.

1. UNIFORM SPHERICAL INCLUSIONS:

First, the validity of the EMAs for uniform inclusions was tested. The experimental data from literature were selected so that the validity of the EMA could be tested in a wide range. In Table 12, the structural parameters of the chosen experimental random media are shown.

Table 12 The chosen experimental data from literature to test the EMA formulas.

Inclusion Material	Inclusion Radius [nm]	Filling Factor	Thickness [nm]	Reference
SiO_2	52.5	0.445	105	[77]
SiO_2	40	0.25	80	[78]
	60	0.25	120	
SiO_2	55	0.6	110	[79]
	105	0.6	210	
Al_2O_3	20	0.007	3800	[100]

Au	5.7	0.0057	Bulk	[146]

The uniform Mie model (3.34) and the Rayleigh model (3.38) developed here was compared with several existing EMA formulas from the literature as well as experimental results. We considered the parallel model (3.6), the series model (3.5), the volume averaging (VA) model (3.7), the Bruggeman (BG) model (3.4) and the MG (3.2) model for comparison with the developed EMA formulas. Although all the EMA formulas considered in this work describe bulk medium, they can predict the effective parameters of thin-films with reasonable accuracy [104]. Thus, to measure the usefulness of the EMAs, we calculated the reflectivity of thin-film anti reflection (AR) coatings using the developed and other EMAs and compared with experimental results. Our approach is summarized in Figure 50. We examined the accuracy of the models using least square error. The error is defined as:

$$Error = \sqrt{\frac{1}{L}\left[\sum_{i=1}^{L}(Experimental\ value_i - EMA\ value_i)^2\right]} \tag{3.39}$$

Where L is the number of data points.

In order to calculate the optical properties of random heterogeneous materials using the EMA, we used the well-known transfer matrix method (TMM). In TMM, the problem of calculating the reflectance, transmittance and absorbance of a multilayer structure reduces to a matrix multiplication problem. This process is summarized in Figure 50.

2. COATED SPHERICAL INCLUSIONS

To test the EMA for coated spherical inclusions, a magnetic microsphere colloid (MMC) was obtained and its transmission was experimentally observed. Then the observed transmission was modelled using the designed EMA. The MMC were prepared by diluting colloids purchased from Bang Laboratories with deionized water. The purchased colloids contained 97.5% water and 2.5% magnetic microspheres, which are composed of Iron (III) oxide (Fe_3O_4) core and a proprietary polymer shell. The mean outer diameter of the microspheres was 1.05 □m.

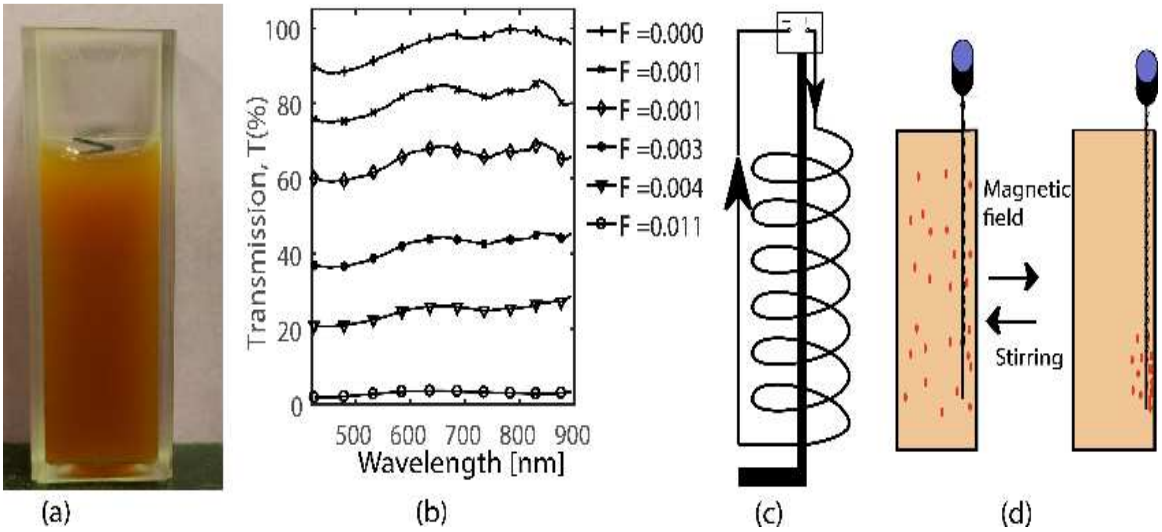

Figure 51 (a) The prepared sample in a 10-mm cuvette, (b) the measured transmission of the samples at different filling factors, (c) the actuator, consisting of a stirrer with an electromagnetic coil around it, (d) the catch and release mechanism of the actuator.

Samples with different filling factors were prepared by varying the amount of added water. The precise filling factors of the prepared samples were unknown. These samples were placed in optical cuvettes with 5mm and 10 mm optical path-length. One such sample is shown in Figure 51(a). To measure the transmission of the MMC, the samples were placed in the optical path of a spectrometer (Ocean Optics USB-2000+VIS-NIR) with 2048 element silicon linear CCD array, 0.3 nm resolution, and a spectral range of

200-1100 nm, using an incandescent light source. During data acquisition, each scan lasted 5 ms, and an average of 5 scans were used to boost the signal quality. The measured transmissions of samples with different filling factor are shown in Figure 51(b), demonstrating the change in transmission with filling factor. The filling factors were extracted using theoretical modelling. The tunability of the transmission was studied by measuring the average transmission in the wavelength range 400 – 1100 nm using a photodetector, while the sample was subjected to static magnetic field. For the optical measurements, the spot size of the incident light on the cuvette had a diameter 1 mm.

A miniature electromagnetic actuator was built for demonstrating magnetically tunable transmission of the MMC. It consisted of an electromagnet coiled around a mechanical stirrer, as shown in Figure 51(c). The electromagnetic consisted of 1000 turns of enameled copper wire around a steel rod with diameter 1 mm. When the electromagnet of the actuator was activated, the resulting magnetic field separated the magnetic microspheres from the colloid, thus reducing its filling factor. Similarly, the actuator re-disperses the microspheres by mechanical stirring, thereby restoring the filling factor. Thus, the filling factor of the aqueous MMC can be controlled, as demonstrated in Figure 51(d).

C. Range of Validity

We arrived at an EMA which can account for the finite size of the nanosphere inclusions and their interactions. In this section, the EMA is tested by comparing its prediction with experimental values from the literature.

An important property of the derived EMA is that it accounts for the Mie scattering. It is known that electrostatic interactions and Rayleigh scattering are simply special cases

of the Mie scattering. It is illuminating to note that this property of Mie scattering is upheld in the derived EMA. For example, the Rayleigh scattering approximation can be derived simply by expanding the Mie coefficients in power series of relative refractive index (m) and size parameter (x) and curtailing the series at the sixth power. Interestingly, the MG formula, which only considers electrostatic interactions, can also be derived from the Mie coefficients by curtailing the Mie power series at the third power. Thus, by curtailing the Mie coefficients at different power, i.e., by approximating the Mie scattering with different accuracy, we arrive at the Rayleigh approximation and the MG approximation. This connection gives us a tool to assess the applicability of the Rayleigh and MG approximation systematically. It is known that MG approximation applies when the size parameter is much smaller than unity [6] but a specific range is not specified in the literature. Additionally, from the above discussion, the accuracy of the curtailed series should clearly depend on both relative refractive index (m) and size parameter (x).

We calculated the errors in the Rayleigh approximation and the MG approximation with respect to the complete Mie solution and set limits of applicability on the approximations. Using the limits of Rayleigh regime ($R/\lambda \leq 0.1$) as a guideline, we set a 3% error tolerance limit empirically. A lower tolerance would exclude many known acceptable uses of MG formula, and a higher tolerance would produce erroneous results by using of the Rayleigh formula.

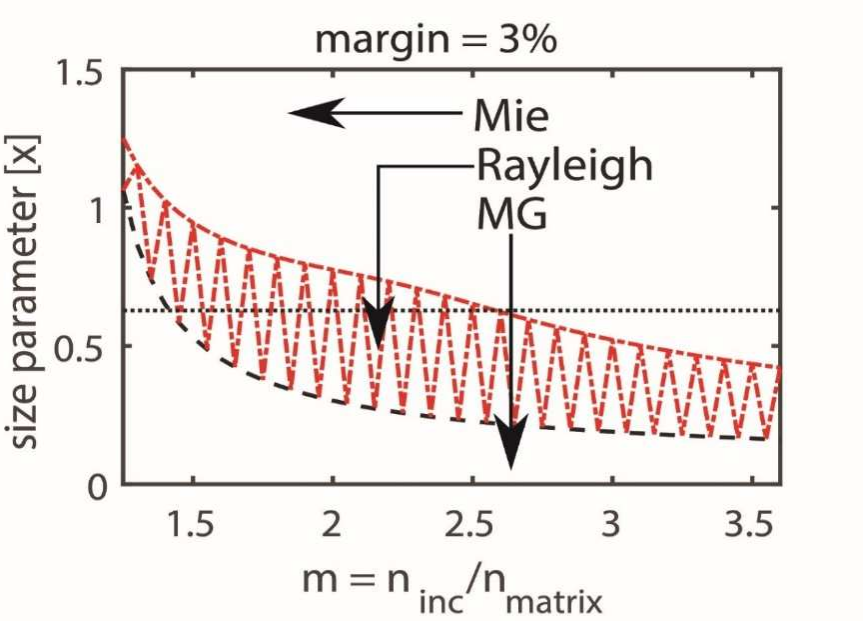

Figure 52 The range of applicability of the Rayleigh approximation and the MG approximation.

In Figure 52, the limits on the relative refractive index (m) and the size parameter (x) for using these approximations are plotted. When the m and x fall within the white area at the bottom, the MG approximation is enough, but when they fall within the hatched zone, the Rayleigh approximation must be used. When they fall in the white area above, the Mie model must be employed for accurate result. From the figure, it can be observed that the definition of Rayleigh regime, considered to be $R/\lambda < 0.1$, is also dependent on m. The dotted line in the figure marks the boundary for the Rayleigh approximation, as reported in the literature. However, it can be observed from Figure 52 that the MG formula is sufficient within this bound when $m < 1.5$, i.e., when the inclusions do not have a particularly high refractive index compared to the matrix material. On the other hand, when $m > 2.6$, the Mie formula must be used. That is, when the inclusion is high refractive index material, the scattering is strong enough that the Mie formula must be used regardless of size. Similarly, the MG and Rayleigh formulas are enough above this bound

when m <1.5 and 2.6, respectively, and x is within the appropriate range. Thus, it can be concluded that the condition for using the MG and Rayleigh approximation is weak scattering, whereas the Mie formula must be used if the scattering is strong.

D. Results

1. PERIODIC NANOSTRUCTURE AS AR COATING

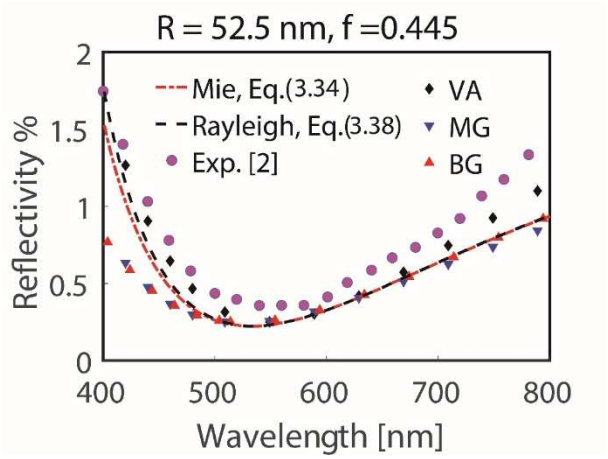

Figure 53 The reflectivity of a glass slab coated with polystyrene nanosphere is calculated using EMAs and compared with experimental data [77].

To experimentally verify the derived EMAs, we compared the experimental value of different experiment, summarized in Table 12, with corresponding EMA predictions. Polystyrene microspheres with 52.5 nm radius, deposited on a glass substrate, has been reported as AR coating [77]. The microsphere layer can be modeled as an effective medium containing spherical inclusions in a matrix of air. Then the reflectivity can be calculated by treating the system as a simple multilayer arrangement. The calculated reflectivity is compared with experimental result [77] in Figure 53. The MG and BG EMAs produce result that differs from the experimental result. This is due to the finite size of the nanospheres. On the other hand, the Mie and Rayleigh based EMAs produce much closer

results. We also see that the VA model produces the best match, while the series and parallel models (not shown) produce the worst fit.

The silica nanospheres of different radii have also been reported as AR coating [78]. We calculated the reflectivity of the silica AR coating by modelling the silica coating layer with the derived EMA. The calculated results are compared with experimental results for silica microspheres with different radii in Figure 54.

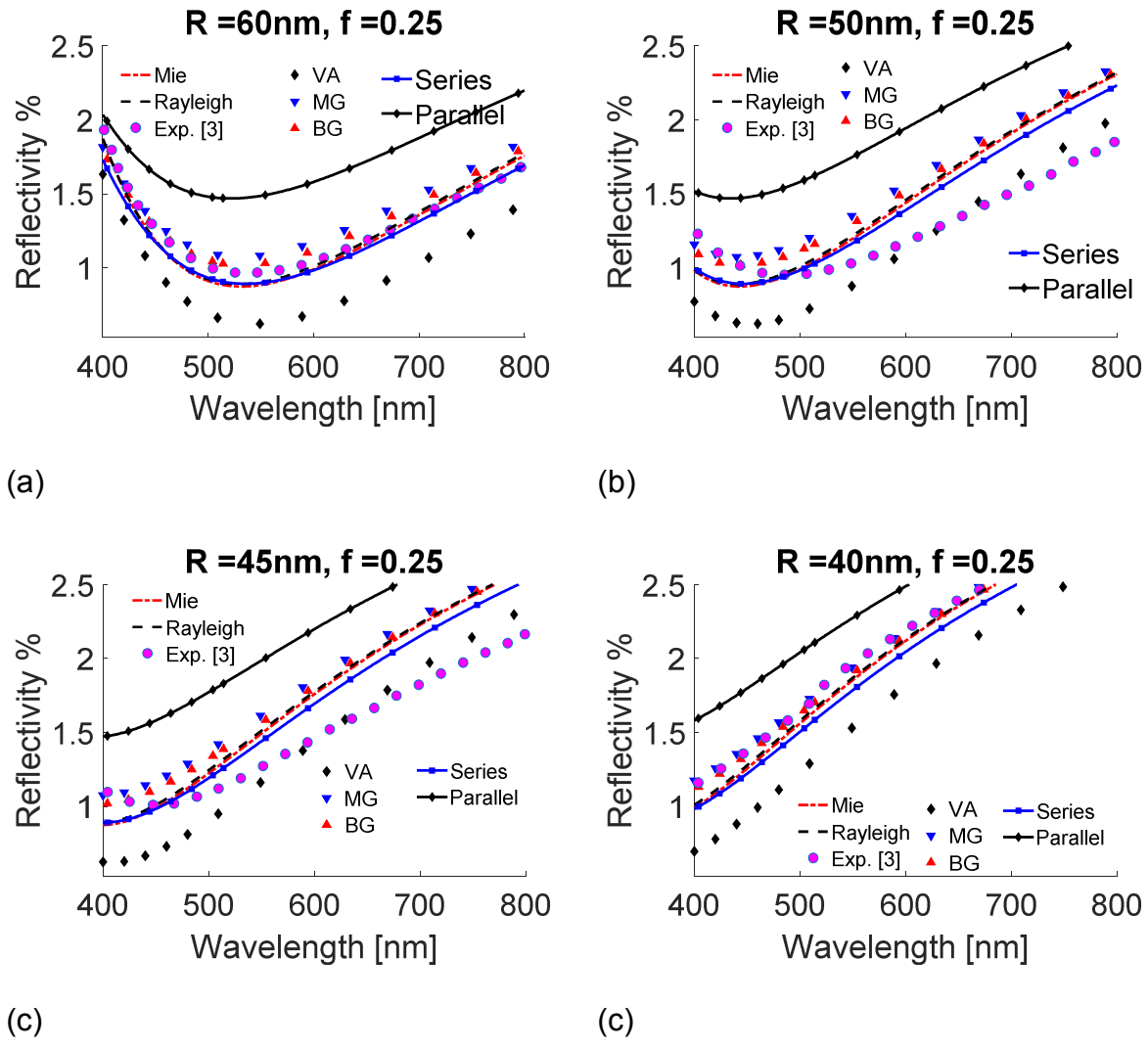

Figure 54 The reflectivity curves of a glass slab coated with silica nanospheres of different radii are calculated using EMA and compared with experimental result [78].

For microspheres with a 60nm radius, the Mie model produces almost an exact match and the Rayleigh model also produces a very accurate match whereas the VA, series and parallel models produce a worse fit than any other model. Results for 60 nm radius nanospheres are summarized in Figure 54(a). We also calculated similar results when the silica nanosphere radius is 50nm, 45nm and 40 nm. The results are shown in Figure 54 (b), (c), and (d), respectively. The Mie and Rayleigh EMA produces the best fit in all cases, while the other EMA produces higher errors.

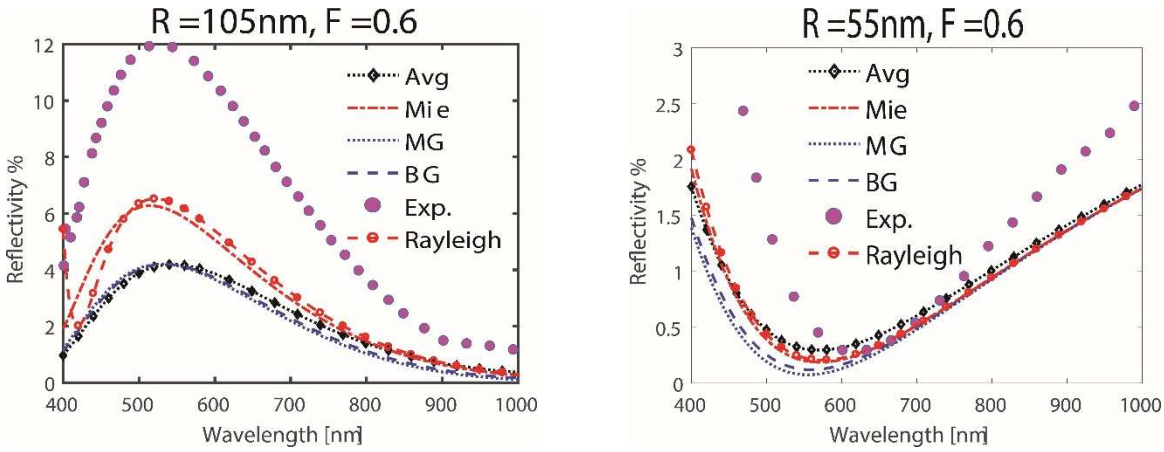

(a) (b)

Figure 55. The reflectivity of glass slab coated with silica nanosphere is calculated using EMA and compared to experimental result [79].

Silica nanosphere layers with a much higher volume filling fraction (f=0.6) are also reported [79] in Figure 55. We calculated that for microspheres of 55 nm and 105 nm radius, all models underestimate the experimental result, but the Mie and Rayleigh models produce the closest match. The discrepancy is because the EMAs employed in this work assume low filling factor. By accounting for larger sized particles, the Mie and Rayleigh model produces much less error compared to other EMA models. Results for 55 nm and 105 nm radius nanospheres are shown in Figure 55. Although the Rayleigh model doesn't apply for this case it still produces less error than the MG, BG and VA

models. It is observed in that when the radius of inclusions and filling factor is high, the Mie and Rayleigh models show best match to experimental result. It is noteworthy that the Rayleigh model agrees exactly to the Mie model when R/λ<0.1.

2. APERIODIC NANOSTRUCTURE AS TUNABLE WINDOW

a) Theoretical modelling

The EMA modelling of the MMC is summarized in Figure 56. The layered structure of the magnetic microspheres with all the structural parameters is shown in Figure 56(a). The outer radius (R_{out}) was specified by the vendor to be 525nm, while the permittivity of iron oxide ($\epsilon_{iron\ oxide}$) was also known. Along with the filling factor, the permittivity of the polymer ($\epsilon_{polymer}$) and the inner radius (R_{in}) of the microspheres were unknown parameters. We used the derived Mie based EMA in (3.34) with core-shell particle (CSP) scattering parameters in eq. (3.35) to directly model the medium containing layered microspheres as an effective medium, as shown in Figure 56(b). For comparison, we also modeled the MMC using uniform particle EMA, the MG, BG and VA formulas. When using these formulas, the layered microspheres were first approximated as uniform spheres using the MG formula. Then the medium containing the approximated uniform spherical inclusion was modeled as an effective medium, as shown in Figure 56(c). The transmission of the MMC was calculated using the Fresnel equations, where effective parameters of the MMC obtained from EMAs were used.

Table 13 The unknown parameters extracted by different EMA.

EMA	R_{IN}(NM)	N_P	F
CSP EMA	225	1.4	0.004
UNIFORM MIE	167	1.9	0.003
MG	100	1.6	0.008
BG	146	1.7	0.07

VA	118	1.9	0.003

For each model, the unknown parameters were extracted by the iterative least error fitting of the calculated transmission to the experimentally obtained values. These extracted parameters are shown in Table 1. They represent the best-fit of the experimentally obtained transmission by each EMA, respectively. The best-fits for the different EMA are compared with the experimental results in Figure 56(d). The CSP EMA matches the experimental value with the least amount of error. The uniform Mie model produces a better fit than the MG, BG, and VA models, but it remains inaccurate compared to CSP EMA. As expected, the worst prediction is obtained when the MG, BG and VA models are used. Not only do these EMAs predict peaks at inaccurate wavelengths, they also fail to predict the trends of the transmission curve. Based on the findings above, it can be concluded that the CSP EMA predicts the transmission of the MMC most accurately. The filling factor extracted using CSP EMA will be used for subsequent analyses.

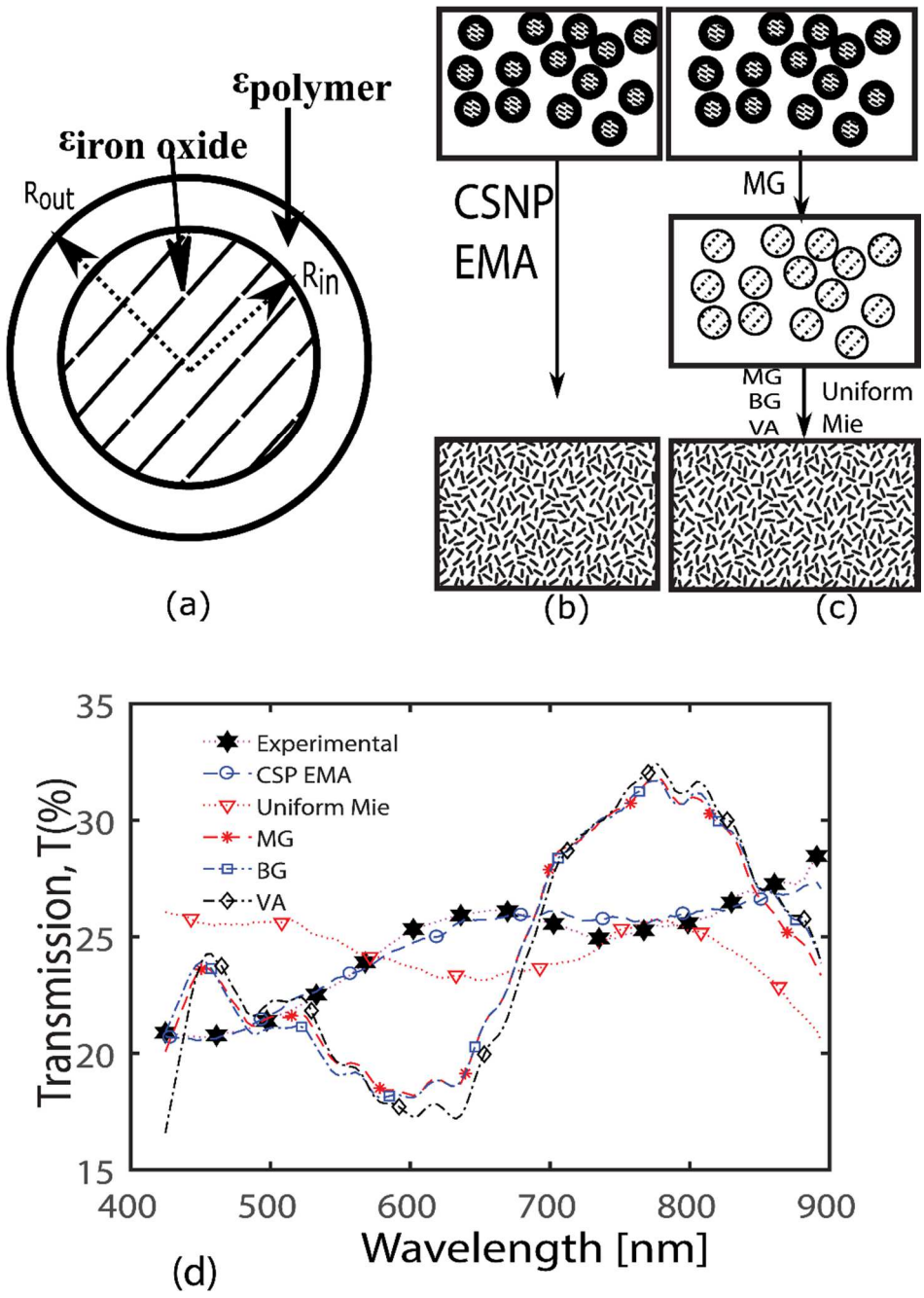

Figure 56 (a) The structure of the magnetic microsphere, (b) the modelling strategy with CSP EMA, and (c) that using several Existing EMAs. (d) Comparison of the experimental and EMA predicted values of transmission. Results obtained using various EMAs are compared to the experimental values.

b) Application: Tunable optical filter

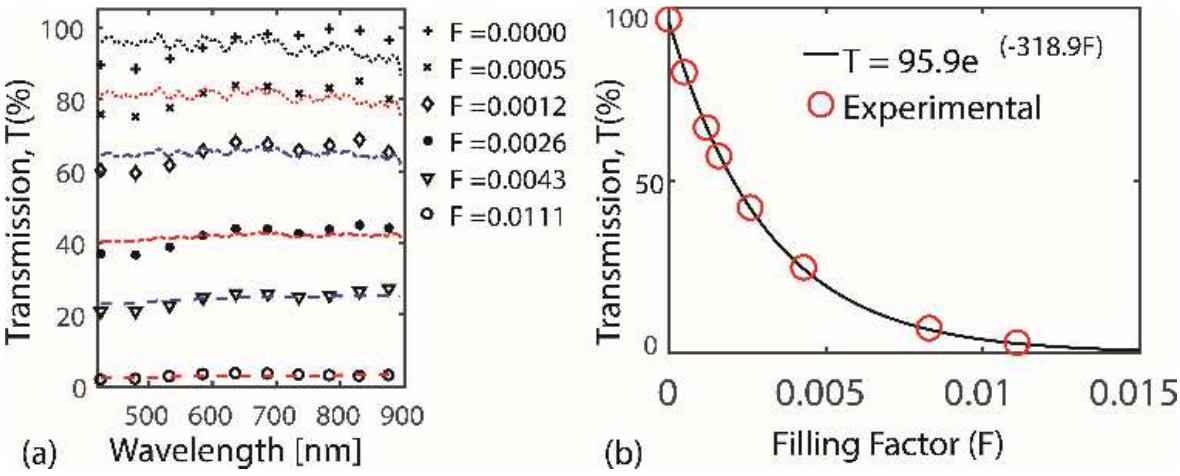

Figure 57 (a) The transmission of the MMC at different filling factor. The lines represent EMA prediction and the markers represent experimental value. (b) The average transmission at different filling factor.

The internal composition of the MMC can be directly related to its refractive index by eq. (3.34). Although most input parameters in (3.34) cannot be changed once the MMC sample is prepared, the filling factor can be changed magnetically. Thus, by changing the filling factor, the transmission of the sample can be controlled. In this section, the relationship between the transmission and filling factor is quantified.

To that end, the transmission of the MMC was experimentally determined at different filling factors. The experimental results and corresponding EMA predictions are shown in Figure 57(a). The filling factors corresponding to each transmission curve are shown at the top right corner. At F = 0.0111, the transmission is close to 0 throughout the spectrum, with local peaks near 700 and 900 nm, indicating the brown color of the sample. As the filling factor decreases, the transmission steadily rises and becomes very close to 100% throughout the visible wavelengths. At lower filling factors, the peaks at 700 and 900 nm are less pronounced, indicating the increasing transparency of the sample. The tunable range of the transmission is therefore close to 100% throughout the visible

spectrum, which indicates the viability of the colloids as a tunable optical window. The spectral average of the experimental transmission for different filling factors is plotted in Figure 57(b). The least error fitting of the experimental data reveals the relation between the filling factor (F) and the transmission (T) in percentage to be an exponential:

$$T(\%) = 95.9e^{-318.9F} \tag{3.40}$$

Thus, the relation between the filling factor and transmission, in (3.40), can be quantified as an exponential, which helps in tuning the transmission precisely by controlling the filling factor.

The transmission of the MMC can be magnetically tuned using the designed EM actuator. When the magnet of the actuator was activated, the magnetic field exerted a magnetophoretic force on the microspheres, which separated them from the colloid. Thus, the filling factor became smaller with the application duration (D) of the actuator. The stirrer of the actuator mixed the separated microspheres back into the colloid and reset the filling factor. In this section, the magnetic field tunability of the transmission was discussed, and the relationships between transmission, magnetic field and duration of application were quantified. The magnetically tunable transmission of the MMC was demonstrated using the EM actuator, and the results are plotted against time in Figure 58(a). When the magnet in the actuator is activated, the transmission (T) increases exponentially with the duration of application (D) as:

$$T(\%) = T_0 e^{\tau D} \tag{3.41}$$

where τ is the exponential coefficient. The value of τ depends on the magnetic field strength.

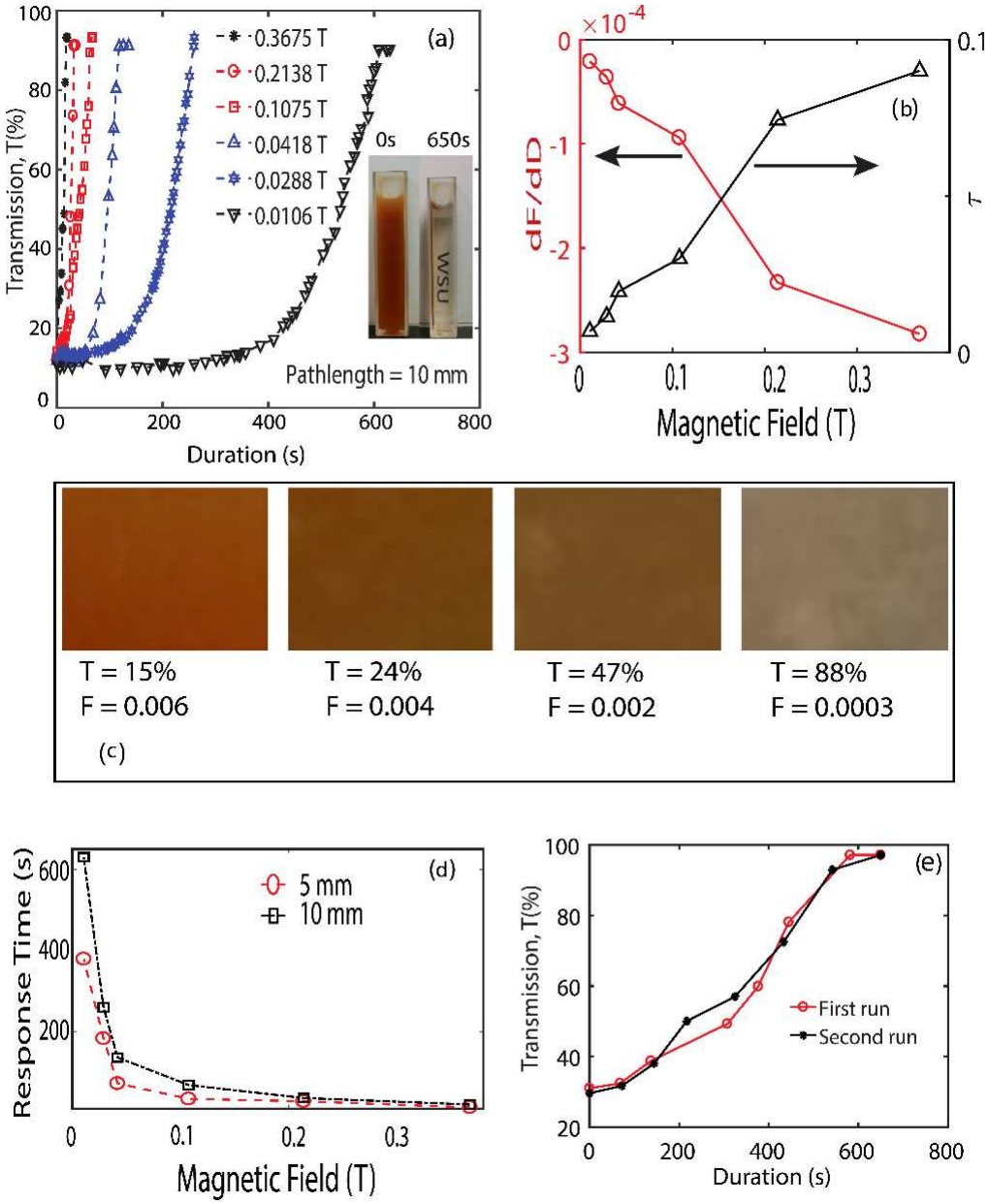

Figure 58 (a)The transmission of the sample under magnetic field is plotted against duration of magnetic field. (b) The rate of filling factor changes, and exponential coefficient of transmission are plotted against magnetic field. (c) Tunable transmission of the colloids. (d) Response time is plotted against field strength. (e) Change in transmission with duration of magnetic field.

In the inset of Figure 58(a), it is shown that a completely opaque sample turned transparent in 650s using the actuator when B = 0.01T. From (3.40) and (3.41), a linear relation can be found between the filling factor (F) and duration (D):

$$\mathrm{F} = \mathrm{C}_1 - C_2 D \tag{3.42}$$

where $\mathrm{C}_1 = \frac{\log(95.9/T_0)}{318.9}$ and $\mathrm{C}_2 = \frac{\tau}{318.9}$ are parameters that depend on the applied magnetic field and nature of the MMC. From (3.42), it is apparent that the filling factor linearly decreases with duration. The filling factor can be reset to the initial value by activating the stirrer in the actuator. The rates of the filling-factor change with respect to the duration (dF/dD) is shown in Figure 58(b). The filling-factor decreases faster with a stronger magnetic field. Similarly, the exponential coefficient of the transmission (τ) increases with the magnetic field, as shown in Figure 58(b), implying a faster change in the transmission with a stronger magnetic field. The quantitative relations between the filling factor, duration, and transmission, as described in (3.40) - (3.42), and the subsequent analyses imply that the transmission of an MMC sample can be controllably tuned by choosing the magnetic field strength and duration. To illustrate this, an MMC sample is subjected to a magnetic field 0.0418 T. The sample was placed in the magnetic field for a certain amount of time before removing the magnetic field. After capturing a photo of the sample and resetting the MMC, the experiment was repeated with increasing duration. In Figure 58(c), pictures of the samples are shown. As the duration of the magnetic field increases, the filling factor and transmission of the sample decreases from 15% to 88%. Thus, different transmissions can be obtained using the same sample simply by changing the duration of the magnetic field. As implied in (3.42), the speed of the tuning is dependent on the magnetic field strength.

In Figure 58(d), the response time of the sample, defined as the time required to achieve transparency of the MMC, is plotted against the magnetic field. As expected, the response time falls sharply as the magnetic field strength increases. Also, the same

magnetic field has a faster response time for the 5mm cuvette compared to the 10-mm cuvette. Thus, the transmission of the MMC can be tuned using the application time and magnetic field strength of the EM actuator along with optical pathlength as tunable parameters.

The magnet and stirrer in the actuator allowed us to repeatedly decrease and reset the filling factor. Thus, the tuning of the transmission can be done repeatedly. To investigate the reproducibility of the tuning process upon repetition, we investigated two successive cycles of tuning using the same magnetic field strength. The results are summarized in Figure 58(e). The transmission changes almost identically with duration for both cases, indicating the high reproducibility of the tunability.

Magnetic microsphere colloids, along with a compact catch and release system, has the potential to be a fast, stable, and inexpensive tunable optical window or switch. Several miniature catch and release systems have been reported, including current carrying conductors, differential magnetic fields, and permanent magnets.

3. LOSSY NANORODS AS ABSORBER

To observe the performance of the EMA with lossy materials, we studied the absorption in lossy mesoporous alumina with cylindrical air inclusions on an aluminum substrate [100] as shown in Figure 59. We calculated the absorption of the multilayered structure using all the EMAs mentioned in this work, as seen in Figure 59. In this case, the matrix material was lossy alumina, and the inclusion material was air. In this case, however, the inclusions were cylindrical in shape.

Although we have assumed that air inclusions are spherical in shape as opposed to cylindrical, it can be observed that the Mie and Rayleigh models produce very good

matches to the experimental results. It implies the suitability of the proposed models even when the constituents are not spherical in shape. To understand the cause of this, we calculated the scattering cross section (SCS) of spherical and cylindrical shaped inclusions with equal volume. The results are plotted in the inset of Figure 59. We see that the polarizabilities of the cylindrical inclusion and spherical inclusion are good approximations of each other.

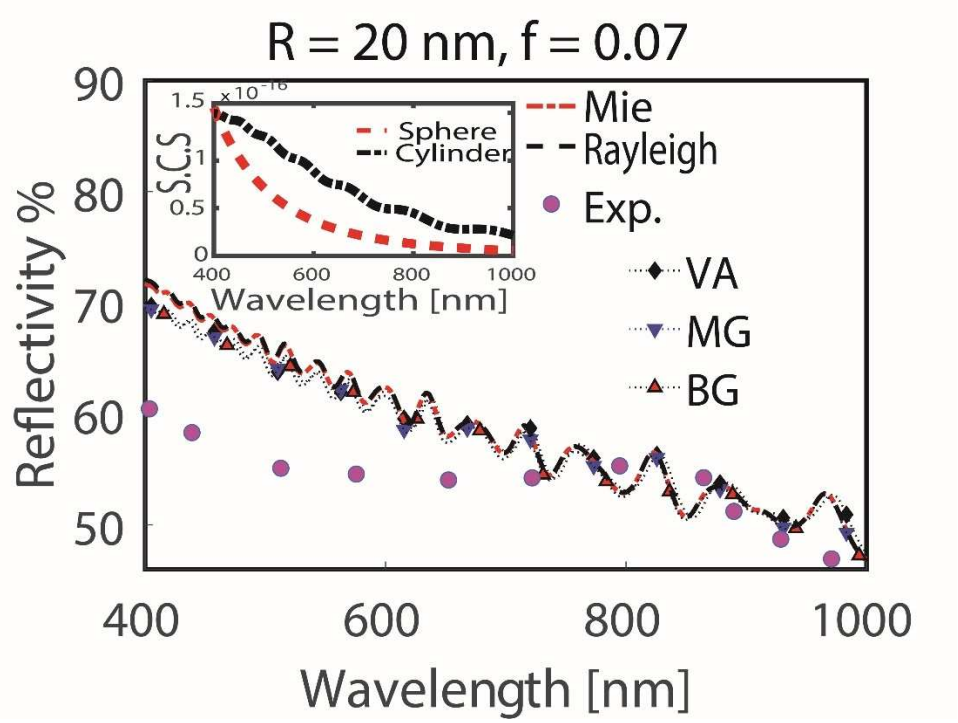

Figure 59 The absorption by mesoporous alumina on aluminum substrate is calculated using EMA and compared to experimental result [100]. The SCS of cylindrical and spherical inclusions with equal volume are compared in the inset.

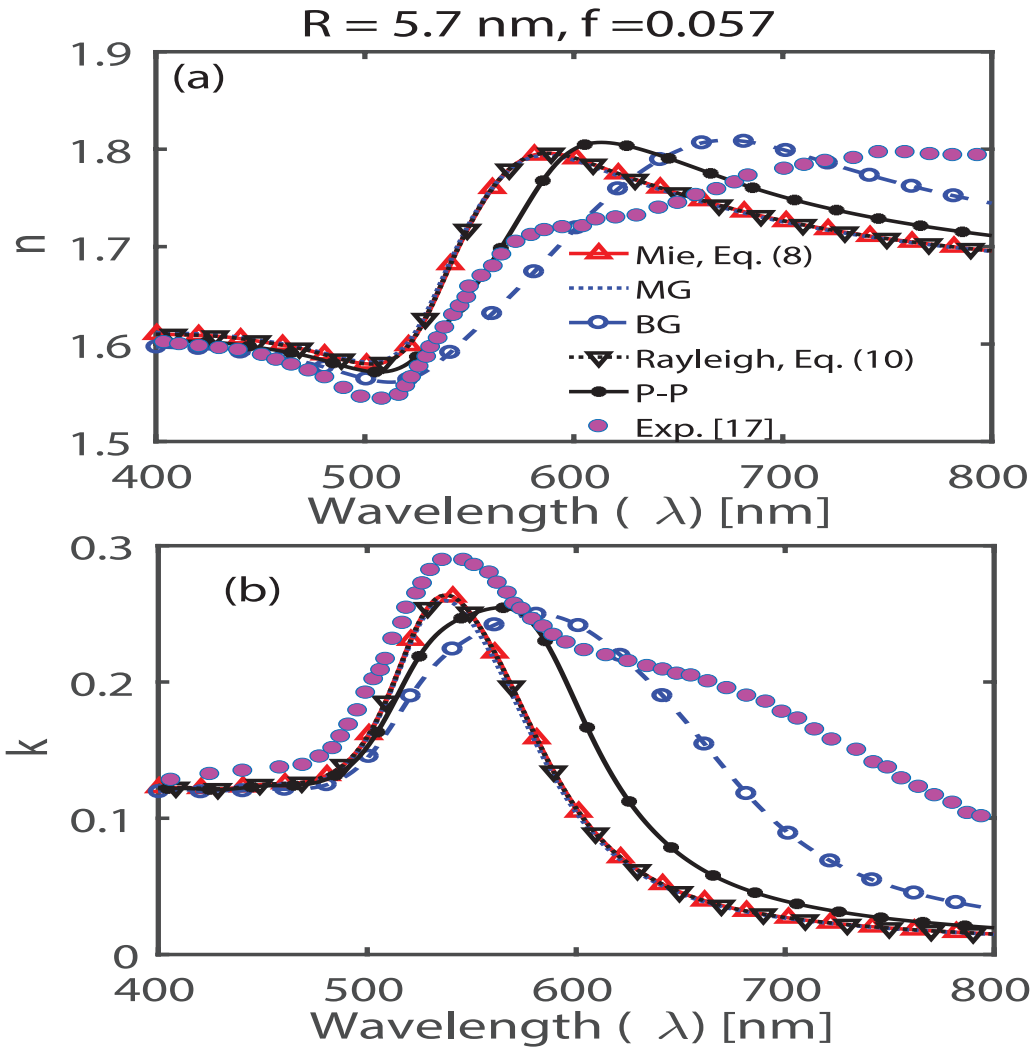

Figure 60 The effective complex refractive index of gold nanoparticles suspended in PVK.

Another case we investigated is when the inclusion material is plasmonic, e.g., gold. The effective parameters of gold nanoparticle colloid in PVK (Polyvinyl Carbazole) polymer has been estimated using ellipsometry [146]. The EMA predictions are compared with experimental results in Figure 60. The nanoparticle radius was 5 nm, and the filling factor was ~5%. We compare the experimental data with those calculated using EMA. The Mie and Rayleigh models show some clear deviance from experimental result in this case. It is caused by the interparticle interaction. When the net polarizability is used in the Mie EMA, improved predictions are found. The black dash-dotted line in Figure 60

represents the result when the net polarizability is used. When interparticle interaction is modelled, the Mie model produces a much closer fit. Evidently, the Mie model is not only the most accurate among the models, but also the most complex as well. The Rayleigh approximation produces a sufficiently close approximation to the Mie model in a much simpler way. The linear models aren't shown in this case because they completely fail.

E. Summary

In conclusion, we have derived an effective medium approximation that accounts for the Mie and Rayleigh scattering within the frameworks of Maxwell-Garnett's mixing rule with a simpler and analytical expression. We have compared the results derived from this expression with experimental results and found better agreement compared to other EMAs reported in the literature. We found that most models can accurately model media with small inclusion, but for media with a larger inclusion size and a higher filling factor, the derived formula produces the best match. The derived formulae are shown to be more accurate than other EMA formula for lossy and plasmonic material. Their accuracy for the cases when the inclusions are cylindrical in shape were also tested. Inter-particle interaction, which is absent from most EMAs, has been accounted for in our model using multipole net polarizability, which improves the accuracy of the formulae in predicting the optical properties of aperiodic optical nanostructure.

To demonstrate the flexibility of size in the derived framework, a magnetic colloid is modelled which contained particle that are comparable to wavelength in size. It was found that the transmission through the colloid can be successfully predicted, and the magnetic tunability can be calculated using the derived formulae.

IV. FLAT OPTICAL ELEMENTS COMPOSED OF APERIODIC NANOSTRUCTURE

In previous chapters, analytical techniques to analyze optical nanostructures were studied and developed. A more accurate and versatile analytical framework for studying aperiodic optical nanostructure was established. Various devices were demonstrated analytically and experimentally using these methods. In this chapter, we further develop the analytical framework. Here, we develop a method to analytically calculate the far-field created by an aperiodic optical nanostructure. Our focus is on the design and analysis of flat optical elements composed of subwavelength aperiodic optical nanostructures. Flat optical elements are highly desirable because they are compatible with planar integrated circuit technology. Unlike traditional optics, where the shape of bulky spheroids must be carefully designed to obtain high-performance optical elements, flat optics promise flat, ultra-thin optical components with subwavelength phase control, single step lithography and superior aberration control [147]. Here, we demonstrate how the developed analytical framework can be harnessed to design and analyze flat optical elements using subwavelength nanostructures. Then, we compare the analytical method with numerical methods and compare their efficiency. Using the analytical method, we point out the role of low refractive index material in designing low-loss, flat subwavelength optical elements.

In this chapter, we investigated the performance of flat optical lenses designed using typical optical glass, utilizing the analytical Fresnel or Rayleigh-Sommerfeld (RS) diffraction theory in combination with analytical effective medium approximation (EMA), along with the full wave three-dimensional finite difference time domain method (3D-FDTD). First, the relationship between geometric parameters of inclusions and the produced phase is investigated. The condition on the size and shape of the inclusions to

achieve complete 2π phase coverage is determined. Then, the spatial phase profile for focusing a plane wave is designed using inclusions of different shape. Analytical and numerical analyses of the performance of the optical lenses were carried out and the results were compared. The analytical method, despite requiring significantly lower computational resources, accurately matched FDTD and experimental results. The memory efficiency of the analytical method allowed for the analysis of large scale thin optical lenses with subwavelength structures. Although the design methodology presented here is independent of the wavelength, we report specifically on visible wavelengths and perform our calculations at λ=600 nm. The results indicate that robust, polarization insensitive subwavelength optical lenses can be designed using low index materials like glass using highly efficient analytical methods.

A. Methodology

1. PHASE CALCULATION

All-dielectric nanostructured optical lenses can be designed by implementing spatial phase profiles using inclusions that produce a specific phase [88, 96, 148, 149]. Thus, the first step in designing such optical lenses is to relate the inclusions with a specific imparted phase. The origin of the produced phase can be overlapping resonances in dielectric resonators [149-151], geometric phase [85], and propagation phase [152, 153]. One advantage of using a low refractive index material is that the phase relation can be easily calculated using EMA since only the propagation phase is relevant in this case. In this section, we study low index inclusions of various shape using EMA [77, 154-156] and compare the results with FDTD calculations.

In Figure 61(a), the different shaped inclusions are shown. The shapes include rectangular fins of fixed height, cubes with varying side length, cylinders with varying radius and height, planar cylinder with fixed height and varying radius, and spheres with varying radius. The inclusions are assumed to be low index material on a low index substrate. We assume the inclusions are arranged periodically with a period of (*a*) 400nm. The height of the inclusions is specified by H, while R specifies the size. R represents the radius for the sphere shaped and cylinder-shaped inclusions. For the cube and fin shaped inclusion, both lateral widths can be given as 2R. The relationship between the height and size is shown in Figure 61(a). In this calculation, we assume the operating wavelength to be 600 nm.

The 3D-FDTD calculations are carried out using commercially available FDTD and post-processing tools. Bloch boundary conditions have been used in-plane, whereas a perfectly matched layer (PML) boundary is used along the propagation direction. A convergence test was carried out to find an appropriate mesh density. A plane wave of 600nm wavelength impinges on the inclusions with normal incidence, and the transmitted fields are calculated. From the source and the transmitted fields, the complex transmission from the inclusions is calculated. The phase of the transmission is also calculated using EMA. From Figure 52, the simplest approximation is enough when the refractive index is low (<2.0). While many different EMA formulas are available, we choose the volume averaging [77] formula. Here, the only phase considered is the propagation phase, given as:

$$\phi_{\mathrm{prop}} = \frac{2\pi n_{\mathrm{eff}} H}{\lambda} \tag{4.1}$$

Where $n_{eff} = \sqrt{n_s^2 FF + 1 - FF}$ is the volume averaged effective index of the arrayed inclusions of different shape, n_s is the inclusion refractive index and FF is the volume filling factor of the medium. As the size (R) changes, the FF changes, leading to change in n_{eff}. The change in n_{eff}, along with the change in H, causes the change in ϕ_{prop}.

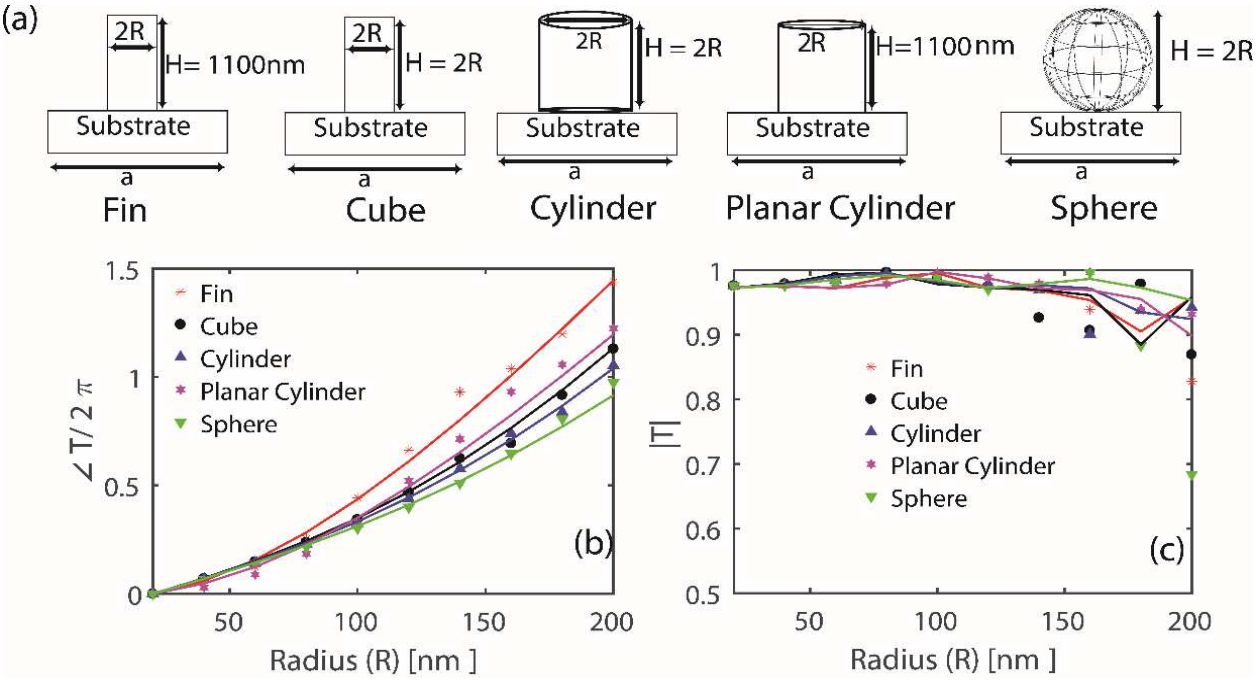

Figure 61 (a) the low index inclusions with different shapes on glass substrate. The phase(b) and transmission (c) of the transmission through the arrayed inclusions. The markers represent FDTD calculations while the solid lines represent EMA predictions.

In Figure 61(b), the 2π normalized phase angle of transmission ($\angle T/2\pi$) through the arrayed inclusions of different shapes are shown as the size (R) increases from 20 to 200 nm. The FDTD calculations, represented by the markers, is closely matched by the EMA predictions (ϕ_{prop}), represented by solid lines. Thus, we can conclude that the propagation phase is the dominant source of the phase in this case, and the shape of the inclusion is not important. This argument is bolstered further by Figure 61(c), where the magnitude of transmission for different shapes also shows agreement between EMA and

FDTD results. Thus, EMA calculations can be used to draw relationship between produced phase and the size of inclusions, which significantly simplifies the design process. Additionally, using EMA allows us to analytically derive the conditions for achieving 2 π phase coverage:

$$2\pi = \phi_{max}(R,H) - \phi_{min}(R,H) \tag{4.2}$$

where φ_{max} is the maximum phase, φ_{min} is the minimum phase. From (4.1), the maximum phase is imparted when the product $n_{eff}H$ is maximum, and the phase is minimum when $n_{eff}H$ is minimum. Thus, the condition in (4.2) can be simplified as:

$$n_{eff_{max}}(R,H)H_{max} - n_{eff_{min}}(R,H)H_{min} = \lambda \tag{4.3}$$

Here, H_{max} is the maximum height, $n_{eff_{max}}$ is the maximum effective index, H_{min}in the minimum height, and $n_{eff_{min}}$ is the minimum effective index. The relations in (4.3) can be used as a guideline to determine the required R and H to achieve 2π phase coverage. For example, let us consider the inclusions shown in Figure 61(a). For the spheres, cubes, and cylinders, the span of the parameter R can be calculated from (4.3) by substituting H = 2R, while for the planar cylinders and fins, $H_{max} = H_{min} = H$. The relationship between R_{max} and R_{min} for the sphere, cube and cylinder-shaped inclusion is shown in Figure 62(a). The cubic shape requires the smallest span of R while the sphere shape requires the highest. This agrees with the fact that cubes can be packed much more closely and medium with cubic inclusions can have a higher effective index compared to cylindrical and spherical inclusions. For the planar cylinder and fin shaped inclusion, a minimum H required to obtain the 2π phase coverage[152], given as $\mathrm{H} = \lambda/(\mathrm{n_s} - 1)$, which is 750 nm in this case. The relationship between H and the span of R is plotted in Figure 62(b)

and (c) for planar cylinder and fin shaped inclusions, respectively. The required span of R decreases with increasing H.

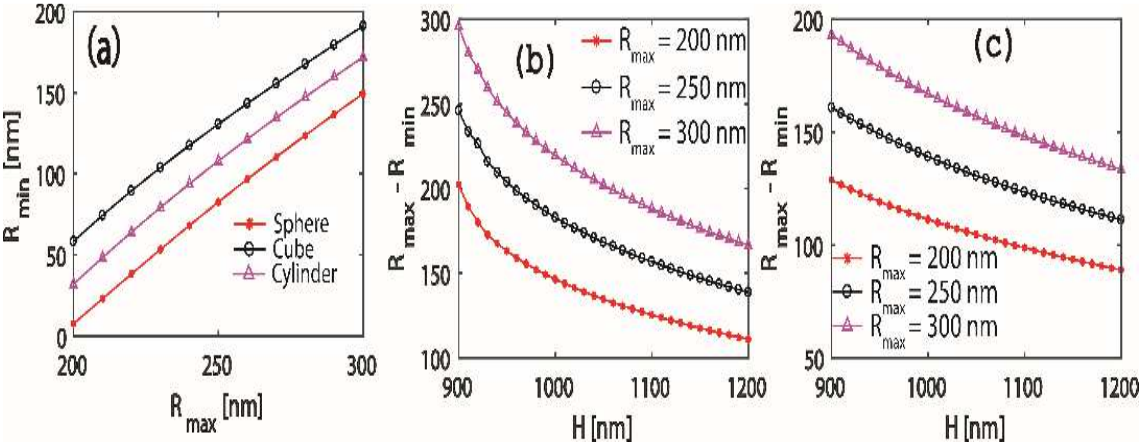

Figure 62(a) The relationship between Rmin and Rmax for the sphere, cube, and cylinder-shaped inclusion. (b) The relation between the span of R and H for planar cylinder and (c) fin shaped inclusion.

Using the relations shown in Figure 62, it is possible to determine the necessary design parameters for optical lenses. While the calculations are carried out using $n_s = 1.8$, the methodology employed remains valid when the propagation phase is the dominant phase.

2. DESIGN OF OPTICAL COMPONENTS

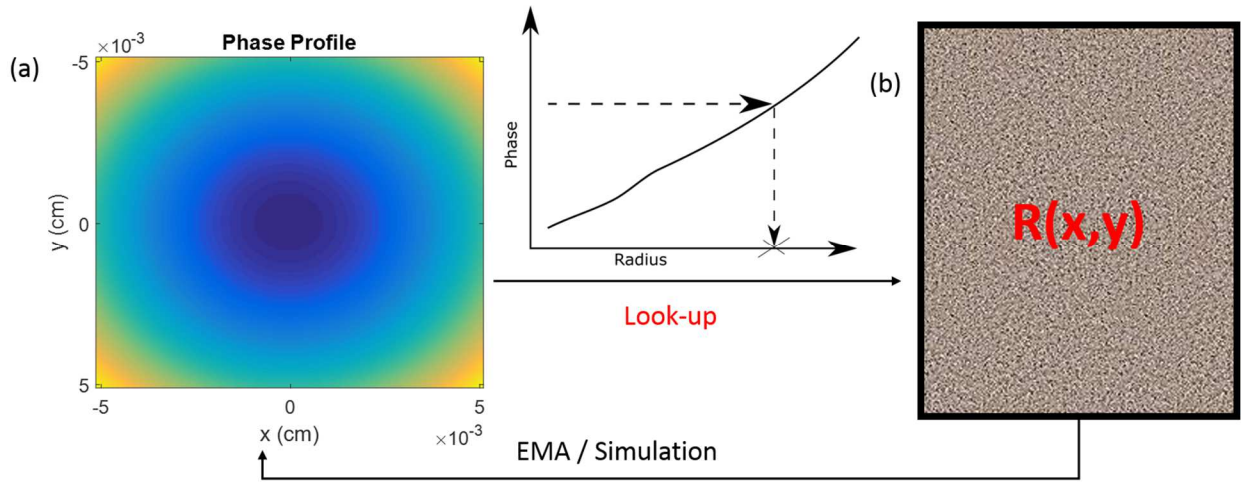

Figure 63 The process of calculating the physical structure of the optical element from the required phase profile

In this section, we design a focusing optical lens by implementing a spatial phase profile, $\Phi(\mathrm{x},\mathrm{y})$ using appropriate distribution of the inclusions to obtain the focusing effect. The spatial phase profile for focusing can be described as:

$$\Phi(x,y) = \frac{2\pi}{\lambda}\left(\sqrt{x^2+y^2+f^2} - f\right), \tag{4.4}$$

where f is the focal length, λ is the operational wavelength and (x, y) are the in-plane spatial coordinates. A sample phase profile is shown in Figure 63(a). To implement the spatial phase profile, it is first discretized into grids that adhere to the Nyquist criterion [89]:

$$a < \frac{\lambda}{2NA} = \frac{\lambda}{2\sin\left(tan^{-1}\left(\frac{D}{2f}\right)\right)} \tag{4.5}$$

where *a* is the periodicity of the grid, NA is the numerical aperture, D is the diameter of the lens, and f is the focal length. In our design, the wavelength is set at 600nm and the periodicity is set at 400nm. Thus, the maximum NA in our system that doesn't violate the

Nyquist requirement is 0.75. The diameter is selected based on available computational resources. In this section, we select *D =51a,* resulting in a lens which is 20.4 μm in diameter. The focal length is selected based on the NA. In this calculation, we choose NA = 0.4. In selecting the periodicity (*a*), care must be taken such that $\mathrm{R}_{\max} = \frac{a}{2}$ is enough to obtain 2π phase coverage. The specific lattice of the grid is not significant. Once the periodicity (*a*) and diameter (D) are selected, the lens surface can be divided into a discretized grid, consisting of $\frac{D}{a} \times \frac{D}{a}$ grid points. From this grid, the discretized phase profile at each grid point can be calculated using (4.4).

Once the discretized phase profile is calculated, the required parameters of the inclusions can be calculated for each grid-point by using the data in Figure 61(b) as a look up table. For example, if the optical element consists of cubic inclusions, then the required R can be looked up using Figure 61(b) as a look-up table for each grid-point. At the end, the distribution R (x, y) required to implement the spatial phase profile $\Phi(\mathrm{x},\mathrm{y})$ can be obtained. This process is schematically represented in Figure 63.

3. FAR-FIELD CALCULATION

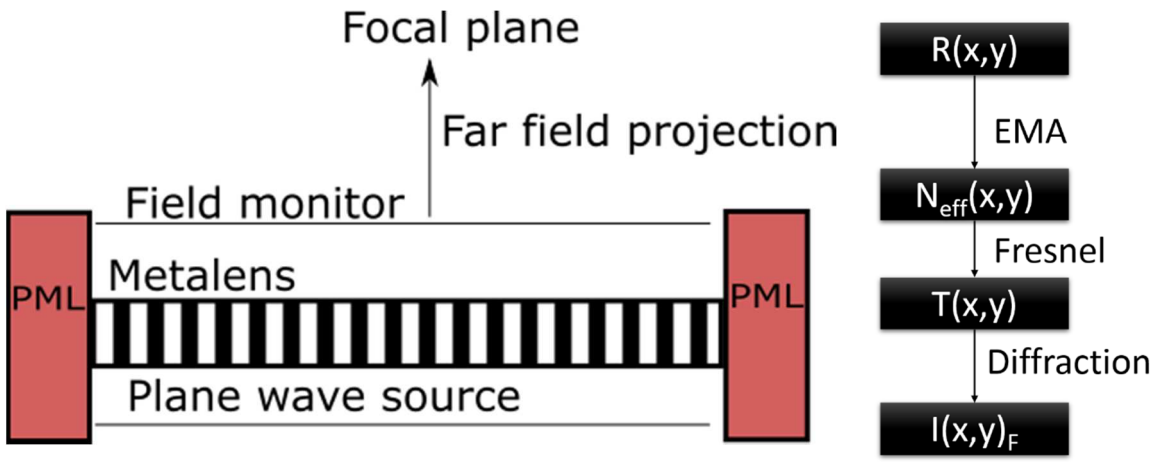

(a) (b)

Figure 64 (a) Using FDTD to calculate the far-field, (b) using analytical scalar diffraction equations to calculate the far-field.

Once the discretized phase profile is calculated, the focal length can be calculated in two different ways, as shown in Figure 64. In FDTD calculations, shown in Figure 64(a), the lens is designed by putting appropriate inclusions corresponding to the required phase at each of the grid-points. Symmetric and anti-symmetric boundary was used along the x and y axes, respectively. The boundary along the propagation axis (z) was PML. By illuminating the designed lens by a 600 nm wavelength plane wave, the near fields at the edge of the optical lens can be extracted. By converting the near-fields into a far-field along the focal axis, the focal length can be calculated.

As shown in Figure 64(b), we also utilize an analytical diffraction equation [157] with EMA to calculate the focal length. In this method, the effective refractive index at each grid point is calculated using the relation:

$$n_{eff}(x,y) = \Phi(x,y) \times \frac{\lambda}{2\pi H(x,y)}. \tag{4.6}$$

Here, $\mathrm{n_{eff}}(x, y)$ is the volume averaged effective index and H is the height of the nanostructure at the specific grid point. The averaging window was set equal to the period (*a*). Using the obtained n_{eff}, the magnitude of the transmission can be analytically calculated using a well-known formula for layered media, and the phase of the transmission can be calculated using (4.1). From the calculated complex transmission of the optical lens, the intensity along the focal axis can be calculated using the analytical diffraction equation. There are several analytical solutions to the diffraction problem that can be used, depending on the numerical aperture of the lens. For example, if the numerical aperture is large, the Rayleigh-Sommerfeld (RS) equation needs to be used. When the numerical aperture is small, we can use the Fresnel diffraction equation. Using the RS equation, the far-field at a distance z can be calculated as:

$$U_{farfield}(x,y) = F^{-1}\left(F\left(U_{near}(x,y)\right) \times F\left(\frac{z}{j\lambda}\left(\frac{\exp\left(jk\sqrt{z^2+x^2+y^2}\right)}{z^2+x^2+y^2}\right)\right)\right) \qquad (4.7)$$

Similarly, the far-field at a distance z can be calculated using the Fresnel equation as:

$$U_{farfield}(x,y) = F^{-1}\left(F\left(U_{near}(x,y)\right) \times F\left(\frac{e^{jkz}}{j\lambda z}\frac{jk}{2z}(x^2+y^2)\right)\right) \qquad (4.8)$$

Here,

$U_{far-field}$	is Far-field distribution
U_{near}	is Near-field distribution
F	is Fourier Transform
F^{-1}	is Inverse Fourier Transform

x, y, z is Distance in the far-field from the center of the lens.

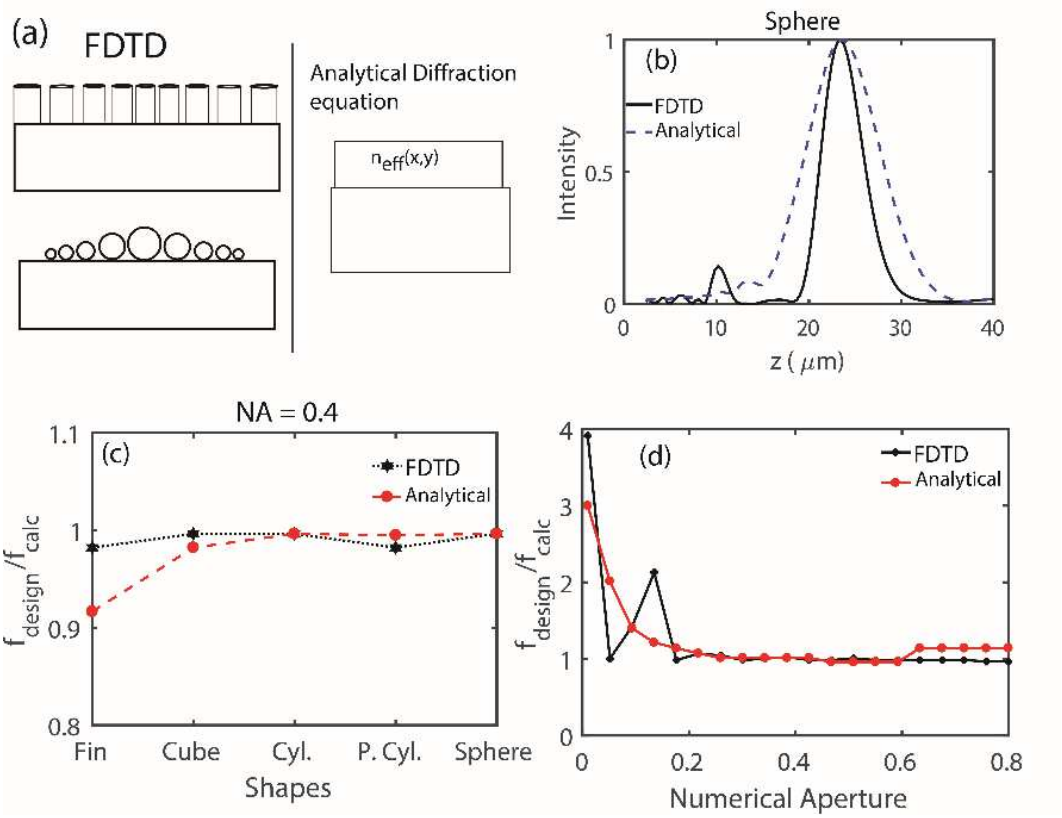

Figure 65 (a) Schematic of the comparison study. (b) The intensity of fields along the focal axis (z) calculated using FDTD and analytical method. The ratio of designed focal length and that calculated using FDTD and analytical method for (c) different shaped inclusions and (d) different numerical aperture.

It is critical to verify that the optical lens has an accurate focal length. In this section we compare the focal length calculation using FDTD and the analytical diffraction formula, as shown in Figure 65(a). The Fresnel diffraction equation (4.8) is used when the numerical aperture (NA) is smaller than 0.1, and the RS equation (4.7) is used in other cases. For this calculation, we assume the direction of propagation is along the z axis while the lens is along the x-y plane.

In Figure 65(b), the intensity of fields along the focal axis, calculated using FDTD and analytical method, is plotted. Both FDTD and RS calculation predict focusing at the same focal length and show similar intensity profile. We performed this study for the inclusion shapes shown in Figure 61(a) and summarized the result in Figure 65(c). At NA = 0.4, the accuracy of FDTD and analytical method in predicting the design focal length is independent of inclusion shape and remains comparable to each other. However, as NA changes, the accuracy of predicting the design focal length worsens for both methods, as shown in Figure 65(d). At a very small NA, the far field projection done in the FDTD calculation degrades in accuracy, and the predicted focal length is smaller than the actual design focal length. The analytical method also shows a similar degradation of the accuracy. On the other hand, for a higher NA, both FDTD and the RS method predict the focal length with high accuracy. Thus, EMA along with the analytical diffraction equation can characterize nanostructured optical lenses as accurately as FDTD methods using significantly lower computational resources.

A summary of the methodology steps is shown in Figure 66.

A. Comparison with FDTD

To compare the focusing properties of the lens calculated using FDTD and the analytical method, we analyze two optical lenses using both methods. With no loss of generality, we consider lenses consisting of spherical and cylindrical inclusions.

Figure 67 (a) shows the partial schematic of the first optical lens, with NA = 0.4 and a design focal length of 23 □m. It consists of spherical inclusions (n_s = 1.8) arranged in a hexagonal lattice with periodicity 400 nm on a glass substrate (n_{sub} = 1.4). The radius of the spheres varies between 20 nm to 200nm. The device is illuminated from below by a

monochromatic plane wave with $\lambda = 600\text{nm}$.The intensity of the electromagnetic fields at the focal plane can be seen in Figure 67(b). Clearly, the plane wave is focused on to a

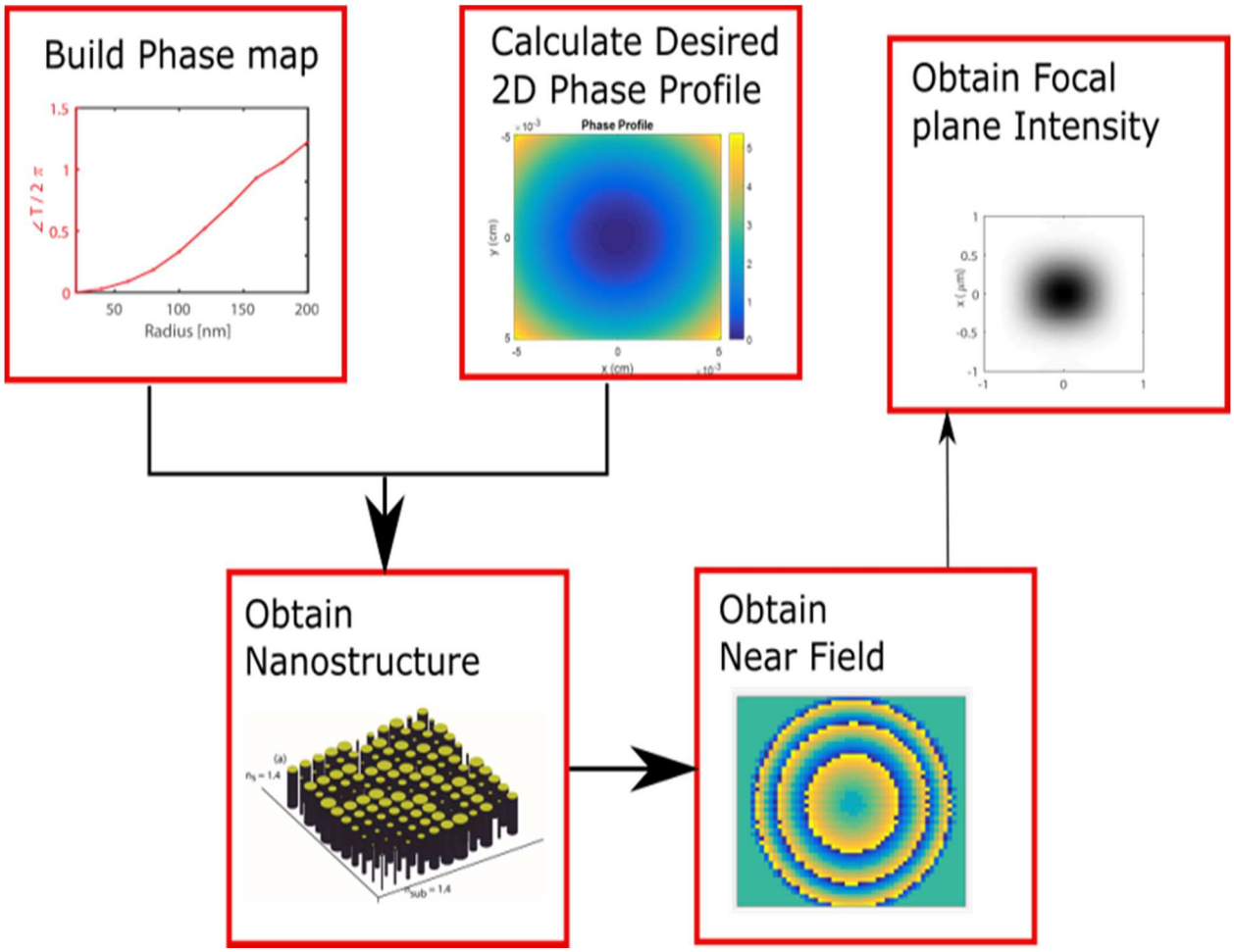

Figure 66 A summary of the methodology.

single spot. The intensity of the electric field along the (y = 0) and (x = 0) line in the focal plane has been calculated using FDTD and the analytical method, and the results are summarized Figure 67(c) and (d), respectively. The analytical predictions are in close agreement with the FDTD results. Both methods predict Airy profiles with multipole lobes. The main lobe is approximated by a Gaussian curve to determine the spot size. The FDTD calculation predicts a spot size of 0.31 □m while the analytical method predicts spot size of 0.34 □m, both of which compare well with the diffraction limit (0.2 □m) in this case.

Figure 67(e) shows the intensity along the focal axis, which shows that both methods predict the focal length accurately. We calculated the focusing efficiency by comparing the power in an area with a radius of 2*spot size with the total power in the focal plane. In this case, the focusing efficiency is 20%.

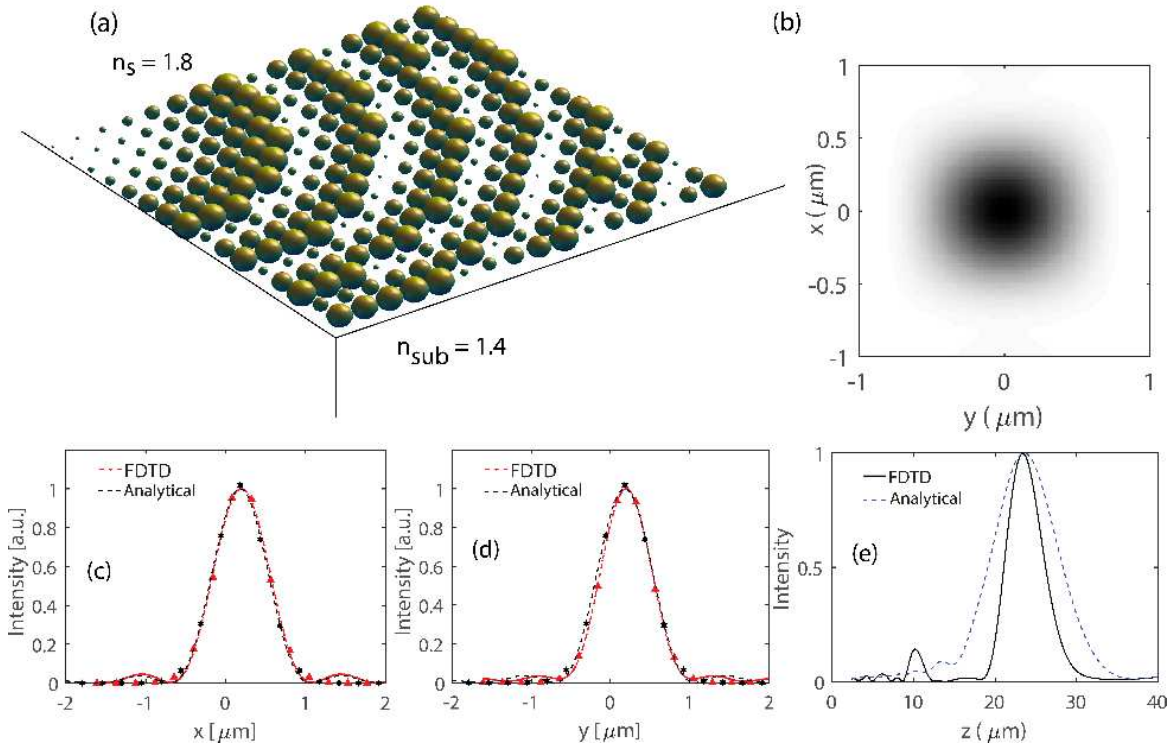

Figure 67(a) Schematic of spherical inclusions on glass substrate. (b) The intensity profile at the focal plane where z = f. The intensity profiles in the focal plane calculated using FDTD and analytical method along the (c) x, (d) y, and (e) z axis. The stars (*) represent the Gaussian fit for the FDTD results and the triangle (Δ) represent the Gaussian fit for the analytical method results.

A similar analysis is carried out for a second optical lens, consisting of a cylindrical inclusion (n_s = 1.4) with a fixed height (H = 2000 nm) arranged in a rectangular lattice with periodicity 400 nm on a glass substrate (n_{sub} = 1.4). Figure 68(a) shows a partial schematic of the optical lens. Like the previous case, the lens has NA = 0.4, and the design focal length is 23 □m. In Figure 68(b), the incident light is focused on a spot in the

focal plane. The spot size at the focal plane is calculated using FDTD and the analytical method, and the results are 0.29 □m and 0.21 □m, respectively. The focusing efficiency is found to be 18.5% in this case. Based on the above analyses, the analytical method is capable of closely matching the FDTD prediction.

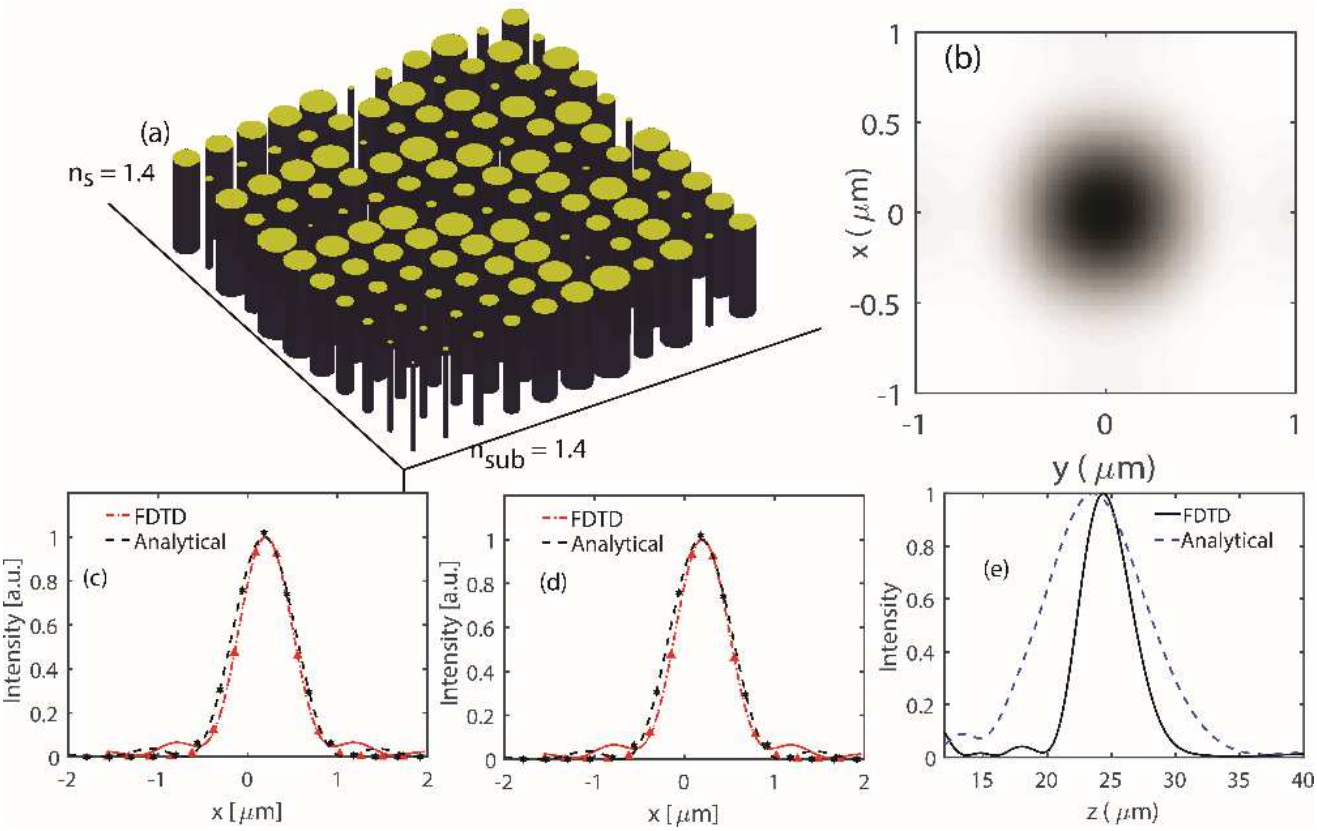

Figure 68(a) Schematic of the cylindrical inclusions on glass substrate. (b) The intensity profile at the focal plane where z = f. The intensity profiles in the focal plane calculated using FDTD and analytical method along the (c) x, (d) y, and (e) z axis. The stars (*) represent the Gaussian fit for the FDTD results and the triangle (Δ) represent the Gaussian fit for the analytical method results.

In Table 14, the focusing performance of this optical lens is compared with other reported devices operating in visible wavelengths. The performance of the designed lens compares well with the reported devices operating in the visible wavelengths. The calculated spot size is comparable to those reported using high index material. The efficiency also agrees well with the reported values using comparable materials. The low

efficiency can be attributed to the inability of low index inclusion to diffract light into higher orders efficiently[158]. Notably, such performance has been achieved with a subwavelength thickness.

Table 14 Comparison of the performance of the designed flat lens.

INDEX (N)	THICKNESS (NM)	NA	EFFICIENCY	SPOT SIZE	REFERENCE
2.17	245	0.15-0.2		2.8 □m	[95]
2.0	633	0.75	10%	0.95 □m	[84]
2.0	633	0.06	47%	15 □m	[84]
1.52	<1200	0.5		1.55 □m	[96]
2.6	<600	0.6	70%	0.46 □m	[89]
1.56		0.17	15-20%		[159]
1.8	<400	0.4	20 %	0.3 □m	This work
1.4	2000	0.4	18.5%	0.29	

B. Comparison with the Experiment

In this previous section, it was established that a combination of EMA and the diffraction equation can predict the focusing properties of a subwavelength nanostructured optical lens. In this section, we compare the analytical predictions with experimental work from the literature.

First, a high refractive index transmit-array based lens[160] is considered. It is composed of high index (n_s = 3.43) cylindrical inclusions with a fixed height (H = 900 nm), arranged in a rectangular lattice with periodicity 800 nm. The structure is like Figure 68(a). The radius of the inclusions varies between 100 nm to 300 nm. The operating wavelength was 1550 nm. The intensity of electric field along the focal axis of the lens is calculated using analytical method and the results are summarized in Figure 69(a). The dotted line represents experimentally measured focal length. Clearly, the analytical method can predict the focal length accurately.

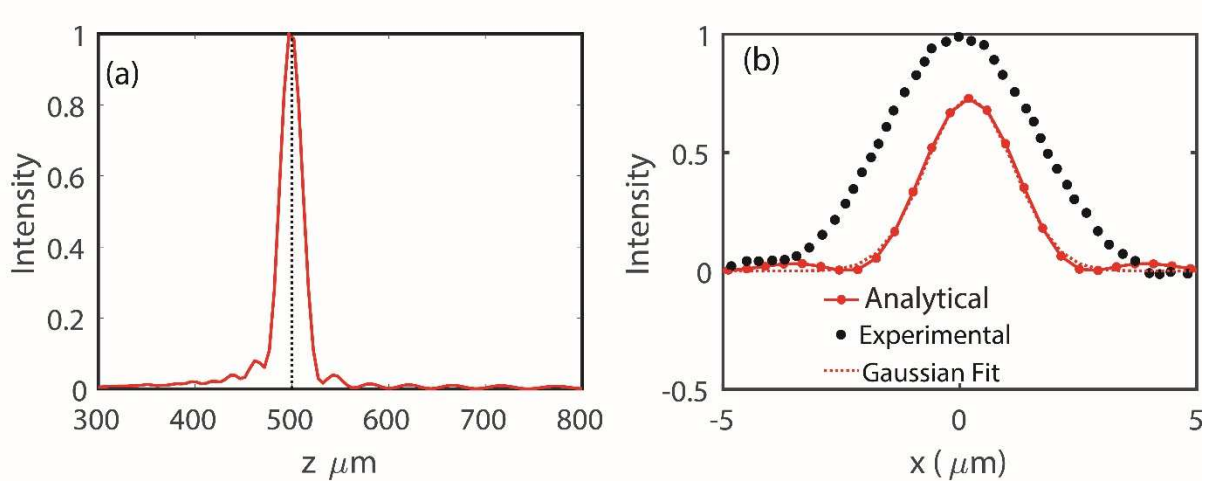

Figure 69(a) The intensity along the focal plane of the high refractive index lens. The dotted line represents the design focal length. (b) The experimental intensity along the x axis, approximation using analytical method and its Gaussian fit.

In Figure 69(b), the experimentally measured intensity profile along the x axis, taken from [160] is compared with analytical results and its Gaussian fit. The analytical calculation closely matches the intensity profile. Thus, the analytical method can accurately predict focusing performance even when the inclusions have a high refractive index.

A similar comparison is carried out for a low refractive index lens (n_s = 2.0) composed of cylindrical inclusions with fixed height (H = 633), arranged in a rectangular lattice with periodicity 443 nm [84]. The radius of the inclusions was between 20 to 220 nm while the operating wavelength was 633 nm. The structure of the lens is like that in Figure 68(a).

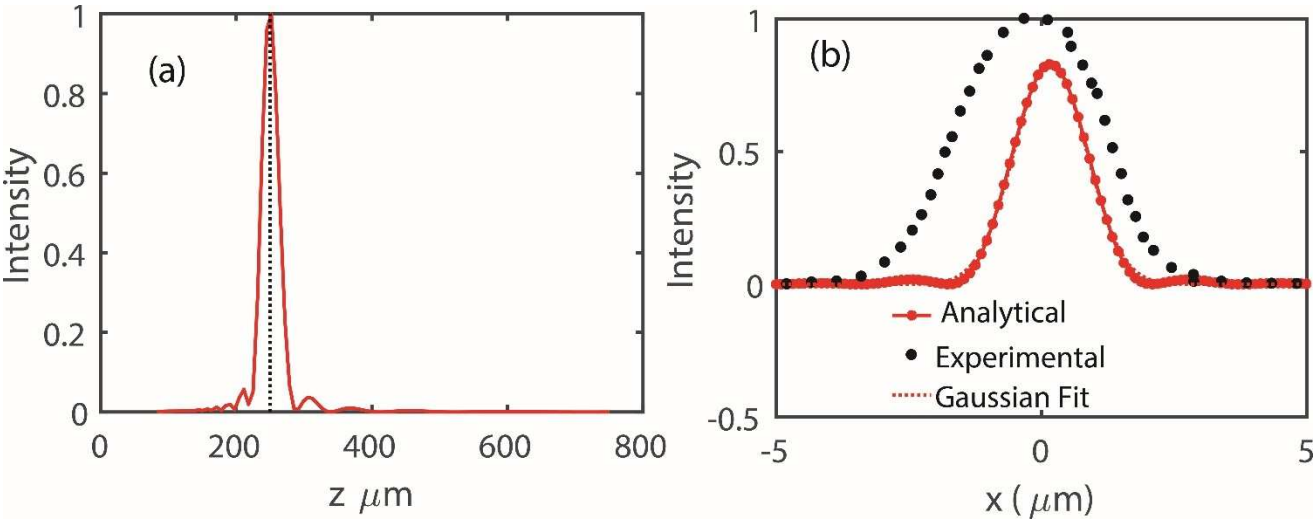

Figure 70(a) The intensity along the focal plane of the low refractive index lens. The dotted line represents the design focal length. (b) The experimental intensity along the x axis, approximation using analytical method and its Gaussian fit.

In Figure 70(a), the intensity along the focal axis, calculated using analytical method, is plotted. The dotted line represents experimentally measured focal length. Clearly, this method predicts the design focal length accurately. In Figure 70(b), the experimentally measured intensity along the x axis is plotted along with analytical calculation and its Gaussian fit. In this case, the experimental intensity profile is wider than the EMA prediction. The EMA calculation predicts the ideal Airy spot of the designed lens where the phase profile is perfectly implemented and the focusing is only diffraction limited. Experimental measurement has other limitations related to imaging and measurement, resulting in a wider spot.

Thus, the analytical approach, based on diffraction equation and EMA, is a suitable tool for studying optical lenses, even when the inclusions have a high refractive index.

C. Large Area Focusing Lens

1. FOCUSING

In the FDTD analysis presented previously, the size of the analyzed lens was limited by high memory requirement of the FDTD method. For a practical lens with a millimeter range size, the optical lens would require more than 16 million individual inclusions. The FDTD analysis of such a structure may require terabytes of memory, which is prohibitively large. Algorithms have been developed to reduce the memory required to manufacture such lenses[161]. The numerical analysis of such large lenses is a necessary step before fabrication. Clearly mesh-based methods like FDTD or FEM would require a prohibitive amount of memory when simulating millions of individual inclusions. Alternatively, the analytical calculations can be employed to design and analyze nanostructured optical lens with a significantly lower computational cost. In this method, each inclusion is represented by a single number (n_{eff} (x, y)), which drastically reduces the memory required to analyze large scale lenses. As a demonstration, we designed and analyzed a large-scale optical lens using the described approach.

In Figure 71(a), the radius distribution required to design a large-scale optical lens is shown. The phase profile in (4.4) was implemented over an area 1.64 mm x 1.64 mm using spherical inclusions using the relation in Figure 61(b). Using the analytical approach, the optical lens is replaced by an equivalent effective index distribution from which the electric field intensity along the focal axis can be calculated using the RS equation. In Figure 71(b), the intensity is plotted along the focal axis. The peak of the intensity coincides with the design focal length, marked by the vertical dotted line.

We have analyzed the large-scale optical lens for a range of numerical aperture and compared the obtained focal length with the designed focal length in Figure 71(c). Clearly, focal length of large-scale optical lens designed using this approach shows high fidelity to design focal length. The spot size, shown in Figure 71(c), decreases as the numerical aperture increases, implying a tighter focus at smaller focal length. The spot size compares well with that of a diffraction limited perfect lens, calculated using the Airy function [84]. In Figure 71(d), the accuracy of focal length prediction is plotted for the increasing wavelength. Here, a linear dispersion can be clearly seen. Across the visible spectrum, the dispersion is 26%.

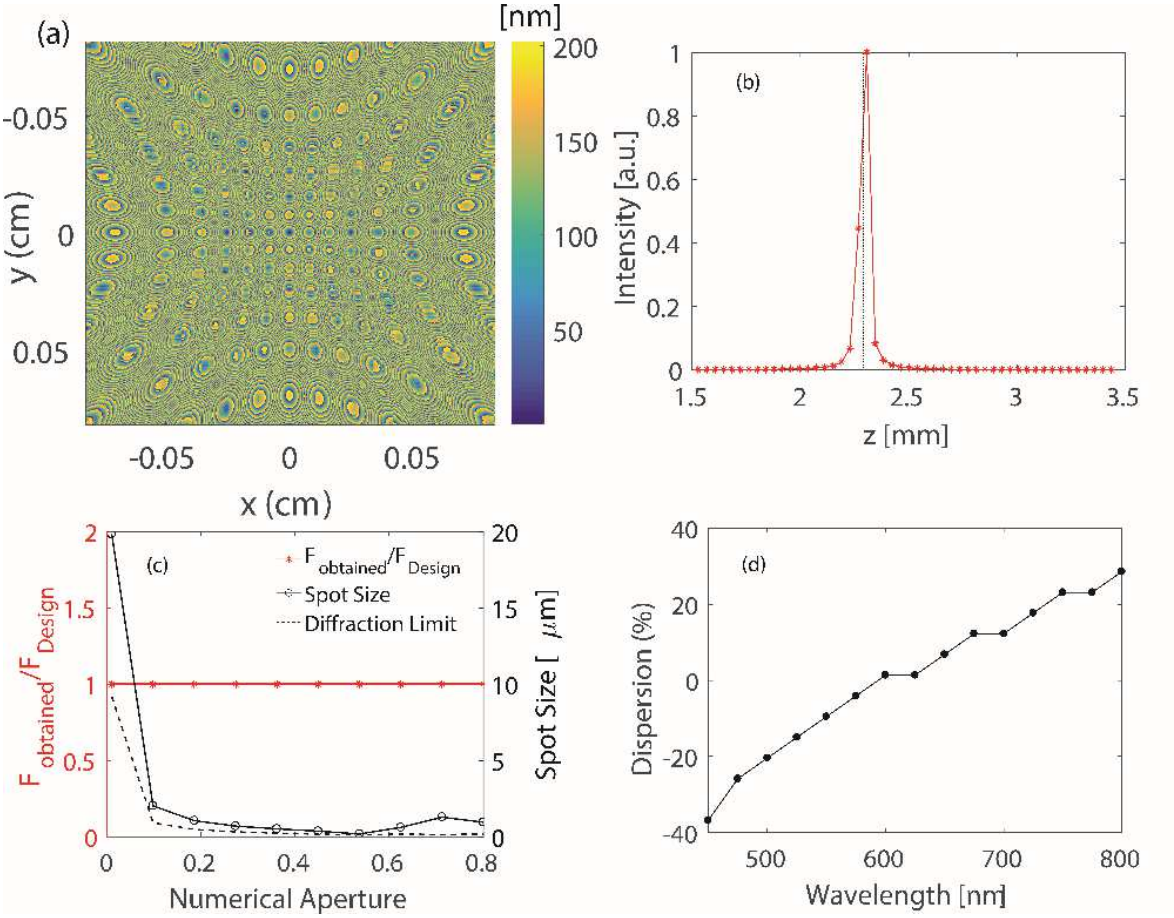

Figure 71(a) Radius distribution for a large-scale optical lens, (b) Intensity along the focal (z) axis, (c) ratio of obtained focal lengths and design focal length against increasing NA is shown in the right axis. In the left axis, the variation of the spot size is shown. The dotted line represents the diffraction limit of the spot size at increasing NA, (d) the change in obtained focal length compared to design focal length for increasing wavelength is shown.

2. PERFORMANCE ANALYSIS

In this section, we performed an FDTD analysis of the focusing efficiency, spot size and focal length of the optical lens by varying the design parameters such as the NA, operating wavelength, and polarization angle of the incident plane wave. For this analysis, with no loss of generality, we chose to study the optical lens composed of the spherical inclusions in rectangular and hexagonal lattices. The diameter of the lens studied here is limited to 20.4 □m. The results are summarized in Figure 72. In Figure 72(a), the spot size sharply decreases with numerical aperture. Both rectangular and hexagonal lattice lenses, marked by (R) and (H) in the plots, show similar performance with increasing numerical aperture. The dotted line marks the spot size of a diffraction limited perfect lens. Clearly, the designed optical lens can have a spot size very close to that of a diffraction limited perfect lens. The focusing efficiency (measured at the calculated focal plane) can reach almost 100% when NA < 0.1, and at higher numerical apertures, the efficiency gradually falls towards 20%. Low focusing efficiency at high NA is a well-known problem, arising from the inability of low index inclusions to diffract light in higher orders [162]. Based on Table 14, the efficiency and spot size of the designed optical lens at high NA are comparable to other reported values using similar materials, while at low NA, the designed metalens shows higher efficiency. The transmission of the optical lens remains above 82% in all cases. The high transmission is a consequence of the transparency of the constituent materials, and it makes the designed metalens suitable for cascading.

Although the dispersion of the glass materials is negligible, the implemented phase profile does not conform to (4) at other wavelengths, and chromatic aberration can be predicted. From Figure 72(b), the optical lens has a decreasing focal length with increasing wavelength, which agrees with previous reports [88]. While the design focal length is 18 □m, represented by the dotted line, the focal length changes from 28 □m to 9□□m as the wavelength changes from 400 nm to 800 nm. Such a dispersion can be useful when separating visible wavelengths in a micron size chip.

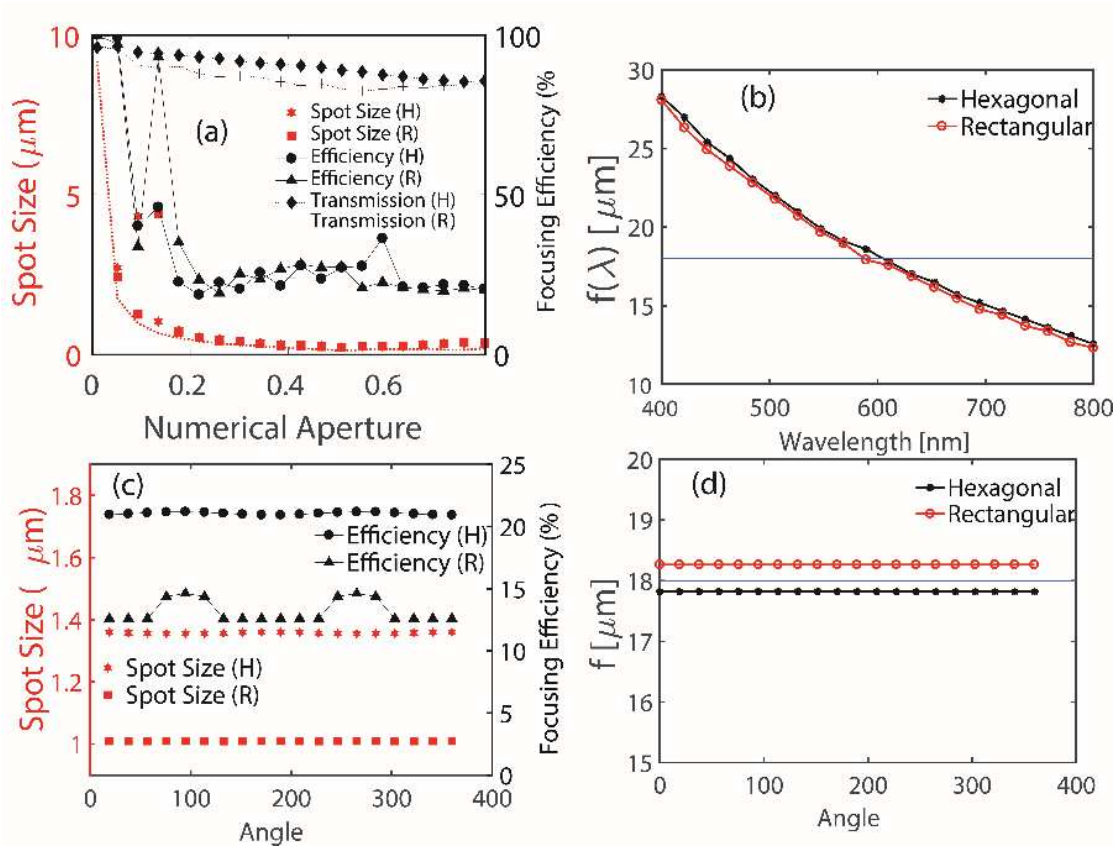

Figure 72(a) the change in spot size and the focusing efficiency of rectangular (R) and hexagonal (H) lattice metalens with increasing numerical aperture. (b) the dispersion of the focal length with increasing wavelength (NA = 0.5). The dotted line shows the design focal length (c) The change in spot size and efficiency of the lens (NA = 0.5) with the angle of polarization of the incident wave. (d) the dispersion of focal length with increasing polarization angle. The dotted line shows the design focal length.

Since the optical lenses are designed using four-fold symmetric inclusions, they should be insensitive to the angle of polarization of the incident plane wave. To test this, we calculate the performance parameters while changing the polarization angle of the incident wave. The angle of polarization is the angle of the E field with the x axis. In Figure 72(c), the spot sizes of the rectangular and hexagonal lattice optical lens are plotted, which remains unchanged with respect to polarization. Similarly, the efficiency remains insensitive to the polarization angle, as shown in Figure 72(c). Crucially, the focal length the lenses are also insensitive to polarization angle, as shown in Figure 72(d). The focal lengths for both lattices remain unchanged with the polarization angle, and remain close to the design focal length, represented by the dotted line. Thus, the optical lens is polarization insensitive, which makes it well-suited for imaging using unpolarized light, e.g., sunlight.

In addition to the numerical aperture, the f number, defined as the ratio of the focal length to the diameter of the lens, is also an important parameter. To study the performance of the designed metalens when the focal length is much larger than the diameter, we calculated the spot size and focusing efficiency of both the rectangular and hexagonal lattice lenses for the increasing f number. The results are summarized in Figure 73.

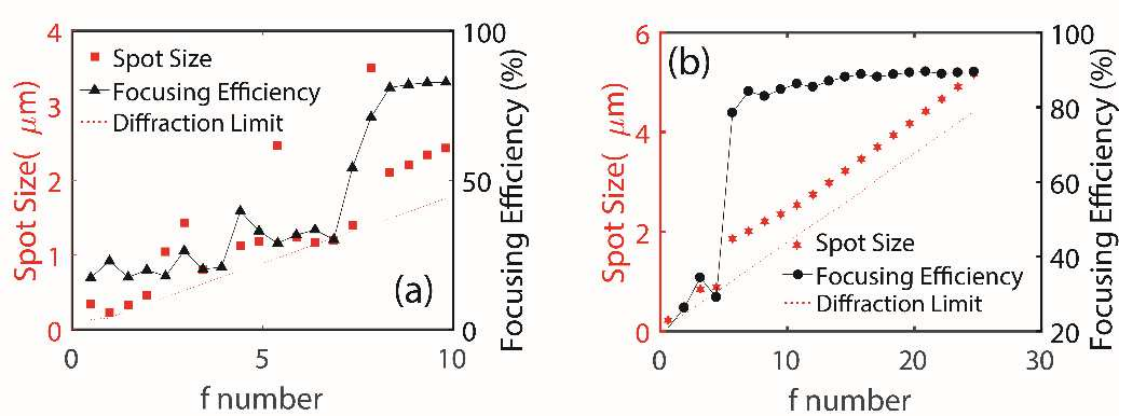

Figure 73 The spot size and focusing efficiency of (a) rectangular lattice and (b) hexagonal lattice metalens with respect to the f number. The dotted lines represent the diffraction limit of the spot size.

The spot size of both lattices rises steadily with the f number, but it remains close to the diffraction limit, represented by the dotted lines. While the spot size can be very close to the diffraction limit for high NA, it is much larger at a high f number (very low NA). For the rectangular lattice, the focusing efficiency rises above 50% at f number ≈7. However, for the hexagonal lattice, the efficiency rises above 50% when the f number ≈ 5. The focusing efficiency remains >80% when the f number >7. Although the performance of the hexagonal lattice and rectangular lattice remain similar when NA ϵ [0.2,0.8], the hexagonal lattice outperforms the rectangular lattice when the f number >5. At a high f number, diffraction into higher orders is not required, leading to high focusing efficiency. The slight enhancement of focusing efficiency for a hexagonal lattice can be attributed to its higher packing factor. For the same NA or f number, the hexagonal lattice can accommodate a larger number of inclusions, which enhances the focusing performance.

3. IMPACT OF IMPERFECTION

We have simulated the optical lens assuming perfect fabrication and no optical errors. While optical systems with close to perfect performance can be available, a fabrication error is harder to avoid. In our design, there are two parameters that are vulnerable to imperfection, viz., the position and the radius of the inclusions. To understand the impact of imperfection, we have studied the performances of the optical lens using FDTD when a degree of uncertainty is added to these parameters. The results are summarized in Figure 74.

To understand the impact of an imperfect arrangement of the inclusions, an uncertainty with standard deviation σ_1 is added to the position vertices of the spheres. The efficiency and spot size are calculated when σ_1 increases up to 15% of the lattice constant *a.* From Figure 74(a), the focusing efficiency decreases by up to three percentage points when the position imperfection increases. In this case, the spot size changes very little. Thus, the imperfection in the position decreases the focusing efficiency, but the spot size remains relatively unchanged. A similar calculation is performed by adding an uncertainty with standard deviation σ_2 to the radii of the spheres. The performance of the optical lens is calculated when σ_2 increases up to 15% of the maximum radius. From Figure 74(b), the focusing efficiency shows change with a range of 5% when the radius imperfection increases. Like the previous case, the spot size shows very little change.

In Figure 74(c), the intensity of the transmitted light along the focal axis (z axis) is plotted when both the position and radius uncertainty are added. As the standard deviation of imperfection rises from 0 to 0.28*a*, the peak intensity along the focal axis falls,

but the focal distance remains the same. In all cases shown in Figure 74(c), the focal distance remains equal to the design focal length, marked by the dotted line. Similarly, with increasing imperfection, the peak intensity in the focal spot decreases, as shown in Figure 74(d). However, the spot size shows little change with increasing imperfection.

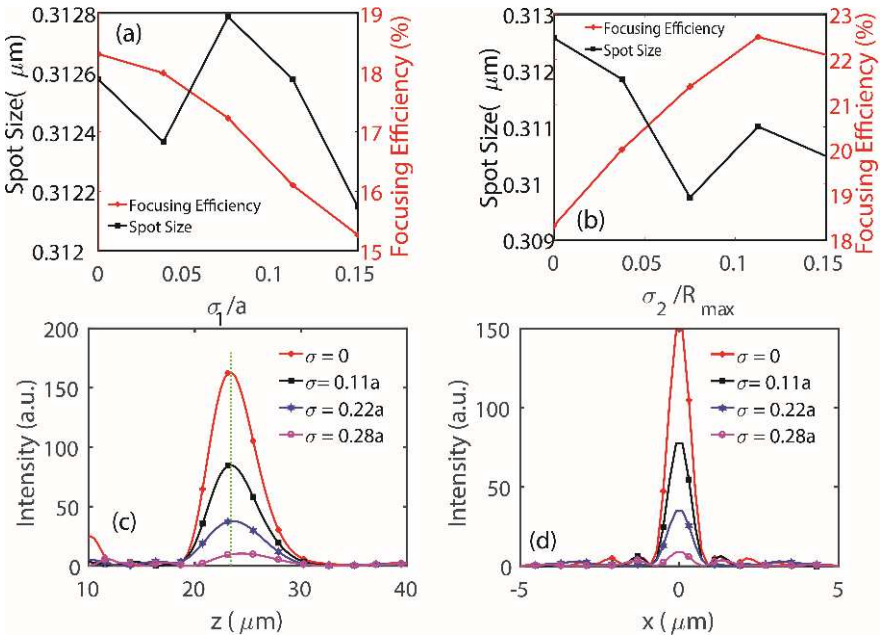

Figure 74 The change in the spot size and focusing efficiency of the hexagonal lattice metalens when (a) the position imperfection and (b) radius imperfection increases. (c) The intensity along the focal axis, (d) the intensity along the x axis in the focal plane.

The above analysis clearly shows that the focal length and spot size of the optical lens show remarkable robustness to uncertainty in the constituent parameters. The metalens can focus light into a spot in the focal plane with as much as 0.28a uncertainty. This allows for flexibility in fabrication with minimal loss of performance.

4. CHROMATIC ABERRATION

In the previous sections, it has been seen that the focal length of the optical element is highly wavelength dependent. In this section we will study this chromatic aberration and determine the factors that control it. It is noteworthy that the material used

in this analysis has been highly nondispersive. As such, material dispersion plays a negligible role in the chromatic aberration.

Let us start by considering a general ideal thin planoconvex lens, the Radius of curvature of which is 100mm, with non-dispersive glass as the material (n = 1.5). Thus, from the lens makers equation:

$$\frac{1}{F} = (1.5 - 1)\left(\frac{1}{R}\right) => F = 2R. \quad (4.9)$$

Where F is the focal length of the lens and the radius is R. Let us consider such a lens with diameter 4.8 mm. The focal length would also be 4.8 mm. The operation of this lens is nondispersive since the material is non-dispersive.

We can investigate whether the flatness of the optical element causes the chromatic aberration by converting the nondispersive planoconvex lens into a flat gradient index (GRIN) lens. The GRIN lens is calculated by imagining the curved lens with a flat box and then calculating the effective index. The effective index would be highest in the middle part and reduced at the two ends. The thickness of the GRIN lens is the same as the ideal thin lens, which is 60 □m. The distribution of the effective index in one half of the lens is shown in Figure 75(a). The other half is mirror symmetric. Using this GRIN lens, light can be focused on one spot, as shown in Figure 75(b). Clearly, the GRIN lens is equivalent to the planoconvex focusing lens.

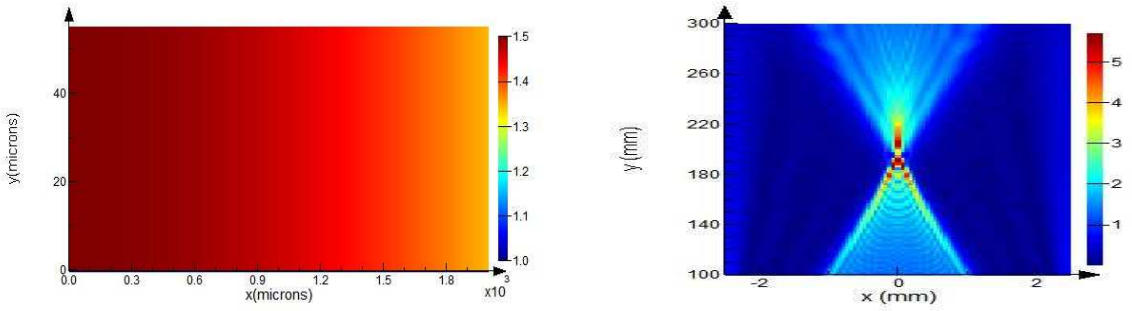

(a) (b)

Figure 75(a) the index distribution of the equivalent GRIN lens, (b) The focusing by the equivalent GRIN lens.

The calculated focal length is plotted against operating wavelength in Figure 76. The focal length remains relatively unchanged. It changed 5 mm (2.5%) over a range of 400nm. Clearly, the flat GRIN lens is nondispersive, if the index of the refraction is nondispersive.

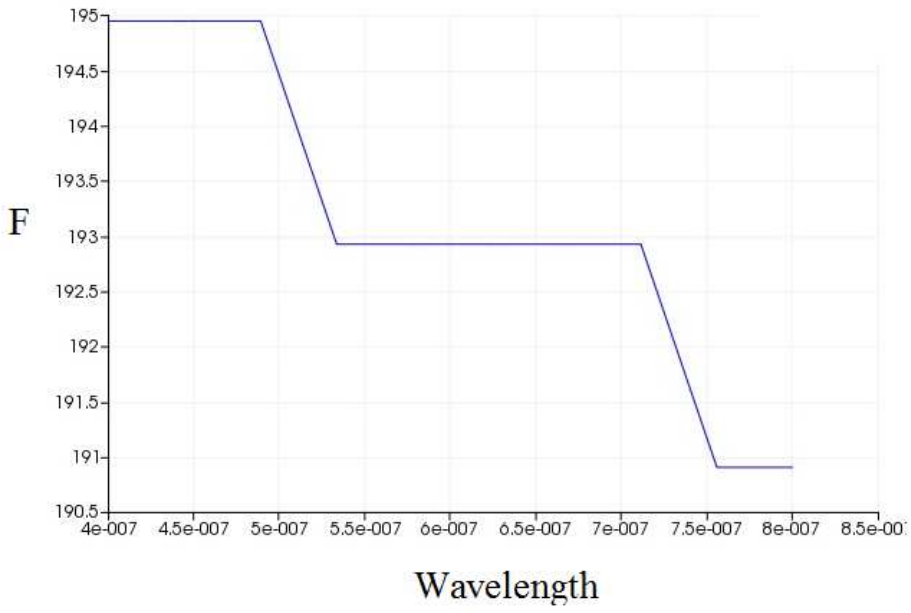

Figure 76 The focal length (F) of the flat GRIN lens with respect to operating wavelength.

In case of the flat GRIN lens, the design is independent of the wavelength, with a thickness that is comparable to the ideal planoconvex lens. Let us now consider a GRIN

lens with a much smaller thickness of 1 □m. The effective index in this case can be calculated from eq. (4.1) by setting H = 1 □m, and λ = 600 nm, and $\phi_{\text{prop}} = mod(\frac{2\pi}{\lambda}\sqrt{x^2+f^2}, 2\pi)$ as the parabolic chirped phase. The n_{eff} shows a rapid switch between high and low values, as shown in Figure 77(a).

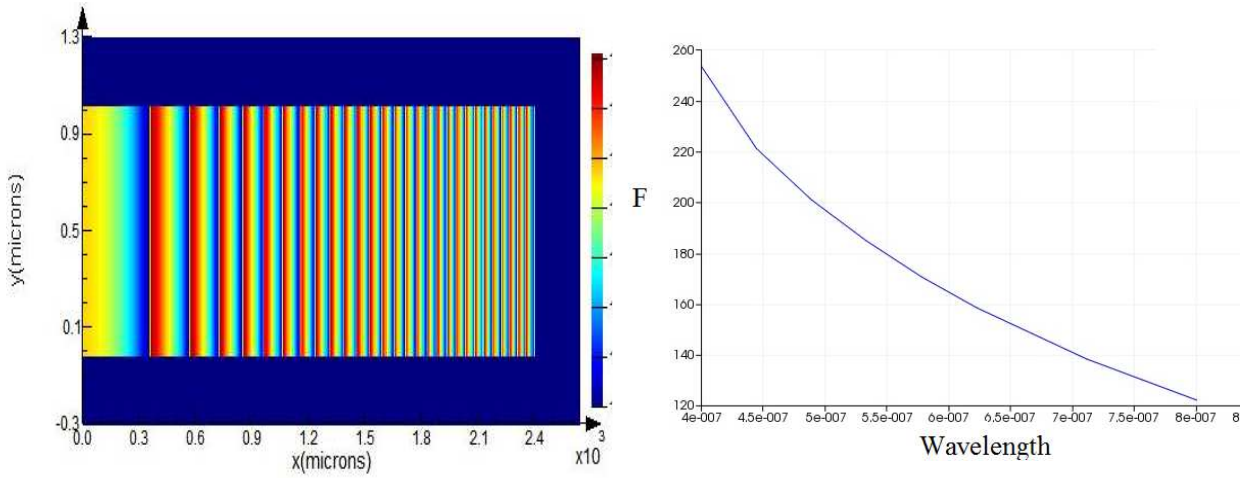

(a) (b)

Figure 77 (a) Index distribution for a 1 □m thin flat GRIN lens, (b) The wavelength dependence of focal length.

Unlike the previous GRIN lens, this 1 □m thick lens is highly dispersive. Clearly, when the thickness is comparable to the wavelength, the resulting lenses are highly dispersive. Let us extend this concept to the designed metalenses. We arrange a group of cylindrical elements in a rectangular grid to achieve a specific phase φ at the face of the lens. The required phase to achieve the focusing effect is given by eq. (4). The radius of each cylinder can be calculated as:

$$R = \sqrt{\frac{a^2\left(\phi^2\lambda_{op}^2 - 4\pi^2H^2\right)}{8\pi^3H^2\left(n_p^2 - 1\right)}} \qquad (4.10)$$

where n_p is the refractive index of the cylindrical element, R is the cylinder face radius, H is the thickness, and *a* is the period of the grid. We calculate the intensity along the focal axis for various wavelengths while increasing the H.

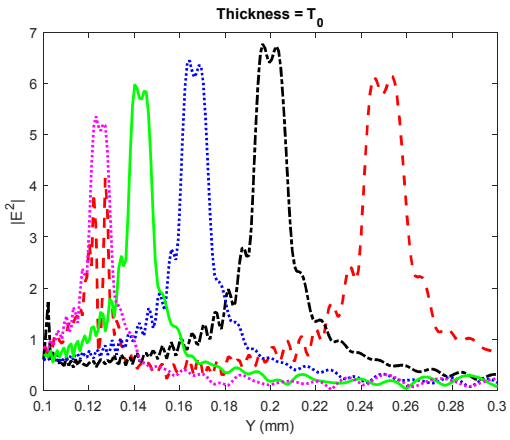

(a)

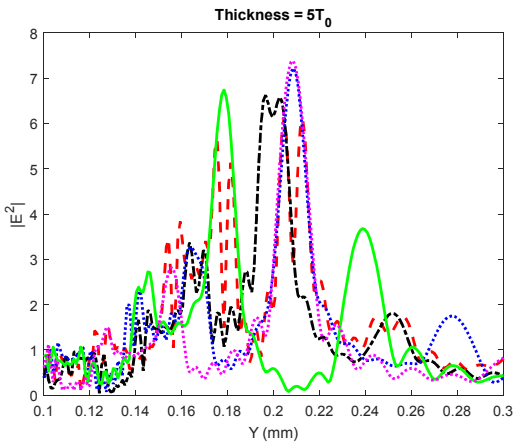

(b)

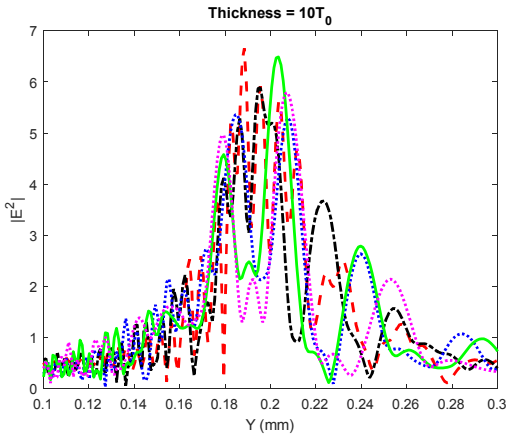

(d)

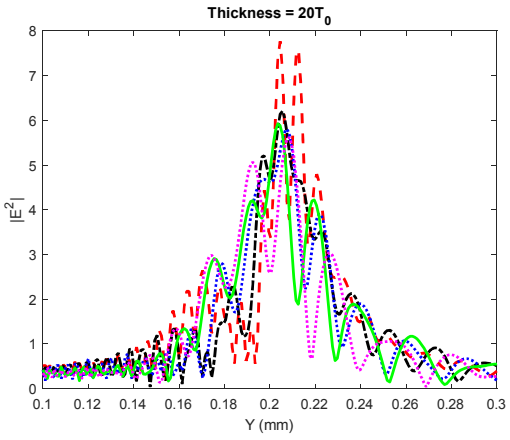

(c)

Figure 78 The intensity along the focal axis for different wavelength at (a) H = T0, (b) H = 5T0, (c) H = 10T0, and (d) H = 20 T0.

From Figure 78, the focal spots for different wavelengths vary greatly when the thickness is small, but at greater thickness, the focal spots converge to one spot. Thus, the thickness of the lens can control the chromatic aberration.

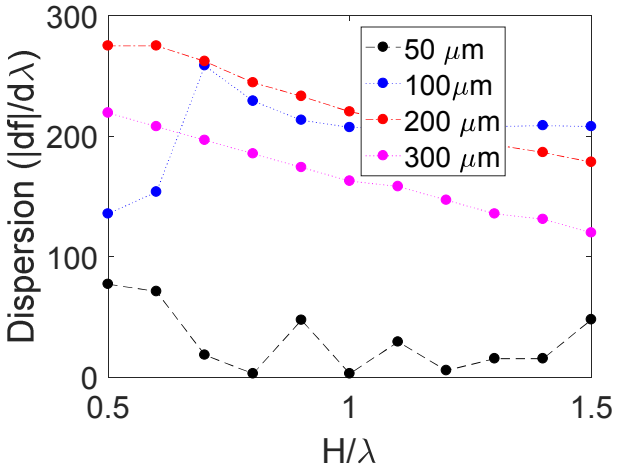

Figure 79 The dispersion of optical element for different thickness as focal length;

In Figure 79, it is shown that the dispersion of nanostructured optical elements reduces linearly with thickness. Thus, the dispersion can be controlled by simply controlling the thickness.

D. Summary

We have designed a robust and polarization insensitive optical lens using low index inclusions arranged on a glass substrate and analyzed their performance numerically. It was shown that phase calculations can be accurately done using EMA. Subsequently, a combination of EMA and diffraction equation was used to analyze optical lens using different shapes of inclusions and with different numerical aperture. The analytical results agreed well with FDTD predictions and experimental results, establishing the accuracy of the analytical method. Using this approach, a large-scale optical lens was designed with high fidelity between designed and calculated focal length. The focusing efficiency and spot size of the optical lens were studied at different design parameters. The optical lens showed efficiency >85% at low NA, while maintaining efficiency ≈ 20% at NA ϵ [0.2,0.8]. The spot size was comparable to the diffraction limit

while the transmission remains above 82%, making it suitable for cascading. While the lens was sensitive to the wavelength of incident light, it was insensitive to its angle of polarization. The focal length and spot size showed remarkable robustness to imperfections in design, while the efficiency decreases. The chromatic aberration of the optical elements was analyzed, and it was shown that the chromatic dispersion can be controlled by the thickness of the optical element. The result indicates that design and analyses of optical lens with subwavelength inclusion can be done using an analytical method based on EMA and the diffraction formula. It is also shown that a transparent material like glass can be a suitable material for subwavelength optical lens.

V. CONCLUSION

A. Summary

In this work, optical nanostructures were studied in order to obtain useful optical properties in a controllable manner. We have paid close attention to design and analysis of different nanostructures using full-wave numerical methods and analytical methods. We have also demonstrated transparent optical nanostructures by using low-loss and transparent materials to obtain desired optical effects.

As a first step, numerical analysis of optical nanostructures was reviewed. The FDTD and PWE methods were discussed and applied to model a variety of optical nanostructures. Specifically, periodic nanostructures with low index materials were analyzed. Based on the analysis, the minimum bandgap required to obtain optical bandgap were established as 1.5. Furthermore, refractive index sensors based on bandgap resonators were numerically demonstrated on low loss transparent materials. It was established that low loss transparent materials can be used for building effective sensors if there is an airbridge between the nanostructure and the substrate. A strategy for controlling the position of bandgap, as well as operating wavelength of the sensor, by changing the period and fill-factor of the periodic nanostructure was established. The numerical analysis established that low index materials can be suitable for optical nanostructures. However, numerical analyses were found to require significant time and computational resources to produce accurate results. Additionally, deriving the control strategy of the controllable nanostructure required performing many time-consuming analyses.

Next, we derived an analytical effective medium approximation that can model the transmission and reflection of optical nanostructure containing inclusions of any size and physical configuration. The derived EMA extended the existing Maxwell-Garnett approximation using Mie scattering theory. The framework was tested for a wide range of optical nanostructures. Their experimentally obtained transmission and reflection were compared with the analytical prediction. It was found that the derived framework produces more accurate prediction compared to the available analytical EMAs found in the literature. As demonstration of the usefulness of the derived EMAs, magnetic microsphere colloids were modelled. The colloids were aperiodic, containing core-shell inclusions that are comparable to or greater than the operating wavelength in size. The derived EMA showed much better accuracy in modelling the transmission of the colloids. Additionally, the magnetic response was modelled. The derived EMA was able to relate the physical properties of the different nanostructures with their transmission analytically. Thus, the controllable and tunable properties could be modelled analytically, which required much less time, compared to full-wave numerical analyses. For example, the dynamic tunability of the magnetic colloid could be analytically derived using the EMA. The filling -factor of the nanostructures required to obtain different transmissions and reflections could be analytically calculated with good accuracy without performing time consuming full-wave numerical analyses.

Using the derived EMA, the transmission and reflection of controllable and tunable optical nanostructures can be modelled. Coupling this EMA with scalar diffraction theory, it is possible to analytically calculate the far-field patterns of any optical nanostructure. An analytical method coupling the EMA with the diffraction theory was designed and used

for analyzing flat, ultra-thin optical nanostructure that can mimic bulky optical elements. Flat lenses with controllable focal length and numerical aperture was designed and analyzed. The analytical method was compared with numerical and experimental results. It was found that the analytical method produced accurate prediction of the far-field properties of the optical elements, while being much faster and efficient compared to numerical methods. The chromatic aberration of subwavelength optical elements was studied, and it was found that the thickness of the elements directly correlates with aberration. That is, thinner elements have higher chromatic aberration, while thicker ones have lower chromatic aberration. Low refractive index materials were used in designing these optical elements, demonstrating the feasibility of designing controllable and tunable optical nanostructure using low loss materials.

B. Limitations

Although the research presented here remains quite general in its applications, there are some limitations. The fabrication of the designs presented here remains a challenge. We have designed optical nanostructures on a wide range of materials including glass and polymers. However, there are few available fabrication technologies that can fabricate complicated structures on glass and polymers. Furthermore, the effective medium framework presented here hasn't been able to eliminate all the shortcomings of the available EMAs. For example, the formula is still asymmetric. That is, a symmetric switch between the matrix and inclusion material doesn't produce the same result. As a result, the effective medium theory presented here remains applicable only below the percolation threshold. Therefore, tightly packed systems cannot be accurately modelled using this formula. In addition, effects of periodicity have not been accounted

for in this framework. The analytical framework has been able to predict the far-field behaviors of optical nanostructures using diffraction theory, which is reliant on Fourier transform. Thus, the accuracy of the results is highly dependent on accurate sampling of the nanostructure.

C. Future Work

In this work, controllable and tunable optical nanostructures on low loss material was studied. An efficient and fast analytical method was demonstrated for design and analysis of such nanostructures. As a next step, the fabrication of these devices will be addressed. Nanosphere lithography [77] and self-assembly [163] were used for fabricating low-loss optical nanostructures using polymers and oxides. These methods remain potential candidates for fabricating the controllable and tunable optical nanostructures.

Additionally, the limitations of the proposed effective medium theory will be addressed in future studies. One possible solution to most of the limitations would be to approach the effective medium in a way similar to that in [103], with the added complexity of having to solve a nonlinear complex implicit equation. Such a solution should be able to predict the behavior of effective medium even when the filling factor is particularly high.

VI. REFERENCES

[1] F. Flory, L. Escoubas, and G. Berginc, "Optical properties of nanostructured materials: a review," *Journal of Nanophotonics,* vol. 5, p. 052502, 2011.

[2] A. I. Kuznetsov, A. E. Miroshnichenko, M. L. Brongersma, Y. S. Kivshar, and B. Luk'yanchuk, "Optically resonant dielectric nanostructures," *Science,* vol. 354, p. aag2472, 2016.

[3] A. A. Siraji and M. S. Alam, "A tunable photonic double heterostructure cavity on ferroelectric barium titanate," *IEEE Photonics Technology Letters,* vol. 25, pp. 1676-1679, 2013.

[4] A. A. Siraji and Y. Zhao, "High-sensitivity and high-Q-factor glass photonic crystal cavity and its applications as sensors," *Optics letters,* vol. 40, pp. 1508-1511, 2015.

[5] R. Gajić, R. Meisels, F. Kuchar, and K. Hingerl, "All-angle left-handed negative refraction in Kagomé and honeycomb lattice photonic crystals," *Physical Review B - Condensed Matter and Materials Physics,* vol. 73, 2006.

[6] R. Ruppin, "Evaluation of extended Maxwell-Garnett theories," *Optics Communications,* vol. 182, pp. 273-279, 2000.

[7] D. R. Smith, S. Schultz, P. Markoš, and C. Soukoulis, "Determination of effective permittivity and permeability of metamaterials from reflection and transmission coefficients," *Physical Review B,* vol. 65, p. 195104, 2002.

[8] C. F. Bohren, X. Xiao, and A. Lakhtakia, "The missing ingredient in effective-medium theories: standard deviations," *Journal of Modern Optics,* vol. 59, pp. 1312-1315, 2012.

[9] A. A. Siraji, M. S. Alam, and S. Haque, "Impact of space modulation on confinement of light in a novel photonic crystal cavity on ferroelectric barium titanate," *Journal of Lightwave Technology,* vol. 31, pp. 802-808, 2013.

[10] J. Ge, Y. Hu, T. Zhang, T. Huynh, and Y. Yin, "Self-assembly and field-responsive optical diffractions of superparamagnetic colloids," *Langmuir,* vol. 24, pp. 3671-3680, 2008.

[11] L. Rayleigh, "LVI. On the influence of obstacles arranged in rectangular order upon the properties of a medium," *The London, Edinburgh, and Dublin Philosophical Magazine and Journal of Science,* vol. 34, pp. 481-502, 1892/12/01 1892.

[12] M. FLOQUET, *ÉQUATIONS DIFFÉRENTIELLES LINÉAIRES*, 1884.

[13] F. Bloch, "Über die quantenmechanik der elektronen in kristallgittern," *Zeitschrift für Physik A Hadrons and Nuclei,* vol. 52, pp. 555-600, 1929.

[14] V. P. Bykov, "Spontaneous emission from a medium with a band spectrum," *Soviet Journal of Quantum Electronics,* vol. 4, p. 861, 1975.

[15] V. A. Sychugov, A. V. Tishchenko, and A. Khakimov, "Thin-film laser based on a Bragg waveguide," *Soviet Journal of Quantum Electronics,* vol. 10, p. 1314, 1980.

[16] E. Yablonovitch, "Inhibited spontaneous emission in solid-state physics and electronics," *Physical review letters,* vol. 58, p. 2059, 1987.

[17] S. John, "Strong localization of photons in certain disordered dielectric superlattices," *Physical review letters,* vol. 58, p. 2486, 1987.

[18] K. Leung and Y. Liu, "Full vector wave calculation of photonic band structures in face-centered-cubic dielectric media," *Physical Review Letters,* vol. 65, p. 2646, 1990.

[19] K. Ho, C. T. Chan, and C. M. Soukoulis, "Existence of a photonic gap in periodic dielectric structures," *Physical Review Letters,* vol. 65, p. 3152, 1990.

[20] E. Yablonovitch, T. Gmitter, and K. Leung, "Photonic band structure: The face-centered-cubic case employing nonspherical atoms," *Physical review letters,* vol. 67, p. 2295, 1991.

[21] K. M. Ho, C. T. Chan, C. Soukoulis, R. Biswas, and M. Sigalas, "Photonic band gaps in three dimensions: new layer-by-layer periodic structures," *Solid State Communications,* vol. 89, pp. 413-416, 1994.

[22] S.-Y. Lin and J. G. Fleming, "A three-dimensional optical photonic crystal," *Journal of Lightwave Technology,* vol. 17, p. 1944, 1999.

[23] Y. A. Vlasov, X.-Z. Bo, J. C. Sturm, and D. J. Norris, "On-chip natural assembly of silicon photonic bandgap crystals," *Nature,* vol. 414, pp. 289-293, 2001.

[24] Y. Akahane, T. Asano, B.-S. Song, and S. Noda, "High-Q photonic nanocavity in a two-dimensional photonic crystal," *Nature,* vol. 425, pp. 944-947, 2003.

[25] E. Chow, A. Grot, L. Mirkarimi, M. Sigalas, and G. Girolami, "Ultracompact biochemical sensor built with two-dimensional photonic crystal microcavity," *Optics letters,* vol. 29, pp. 1093-1095, 2004.

[26] O. Painter, R. Lee, A. Scherer, A. Yariv, J. O'brien, P. Dapkus*, et al.*, "Two-dimensional photonic band-gap defect mode laser," *Science,* vol. 284, pp. 1819-1821, 1999.

[27] A. Chutinan and S. Noda, "Waveguides and waveguide bends in two-dimensional photonic crystal slabs," *Physical review B,* vol. 62, p. 4488, 2000.

[28] E. Cubukcu, K. Aydin, E. Ozbay, S. Foteinopolou, and C. M. Soukoulis, "Subwavelength resolution in a two-dimensional photonic-crystal-based superlens," *Physical Review Letters,* vol. 91, pp. 207401/1-207401/4, 2003.

[29] D. Englund, D. Fattal, E. Waks, G. Solomon, B. Zhang, T. Nakaoka*, et al.*, "Controlling the spontaneous emission rate of single quantum dots in a two-dimensional photonic crystal," *Physical review letters,* vol. 95, p. 013904, 2005.

[30] A. Berrier, M. Mulot, M. Swillo, M. Qiu, L. Thylén, A. Talneau*, et al.*, "Negative Refraction at Infrared Wavelengths in a Two-Dimensional Photonic Crystal," *Physical Review Letters,* vol. 93, p. 073902, 08/11/ 2004.

[31] E. Cubukcu, K. Aydin, E. Ozbay, S. Foteinopoulou, and C. M. Soukoulis, "Electromagnetic waves: Negative refraction by photonic crystals," *Nature,* vol. 423, pp. 604-605, 06/05/print 2003.

[32] N. Takato, K. Jinguji, M. Yasu, H. Toba, and M. Kawachi, "Silica-based single-mode waveguides on silicon and their application to guided-wave optical interferometers," *Journal of Lightwave Technology,* vol. 6, pp. 1003-1010, 1988.

[33] K. Hill, Y. Fujii, D. C. Johnson, and B. Kawasaki, "Photosensitivity in optical fiber waveguides: Application to reflection filter fabrication," *Applied physics letters,* vol. 32, pp. 647-649, 1978.

[34] R. Adar, C. H. Henry, R. F. Kazarinov, R. C. Kistler, and G. R. Weber, "Adiabatic 3-dB couplers, filters, and multiplexers made with silica waveguides on silicon," *Journal of lightwave technology,* vol. 10, pp. 46-50, 1992.

[35] V. Reboud, P. Lovera, N. Kehagias, M. Zelsmann, C. Schuster, F. Reuther*, et al.*, "Two-dimensional polymer photonic crystal band-edge lasers fabricated by nanoimprint lithography," *Applied Physics Letters,* vol. 91, p. 151101, 2007.

[36] J. Lapointe, M. Gagné, M.-J. Li, and R. Kashyap, "Making smart phones smarter with photonics," *Optics express,* vol. 22, pp. 15473-15483, 2014.

[37] A. Rosenberg, R. Tonucci, H.-B. Lin, and A. Campillo, "Near-infrared two-dimensional photonic band-gap materials," *Optics letters,* vol. 21, pp. 830-832, 1996.

[38] H.-B. Lin, R. J. Tonucci, and A. J. Campillo, "Two-dimensional photonic bandgap optical limiter in the visible," *Optics Letters,* vol. 23, 1998.

[39] K. Sakoda, "Transmittance and Bragg re8ectivity of two-dimensional photonic lattices," *Physical Review B,* vol. 52, 1995.

[40] F. Capolino, *Applications of metamaterials*: CRC press, 2009.

[41] S. Jahani and Z. Jacob, "All-dielectric metamaterials," *Nat Nano,* vol. 11, pp. 23-36, 01//print 2016.

[42] A. Ahmadi and H. Mosallaei, "Physical configuration and performance modeling of all-dielectric metamaterials," *Phys. Rev. B,* vol. 77, p. 045104, // 2008.

[43] M. I. Mishchenko and A. A. Lacis, "Manifestations of morphology-dependent resonances in Mie scattering matrices," *Applied mathematics and computation,* vol. 116, pp. 167-179, 2000.

[44] S. Jahani and Z. Jacob, "All-dielectric metamaterials," *Nature nanotechnology,* vol. 11, p. 23, 2016.

[45] C. F. Bohren and D. R. Huffman, "Absorption and Scattering of Light by Small Particles," ed, 2008.

[46] J. C. Ginn, "Realizing optical magnetism from dielectric metamaterials," *Phys. Rev. Lett.,* vol. 108, p. 097402, // 2012.

[47] J. Wang, Z. Xu, B. Du, S. Xia, J. Wang, H. Ma*, et al.*, "Achieving all-dielectric left-handed metamaterials via single-sized dielectric resonators," *Journal of Applied Physics,* vol. 111, p. 044903, 2012.

[48] R. Fleury, D. L. Sounas, and A. Alu, "Negative refraction and planar focusing based on parity-time symmetric metasurfaces," *Physical review letters,* vol. 113, p. 023903, 2014.

[49] T. Liu, L. Huang, W. Hong, Y. Ling, J. Luan, Y. Sun*, et al.*, "Coupling-based Huygens’ meta-atom utilizing bilayer complementary plasmonic structure for light manipulation," *Optics Express,* vol. 25, pp. 16332-16346, 2017/07/10 2017.

[50] A. Mafi, "Transverse Anderson localization of light: a tutorial," *Advances in Optics and Photonics,* vol. 7, pp. 459-515, 2015.

[51] N. Gandji, G. Semouchkin, and E. Semouchkina, "All-dielectric metamaterials: irrelevance of negative refraction to overlapped Mie resonances," *Journal of Physics D: Applied Physics,* vol. 50, p. 455104, 2017.

[52] V. Yannopapas, "Negative refraction in random photonic alloys of polaritonic and plasmonic microspheres," *Physical Review B,* vol. 75, p. 035112, 2007.

[53] M. S. Wheeler, J. S. Aitchison, and M. Mojahedi, "Coated nonmagnetic spheres with a negative index of refraction at infrared frequencies," *Physical Review B,* vol. 73, p. 045105, 2006.

[54] N. Limberopoulos, A. Akyurtlu, K. Higginson, A.-G. Kussow, and C. D. Merritt, "Negative refractive index metamaterials in the visible spectrum based on Mg B 2⁄ Si C composites," *Applied Physics Letters,* vol. 95, p. 186, 2009.

[55] V. Yannopapas, "Binary alloy of virus capsids and gold nanoparticles as a mie-resonance-based optical metamaterial," *Solid State Communications,* vol. 204, pp. 51-55, 2015.

[56] M. Shrestha, A. Asundi, and G.-K. Lau, "Electrically tunable window based on microwrinkled ZnO/Ag thin film," in *Electroactive Polymer Actuators and Devices (EAPAD) 2017*, 2017, p. 101631Y.

[57] J. J. Carson, M. Najiminaini, F. Vasefi, and B. Kaminska, "Nanostructure-based optical filters for multispectral imaging applications," in *AIP Conference Proceedings*, 2014, pp. 57-63.

[58] E. Lee, M. Zhang, Y. Cho, Y. Cui, J. Van der Spiegel, N. Engheta*, et al.*, "Tilted Pillars on Wrinkled Elastomers as a Reversibly Tunable Optical Window," *Advanced Materials,* vol. 26, pp. 4127-4133, 2014.

[59] D. Ge, E. Lee, L. Yang, Y. Cho, M. Li, D. S. Gianola*, et al.*, "A Robust Smart Window: Reversibly Switching from High Transparency to Angle-Independent Structural Color Display," *Advanced Materials,* vol. 27, pp. 2489-2495, 2015.

[60] S. Leinberg, V. Kisand, A. Šutka, K. Saal, R. Lõhmus, U. Joost*, et al.*, "Switchable optical transmittance of TiO2 submicron-diameter wire suspension-based “smart window” device," *Optical Materials,* vol. 46, pp. 418-422, 2015/08/01/ 2015.

[61] O. Philippova, A. Barabanova, V. Molchanov, and A. Khokhlov, "Magnetic polymer beads: Recent trends and developments in synthetic design and applications," *European Polymer Journal,* vol. 47, pp. 542-559, 2011.

[62] I. Hilger, W. Andrä, R. Hergt, R. Hiergeist, H. Schubert, and W. A. Kaiser, "Electromagnetic heating of breast tumors in interventional radiology: in vitro and in vivo studies in human cadavers and mice," *Radiology,* vol. 218, pp. 570-575, 2001.

[63] J. Russell, A. Birnie, and A. Fraser, "High-gradient magnetic separation (HGMS) in soil clay mineral studies," *Clay Minerals,* vol. 19, pp. 771-778, 1984.

[64] B. B. Yellen, Z. G. Forbes, D. S. Halverson, G. Fridman, K. A. Barbee, M. Chorny*, et al.*, "Targeted drug delivery to magnetic implants for therapeutic applications," *Journal of Magnetism and Magnetic Materials,* vol. 293, pp. 647-654, 2005.

[65] J. A. Ritter, A. D. Ebner, K. D. Daniel, and K. L. Stewart, "Application of high gradient magnetic separation principles to magnetic drug targeting," *Journal of Magnetism and Magnetic Materials,* vol. 280, pp. 184-201, 2004.

[66] K. Jeong, L. Petrakis, M. Takayasu, and F. Friedlaender, "SYMPOSIUM ON CHARACTERIZATION AND CHEMISTRY OF OIL SHALES."

[67] O. Veiseh, C. Sun, J. Gunn, N. Kohler, P. Gabikian, D. Lee*, et al.*, "Optical and MRI multifunctional nanoprobe for targeting gliomas," *Nano letters,* vol. 5, pp. 1003-1008, 2005.

[68] S. Sacanna and A. Philipse, "Preparation and properties of monodisperse latex spheres with controlled magnetic moment for field-induced colloidal crystallization and (dipolar) chain formation," *Langmuir,* vol. 22, pp. 10209-10216, 2006.

[69] J. Ge, L. He, J. Goebl, and Y. Yin, "Assembly of magnetically tunable photonic crystals in nonpolar solvents," *Journal of the American Chemical Society,* vol. 131, pp. 3484-3486, 2009.

[70] L. He, V. Malik, M. Wang, Y. Hu, F. E. Anson, and Y. Yin, "Self-assembly and magnetically induced phase transition of three-dimensional colloidal photonic crystals," *Nanoscale,* vol. 4, pp. 4438-4442, 2012.

[71] H. Hu, Q.-W. Chen, J. Tang, X.-Y. Hu, and X.-H. Zhou, "Photonic anti-counterfeiting using structural colors derived from magnetic-responsive photonic crystals with double photonic bandgap heterostructures," *Journal of Materials Chemistry,* vol. 22, p. 11048, 2012.

[72] W. Wang, Q. Li, A. Zheng, X. Li, Z. Pan, J. Jiang*, et al.*, "Superparamagnetic iron oxide nanoparticles for full-color photonic materials with tunable properties," *Results in Physics,* vol. 14, p. 102366, 2019.

[73] J. Goebl, Y. Liu, S. Wong, S. Zorba, and Y. Yin, "Magnetically tunable colloidal micromirrors," *Nanoscale Horizons,* vol. 1, pp. 64-68, 2016.

[74] C. Lee, H. Lee, and R. Westervelt, "Microelectromagnets for the control of magnetic nanoparticles," *Applied physics letters,* vol. 79, pp. 3308-3310, 2001.

[75] J. S. Beveridge, J. R. Stephens, A. H. Latham, and M. E. Williams, "Differential magnetic catch and release: analysis and separation of magnetic nanoparticles," *Analytical chemistry,* vol. 81, pp. 9618-9624, 2009.

[76] S. P. Yeap, S. S. Leong, A. L. Ahmad, B. S. Ooi, and J. Lim, "On size fractionation of iron oxide nanoclusters by low magnetic field gradient," *The Journal of Physical Chemistry C,* vol. 118, pp. 24042-24054, 2014.

[77] Y. Zhao, J. Wang, and G. Mao, "Colloidal subwavelength nanostructures for antireflection optical coatings," *Optics letters,* vol. 30, pp. 1885-1887, 2005.

[78] B.-T. Liu and W.-D. Yeh, "Antireflective surface fabricated from colloidal silica nanoparticles," *Colloids and Surfaces A: Physicochemical and Engineering Aspects,* vol. 356, pp. 145-149, 2010.

[79] K. Askar, B. M. Phillips, Y. Fang, B. Choi, N. Gozubenli, P. Jiang*, et al.*, "Self-assembled self-cleaning broadband anti-reflection coatings," *Colloids and Surfaces A: Physicochemical and Engineering Aspects,* vol. 439, pp. 84-100, 2013.

[80] M. Decker, I. Staude, M. Falkner, J. Dominguez, D. N. Neshev, I. Brener*, et al.*, "High-Efficiency Dielectric Huygens' Surfaces," *Advanced Optical Materials,* vol. 3, pp. 813-820, 2015.

[81] S. J. Byrnes, A. Lenef, F. Aieta, and F. Capasso, "Designing large, high-efficiency, high-numerical-aperture, transmissive meta-lenses for visible light," *Optics express,* vol. 24, pp. 5110-5124, 2016.

[82] Y. Kivshar and A. Miroshnichenko, "Meta-optics with Mie resonances," *Optics and Photonics News,* vol. 28, pp. 24-31, 2017.

[83] S. Kruk and Y. Kivshar, "Functional Meta-Optics and Nanophotonics Governed by Mie Resonances," *ACS Photonics,* vol. 4, pp. 2638-2649, 2017.

[84] A. Zhan, S. Colburn, R. Trivedi, T. K. Fryett, C. M. Dodson, and A. Majumdar, "Low-Contrast Dielectric Metasurface Optics," *ACS Photonics,* vol. 3, pp. 209-214, 2016.

[85] M. Khorasaninejad, W. T. Chen, R. C. Devlin, J. Oh, A. Y. Zhu, and F. Capasso, "Metalenses at visible wavelengths: Diffraction-limited focusing and subwavelength resolution imaging," *Science,* vol. 352, pp. 1190-1194, 2016.

[86] D. Fattal, J. Li, Z. Peng, M. Fiorentino, and R. G. Beausoleil, "Flat dielectric grating reflectors with focusing abilities," *Nature Photonics,* vol. 4, p. 466, 05/02/online 2010.

[87] Z. Wang, Y. Xu, and Y. Zhao, "Aberration analyses for liquid zooming lenses without moving parts," *Optics communications,* vol. 275, pp. 22-26, 2007.

[88] M. Khorasaninejad, Z. Shi, A. Y. Zhu, W.-T. Chen, V. Sanjeev, A. Zaidi*, et al.*, "Achromatic metalens over 60 nm bandwidth in the visible and metalens with reverse chromatic dispersion," *Nano letters,* vol. 17, pp. 1819-1824, 2017.

[89] M. Khorasaninejad, A. Y. Zhu, C. Roques-Carmes, W. T. Chen, J. Oh, I. Mishra*, et al.*, "Polarization-insensitive metalenses at visible wavelengths," *Nano letters,* vol. 16, pp. 7229-7234, 2016.

[90] S. Shrestha, A. C. Overvig, M. Lu, A. Stein, and N. Yu, "Broadband achromatic dielectric metalenses," *Light: Science & Applications,* vol. 7, p. 85, 2018.

[91] L. Zhang, S. Mei, K. Huang, and C. W. Qiu, "Advances in full control of electromagnetic waves with metasurfaces," *Advanced Optical Materials,* vol. 4, pp. 818-833, 2016.

[92] X. Ni, S. Ishii, A. V. Kildishev, and V. M. Shalaev, "Ultra-thin, planar, Babinet-inverted plasmonic metalenses," *Light: Science & Applications,* vol. 2, p. e72, 2013.

[93] L. Zhang, J. Ding, H. Zheng, S. An, H. Lin, B. Zheng*, et al.*, "Ultra-thin high-efficiency mid-infrared transmissive Huygens meta-optics," *Nature communications,* vol. 9, p. 1481, 2018.

[94] P. Ding, Y. Li, L. Shao, X. Tian, J. Wang, and C. Fan, "Graphene aperture-based metalens for dynamic focusing of terahertz waves," *Optics express,* vol. 26, pp. 28038-28050, 2018.

[95] C. H. Liu, J. Zheng, S. Colburn, T. K. Fryett, Y. Chen, X. Xu*, et al.*, "Ultrathin van der Waals Metalenses," *Nano Lett,* vol. 18, pp. 6961-6966, Nov 14 2018.

[96] A. Zhan, T. K. Fryett, S. Colburn, and A. Majumdar, "Inverse design of optical elements based on arrays of dielectric spheres," *Appl Opt,* vol. 57, pp. 1437-1446, Feb 20 2018.

[97] A. Yi, Y. Chen, F. Klocke, G. Pongs, A. Demmer, D. Grewell*, et al.*, "A high volume precision compression molding process of glass diffractive optics by use of a micromachined fused silica wafer mold and low Tg optical glass," *Journal of Micromechanics and Microengineering,* vol. 16, p. 2000, 2006.

[98] W. Däschner, P. Long, R. Stein, C. Wu, and S. Lee, "Cost-effective mass fabrication of multilevel diffractive optical elements by use of a single optical exposure with a gray-scale mask on high-energy beam-sensitive glass," *Applied optics,* vol. 36, pp. 4675-4680, 1997.

[99] R. C. Rumpf. (2012). *Computational Electromagnetics* [Internet]. Available: http://emlab.utep.edu/ee5390cem.htm

[100] M. Farhat, T.-C. Cheng, K. Q. Le, M. M.-C. Cheng, H. Bağcı, and P.-Y. Chen, "Mirror-backed dark alumina: A nearly perfect absorber for thermoelectronics and thermophotovotaics," *Scientific reports,* vol. 6, 2016.

[101] S. J. Corbitt, M. Francoeur, and B. Raeymaekers, "Implementation of optical dielectric metamaterials: A review," *Journal of Quantitative Spectroscopy and Radiative Transfer,* vol. 158, pp. 3-16, 2015.

[102] J. M. Garnett, "Colours in metal glasses, in metallic films, and in metallic solutions. ," *Philosophical Transactions of the Royal Society of London. Series A, Containing Papers of a Mathematical or Physical Character,* vol. 203, pp. 385-420, 1904.

[103] V. D. Bruggeman, "Berechnung verschiedener physikalischer Konstanten von heterogenen Substanzen. I. Dielektrizitätskonstanten und Leitfähigkeiten der Mischkörper aus isotropen Substanzen," *Annalen der physik,* vol. 416, pp. 636-664, 1935.

[104] M. M. Braun and L. Pilon, "Effective optical properties of non-absorbing nanoporous thin films," *Thin Solid Films,* vol. 496, pp. 505-514, 2006.

[105] W. T. Doyle, "Optical properties of a suspension of metal spheres," *Physical review B,* vol. 39, p. 9852, 1989.

[106] G. Mie, "Beiträge zur Optik trüber Medien, speziell kolloidaler Metallösungen," *Annalen der physik,* vol. 330, pp. 377-445, 1908.

[107] A. Malasi, R. Kalyanaraman, and H. Garcia, "From Mie to Fresnel through effective medium approximation with multipole contributions," *Journal of Optics,* vol. 16, p. 065001, 2014.

[108] G. H. Cross, "Fundamental limit to the use of effective medium theories in optics," *Optics letters,* vol. 38, pp. 3057-3060, 2013.

[109] R. Joerger, R. Gampp, A. Heinzel, W. Graf, M. Köhl, P. Gantenbein*, et al.*, "Optical properties of inhomogeneous media," vol. 54, pp. 351-361, 1998.

[110] C. F. Bohren, "Applicability of effective-medium theories to problems of scattering and absorption by nonhomogeneous atmospheric particles," *Journal of the atmospheric sciences,* vol. 43, pp. 468-475, 1986.

[111] F. Valdivia-Valero and M. Nieto-Vesperinas, "Composites of resonant dielectric rods: A test of their behavior as metamaterial refractive elements," *Photonics and Nanostructures-Fundamentals and Applications,* vol. 10, pp. 423-434, 2012.

[112] S. M. Musa, *Computational nanophotonics: modeling and applications*: CRC Press, 2013.

[113] B. Gallinet, J. Butet, and O. J. Martin, "Numerical methods for nanophotonics: standard problems and future challenges," *Laser & Photonics Reviews,* vol. 9, pp. 577-603, 2015.

[114] C. Min, P. Wang, X. Jiao, Y. Deng, and H. Ming, "Beam manipulating by metallic nano-optic lens containing nonlinear media," *Optics Express,* vol. 15, pp. 9541-9546, 2007.

[115] M. Suarez, T. Grosjean, D. Charraut, and D. Courjon, "Nanoring as a magnetic or electric field sensitive nano-antenna for near-field optics applications," *Optics communications,* vol. 270, pp. 447-454, 2007.

[116] K. Yee, "Numerical solution of initial boundary value problems involving Maxwell's equations in isotropic media," *IEEE Transactions on antennas and propagation,* vol. 14, pp. 302-307, 1966.

[117] P. E. Blöchl, O. Jepsen, and O. K. Andersen, "Improved tetrahedron method for Brillouin-zone integrations," *Physical Review B,* vol. 49, p. 16223, 1994.

[118] C. Ye, A. Chen, P. Colombo, and C. Martinez, "Ceramic microparticles and capsules via microfluidic processing of a preceramic polymer," *Journal of The Royal Society Interface,* vol. 7, pp. S461-S473, 2010.

[119] G. Guan, Z. Zhang, Z. Wang, B. Liu, D. Gao, and C. Xie, "Single-Hole Hollow Polymer Microspheres toward Specific High-Capacity Uptake of Target Species," *Advanced Materials,* vol. 19, pp. 2370-2374, 2007.

[120] W. Liu, J. Zhang, B. Lei, H. Ma, W. Xie, and H. Hu, "Ultra-directional forward scattering by individual core-shell nanoparticles," *Optics express,* vol. 22, pp. 16178-16187, 2014.

[121] C. F. Bohren and D. R. Huffman, *Absorption and scattering of light by small particles*: John Wiley & Sons, 2008.

[122] T. Shibanuma, P. Albella, and S. A. Maier, "Unidirectional light scattering with high efficiency at optical frequencies based on low-loss dielectric nanoantennas," *Nanoscale,* vol. 8, pp. 14184-92, Aug 7 2016.

[123] Y. H. Fu, A. I. Kuznetsov, A. E. Miroshnichenko, Y. F. Yu, and B. Luk'yanchuk, "Directional visible light scattering by silicon nanoparticles," *Nature communications,* vol. 4, p. 1527, 2013.

[124] T. Shegai, P. Johansson, C. Langhammer, and M. Käll, "Directional scattering and hydrogen sensing by bimetallic Pd–Au nanoantennas," *Nano letters,* vol. 12, pp. 2464-2469, 2012.

[125] F. A. C. Lucena, M. de Oliveira, C. P. Silva, T. Pedrosa, and M. de Melo, "Controlled directivity and gain of antenna using square loop RFSS based on PIN diode," in *Microwave and Optoelectronics Conference (IMOC), 2017 SBMO/IEEE MTT-S International*, 2017, pp. 1-4.

[126] R. Oliveira, D. Freitas, M. Romeu, M. Silva, A. Sales, A. Ferreira*, et al.*, "Design and simulation of Na2Nb4O11 dielectric resonator antenna added with Bi2O3 for microwave applications," *Microwave and Optical Technology Letters,* vol. 58, pp. 1211-1217, 2016.

[127] D. Paiva, M. Silva, A. Sombra, and P. Fechine, "Properties of the Sr 3 MoO 6 electroceramic for RF/microwave devices," *Journal of Alloys and Compounds,* 2018.

[128] I. M. Hancu, A. G. Curto, M. Castro-López, M. Kuttge, and N. F. van Hulst, "Multipolar interference for directed light emission," *Nano letters,* vol. 14, pp. 166-171, 2013.

[129] A. R. AlAjmi and M. A. Saed, "Corner reflector dielectric surface wave antenna with enhanced directivity," in *Wireless and Microwave Technology Conference (WAMICON), 2015 IEEE 16th Annual*, 2015, pp. 1-3.

[130] L. Junhua, K. Qiang, W. Chunxia, S. Baoqing, X. Yiyang, and C. Hongda, "Design of a photonic crystal microcavity for biosensing," *Journal of Semiconductors,* vol. 32, p. 034008, 2011.

[131] C. Feng, G. Feng, G. Zhou, N. Chen, and S. Zhou, "Design of an ultracompact optical gas sensor based on a photonic crystal nanobeam cavity," *Laser Physics Letters,* vol. 9, p. 875, 2012.

[132] D. J. Ripin, K.-Y. Lim, G. Petrich, P. R. Villeneuve, S. Fan, E. Thoen*, et al.*, "One-dimensional photonic bandgap microcavities for strong optical confinement in GaAs and GaAs/AlxOy semiconductor waveguides," *Journal of lightwave technology,* vol. 17, p. 2152, 1999.

[133] A. Di Falco, L. O'faolain, and T. Krauss, "Chemical sensing in slotted photonic crystal heterostructure cavities," *Applied physics letters,* vol. 94, p. 063503, 2009.

[134] P. B. Deotare, M. W. McCutcheon, I. W. Frank, M. Khan, and M. Lončar, "High quality factor photonic crystal nanobeam cavities," *Applied Physics Letters,* vol. 94, p. 121106, 2009.

[135] H.-w. Fu, H. Zhao, X.-g. Qiao, Y. Li, D.-z. Zhao, and Z. Yong, "Study on a novel photonic crystal temperature sensor," *Optoelectronics Letters,* vol. 7, pp. 419-422, 2011.

[136] N. Sultanova, S. Kasarova, and I. Nikolov, "Dispersion Proper ties of Optical Polymers," *Acta Physica Polonica-Series A General Physics,* vol. 116, p. 585, 2009.

[137] M. Makarova, Y. Gong, S.-L. Cheng, Y. Nishi, S. Yerci, R. Li*, et al.*, "Photonic crystal and plasmonic silicon-based light sources," *IEEE Journal of Selected Topics in Quantum Electronics,* vol. 16, pp. 132-140, 2010.

[138] P. V. Rysselberghe, "Remarks concerning the Clausius-Mossotti Law," *The Journal of Physical Chemistry,* vol. 36, pp. 1152-1155, 1931/01/01 1931.

[139] R. G. Barrera, G. Monsivais, and W. L. Mochán, "Renormalized polarizability in the Maxwell Garnett theory," *Physical Review B,* vol. 38, p. 5371, 1988.

[140] A. Parola, R. Piazza, and V. Degiorgio, "Optical extinction, refractive index, and multiple scattering for suspensions of interacting colloidal particles," *The Journal of chemical physics,* vol. 141, p. 124902, 2014.

[141] K. Kim, S. Yoo, J.-H. Huh, Q. H. Park, and S. Lee, "Limitations and Opportunities for Optical Metafluids To Achieve an Unnatural Refractive Index," *ACS Photonics,* vol. 4, pp. 2298-2311, 2017/09/20 2017.

[142] L. Novotny and B. Hecht, "Principle of Nano-Optics (Cambridge, New York, 2006)," *18The commercial package COMSOL Multiphysics was employed,* p. 38.

[143] A. Malasi, H. Taz, M. Ehrsam, J. Goodwin, H. Garcia, and R. Kalyanaraman, "Enhanced and tunable optical quantum efficiencies from plasmon bandwidth engineering in bimetallic CoAg nanoparticles," *APL Photonics,* vol. 1, p. 076101, 2016.

[144] A. Alvaro Ranha Neves and D. Pisignano, "Effect of finite terms on the truncation error of Mie series," *Optics Letters,* vol. 37, pp. 2418-2420, 2012/06/15 2012.

[145] A. Pinchuk and G. Schatz, "Anisotropic polarizability tensor of a dimer of nanospheres in the vicinity of a plane substrate," *Nanotechnology,* vol. 16, p. 2209, 2005.

[146] J. Vieaud, O. Merchiers, M. Rajaoarivelo, M. Warenghem, Y. Borensztein, V. Ponsinet*, et al.*, "Effective medium description of plasmonic couplings in disordered polymer and gold nanoparticle composites," *Thin Solid Films,* vol. 603, pp. 452-464, 2016.

[147] N. Yu and F. Capasso, "Flat optics with designer metasurfaces," *Nature materials,* vol. 13, p. 139, 2014.

[148] L. Wang, S. Kruk, H. Tang, T. Li, I. Kravchenko, D. N. Neshev*, et al.*, "Grayscale transparent metasurface holograms," *Optica,* vol. 3, p. 1504, 2016.

[149] M. I. Shalaev, J. Sun, A. Tsukernik, A. Pandey, K. Nikolskiy, and N. M. Litchinitser, "High-efficiency all-dielectric metasurfaces for ultracompact beam manipulation in transmission mode," *Nano letters,* vol. 15, pp. 6261-6266, 2015.

[150] S. Campione, L. I. Basilio, L. K. Warne, and M. B. Sinclair, "Tailoring dielectric resonator geometries for directional scattering and Huygens' metasurfaces," *Optics Express,* vol. 23, pp. 2293-2307, 2015.

[151] J. F. Algorri, B. García-Cámara, A. Cuadrado, J. M. Sánchez-Pena, and R. Vergaz, "Selective Dielectric Metasurfaces Based on Directional Conditions of Silicon Nanopillars," *Nanomaterials,* vol. 7, p. 177, 2017.

[152] P. Lalanne, S. Astilean, P. Chavel, E. Cambril, and H. Launois, "Design and fabrication of blazed binary diffractive elements with sampling periods smaller than the structural cutoff," *JOSA A,* vol. 16, pp. 1143-1156, 1999.

[153] P. Lalanne, S. Astilean, P. Chavel, E. Cambril, and H. Launois, "Blazed binary subwavelength gratings with efficiencies larger than those of conventional échelette gratings," *Optics letters,* vol. 23, pp. 1081-1083, 1998.

[154] A. A. Siraji and Y. Zhao, "Tunable optical transmission of magnetic microsphere colloids," *Applied Optics,* vol. 57, pp. 10412-10417, 2018.

[155] A. A. Siraji and Y. Zhao, "Simple effective medium approximation with Rayleigh scattering," *Optics letters,* vol. 42, pp. 1860-1863, 2017.

[156] E. Wang and Y. Zhao, "Etching of nanostructures on soda-lime glass," *Optics letters,* vol. 39, pp. 3748-3751, 2014.

[157] D. G. Voelz, *Computational fourier optics: a MATLAB tutorial*: SPIE press Bellingham, WA, 2011.

[158] F. Chen and H. Craighead, "Diffractive phase elements based on two-dimensional artificial dielectrics," *Optics letters,* vol. 20, pp. 121-123, 1995.

[159] M. Ye, V. Ray, and Y. S. Yi, "Achromatic Flat Subwavelength Grating Lens Over Whole Visible Bandwidths," *IEEE Photonics Technology Letters,* vol. 30, pp. 955-958, 2018.

[160] A. Arbabi, Y. Horie, A. J. Ball, M. Bagheri, and A. Faraon, "Subwavelength-thick lenses with high numerical apertures and large efficiency based on high-contrast transmitarrays," *Nature communications,* vol. 6, p. 7069, 2015.

[161] A. She, S. Zhang, S. Shian, D. R. Clarke, and F. Capasso, "Large area metalenses: design, characterization, and mass manufacturing," *Optics express,* vol. 26, pp. 1573-1585, 2018.

[162] P. Lalanne and P. Chavel, "Metalenses at visible wavelengths: past, present, perspectives," *Laser & Photonics Reviews,* vol. 11, p. 1600295, 2017.

[163] J. Ge, L. He, Y. Hu, and Y. Yin, "Magnetically induced colloidal assembly into field-responsive photonic structures," *Nanoscale,* vol. 3, pp. 177-83, Jan 2011.

VII. ABSTRACT

OPTICAL NANOSTRUCTURES FOR CONTROLLABLE AND TUNABLE OPTICAL PROPERTIES

by

ASHFAQUL ANWAR SIRAJI

December 2019

Advisor: Dr. Yang Zhao

Major: Electrical Engineering

Degree: Doctor of Philosophy

Optical nanostructures are heterogeneous media containing subwavelength inclusions. Their optical properties can be controlled and tuned using the constituent material properties and spatial arrangement of the inclusions. While optical nanostructures have been widely studied, controllable and tunable nanostructures using low loss transparent materials have not been studied in detail in the literature. The objective of this research is to perform efficient design and analyses of controllable and tunable optical nanostructure using low loss transparent materials.

To that end, versatile and highly accurate full-wave numerical methods like finite different time domain and plane wave expansion methods are reviewed first. These methods are compared in terms of their speed, accuracy, and memory requirement. Different kinds of optical nanostructures, consisting of low index transparent materials, are analyzed to study their controllability. For example, single scatterers are optimized to obtain highly directional forward scattering using low index materials. Then, the minimum refractive index required for establishing optical bandgap in a planar photonic crystal was

established. Using optical bandgap on low index materials, highly sensitive transparent sensors are designed. It is found that full-wave numerical methods can analyze small or periodic nanostructure, while requiring significant computational resources for accurate result. Full-wave numerical analyses of aperiodic structures can be highly resource consuming, without producing insightful outcome.

As an alternative to full-wave numerical modelling, analytical effective medium approximations are considered. The available approximations are reviewed, and their limitations are pointed out. Using the Mie scattering theory, the Maxwell-Garnett approximation is extended so that it can account for arbitrary size, as well as different physical structure, of the inclusions. The derived effective medium approximation is tested on a wide variety of optical nanostructure, both periodic and aperiodic. Good agreement between analytical and experimental results is established. The utility of the approximation in designing a controllable and tunable optical nanostructure is demonstrated by modelling the tunable optical properties of magnetic colloids and verifying them experimentally. When appropriate, the effective medium approximation can be a very fast, and efficient method of analyzing the controllable and tunable properties of optical nanostructure. The applicability, limits of validity, and limitation of the approximation is discussed.

Using the analytical framework, controllable flat optical nanostructure that can mimic optical elements, e.g., focusing lenses, are designed. In these optical nanostructures, inclusions are arranged in a flat thin film so that a specific profile of optical density is implemented. By modifying the wave-front of the emergent wave in a controllable manner, these flat nanostructures can perform the same optical operations

as bulky and spherical optical components. Such flat optical components are particularly promising for developing integrated optical chips. However, full-wave numerical modelling of these structures can be difficult since the optical component may be large area, while the nanostructure can be deeply sub-wavelength. Hence, for efficient design of such flat lenses, the relationship between the physical structure of the inclusions and the imparted phase by the nanostructure is studied using effective medium approximation. It was found that the effective medium approximation can predict the imparted phase with high accuracy, while requiring a fraction of the computation resources compared to numerical methods. Based on the relationship between the imparted phase and the physical structure of the inclusions, it is possible to design flat lenses with a controllable spatial phase profile analytically. Furthermore, their far-field properties can also be calculated from the near field ones using the analytical scalar diffraction theory. Thus, controllable flat optical lenses can be designed and analyzed analytically. The analytical results matched very well with the numerical and experimental results, while requiring very little memory and time.

In conclusion, an analytical method for designing and analyzing a tunable and controllable optical nanostructure is derived and verified with experimental results. The analytical method is significantly more efficient compared to numerical methods, while being similarly accurate compared to experimental results. The research in this work can lead to efficient design of optical nanostructure for many different fields, including flat optics, optical switching, and transparent sensing.

VIII. AUTOBIOGRAPHICAL STATEMENT

Educational Credentials:

Ph.D. (December 2019), Department of Electrical and Computer Engineering department, Wayne State University
Advisor: Yang Zhao
Dissertation title: Optical Nanostructures for Controllable and Tunable Optical Properties.

M.S. (December 2014), Department of Electrical and Electronic Engineering, Bangladesh University of Engineering and technology.
Advisor: M Shah Alam
Thesis title: Design and analysis of heterostructure based tunable nanophotonic resonators with high Q and low mode volume.

B.S. (April 2012), Department of Electrical and Electronic Engineering, Bangladesh University of Engineering and technology.
Supervisor: M Shah Alam

Honors and Awards:

- Winner, Second place: Wayne State Graduate Exhibit, 2015.
- The Thomas C. Rumble University Graduate Fellowship, 2018-19.
- Editor's Pick: Applied Optics, June 2019.

Organizations:

- Tau Beta Pie, Michigan Epsilon Chapter
- IEEE Photonics Society.

Selected Publications:

- A. Siraji and Y. Zhao, "Design and analysis of thin optical lens composed of low index subwavelength structures", Applied Optics, vol. 58, issue 18, (2019). *Editor's Pick*.
- A. Siraji and Y. Zhao, " Tunable optical transmission of magnetic microsphere colloids," Applied Optics, vol. 57, issue 36, pp. 10412-10417, (2018).
- A. Siraji and Y. Zhao, "Simple effective medium approximation with Rayleigh scattering," Optics Letters, vol. 42, pp. 1860-1863, 2017
- A. Siraji and Y. Zhao, "High-sensitivity and high-Q-factor glass photonic crystal cavity and its applications as sensors," Optics letters, vol. 40, pp. 1508-1511, 2015.
- A. Siraji and Y. Zhao, "Enhanced directional scattering by low-index microspheres", *in* IEEE MTT-S International Microwave Workshop Series on Advanced Materials and Processes 2018 (IMWS-AMP 2018).
- A. Siraji and Y. Zhao, "High Q-factor photonic crystal cavities on transparent polymers," in Photonics Conference (IPC), 2015, 2015, pp. 373-374.